File ID	72854
Filename	Thesis

SOURCE (OR PART OF THE FOLLOWING SOURCE):

Type	Dissertation
Title	Charm in the proton : an analysis of charm production in deep inelastic scattering.
Author	S.E.S. Schagen
Faculty	Faculty of Science
Year	2004
Pages	152

FULL BIBLIOGRAPHIC DETAILS:
http://dare.uva.nl/record/170669

charm in the proton

an analysis of charm production in deep inelastic scattering

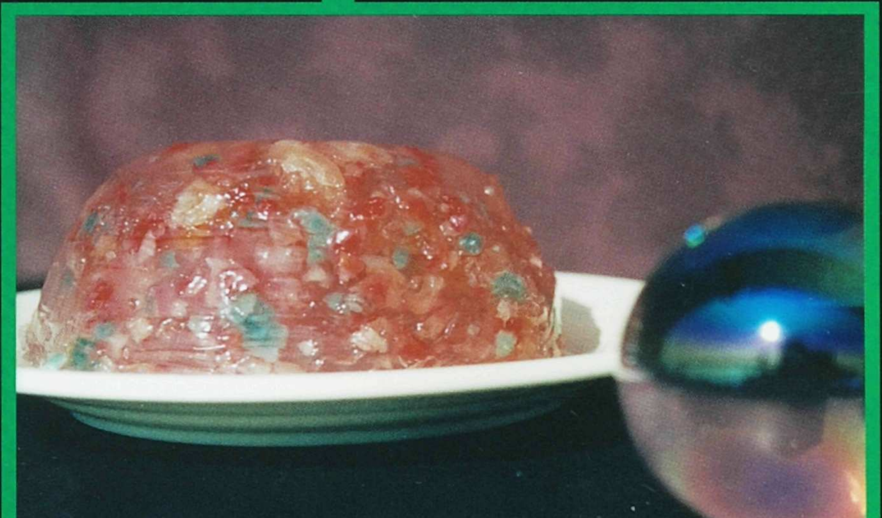

s.e.s. schagen

Charm in the proton

An analysis of charm production in deep inelastic scattering

Charm in the proton

An analysis of charm production in deep inelastic scattering

ACADEMISCH PROEFSCHRIFT

TER VERKRIJGING VAN DE GRAAD VAN DOCTOR
AAN DE UNIVERSITEIT VAN AMSTERDAM
OP GEZAG VAN DE RECTOR MAGNIFICUS
PROF.MR. P.F. VAN DER HEIJDEN
TEN OVERSTAAN VAN EEN DOOR HET COLLEGE VOOR PROMOTIES
INGESTELDE COMMISSIE, IN HET OPENBAAR TE VERDEDIGEN
IN DE AULA DER UNIVERSITEIT
OP 23 JANUARI 2004, TE 10.00 UUR

door

Sven Edmond Simon Schagen

geboren te Amsterdam

Promotor: prof.dr. P.M. Kooijman
Co Promotor: dr. E.N. Koffeman

Faculteit der Natuurwetenschappen, Wiskunde en Informatica

ISBN 90-6464-769-0

The work described in this thesis is part of the research programme of 'het Nationaal Instituut voor Kernfysica en Hoge-Energie Fysica' (NIKHEF) in Amsterdam, the Netherlands. The author was financially supported by the 'Stichting Fundamenteel Onderzoek der Materie' (FOM).

For Claudia

Is it not a strange fate
that we should suffer so much fear and doubt
for so small a thing ?

- Boromir, Son of Denethor
26 February 3019 of The Third Age

Preface

For a long time people assumed the proton to be a fundamental particle of nature. Together with the neutron and the electron the proton builds up every single piece of matter that we see in the world today.

Through the hard work of many people, experimentalists and theoreticians alike, our picture of the proton has changed. Today we view the proton as a sort of trifle, pudding richly flavoured with small pieces of fruit. Most of the proton is gooey, the effect of the strong force mediators the gluons. But often one can also find a hard bit in the jelly: the quarks, of which there are six different flavours.

The physics of scattering of electrons off the proton can also be visualised using the pudding-analogy as follows. Envisage the electron as a glass marble. When the marble is shot at the trifle several scenarios can develop, depending on the energy (=speed) of the marble. If the marble goes too slow, it will collide with the pudding and be recoiled. If the experiment is repeated a number of times, all that will be seen is the outline of the pudding which will appear rather solid. When the marble moves at higher speed, it will actually penetrate the proton and given that the marble has enough energy, it will break up the pudding! Subsequent analysis of the slabs of jelly and fruit scattered throughout the room give insight in the structure of the jelly pudding, as it was before it was blown into a wealth of small pieces.

This is more or less how the proton structure was discovered. At first electrons had too low an energy to actually probe the inner region of the proton and therefore gave rise to the idea that the proton was one of nature's fundamental building blocks. In 1969 experiments at the Stanford Linear Accelerator Center (SLAC) could use electrons with enough energy to break up the proton [1]. Such interactions, where the proton is destroyed are called *deep inelastic scattering.* Through the analysis of the structure hidden in the properties of the fragments after the break up of a proton we have learned about the internal structure of the proton and the rules that govern the internal dynamics of the protons constituents. We can thus reconstruct a picture of the how the proton was before the electron tore it apart.

In this thesis an analysis of the production of the charm quark in deep inelastic *ep* scattering interactions is presented. The charm quark is actually heavier than the proton itself, by approximately 30%. The fact that charm quarks can be (pair!) produced is a purely quantum mechanical effect, which follows from the Heisenberg Uncertainty Principle. This principle states that some energy can be 'borrowed', provided it is for a sufficiently short time. The underlying production mechanism is described by the theory Quantum Chromo Dynamics (QCD). Measurements of heavy quark production in deep inelastic scattering therefore are a test of QCD.

The goal of this thesis is to contribute to the verification or falsification of the assumption that this QCD production mechanism indeed describes the production of charm in deep inelastic scattering. To obtain this goal a measurement of charm production is made by identifying the electrons of the weak decay $\bar{c} \rightarrow e^- \nu_e s$ which has a branching ratio of 9.6 ± 0.4%. This measurement is presented in the chapters 4-6. The analysis is based on data collected with the ZEUS detector in 1996-1997, which will be presented in chapter 3. In total 32 pb^{-1} is analysed. A review of the theoretical framework is given in chapter 1. In chapter 2 the software implementations of the calculations are introduced. Such programmes are used in the modelling of deep inelastic interactions, and heavy quark production in particular, is described. They form a fundamental cornerstone of the analysis presented in the chapters thereafter. The final chapter describes fits of the theoretical predictions to the available data on charm production in deep inelastic scattering. This comprises the semileptonic charm decay data, presented in this thesis, and the published $D^{*\pm}$ results from both the ZEUS and H1 experiment. These fits will have a twofold use. First, they will lead to a novel way to extract the mass of the charm quark. The second will be that these fits can be used to quantitatively answer the question whether QCD can describe todays data on charm production.

CONTENTS

CHAPTER 1

Taking apart the proton

1.1. Introduction

The production of heavy quarks in deep inelastic electron proton scattering poses a rich testing ground for the QCD sector of the Standard Model. The mass of these quarks is higher than the fundamental cut-off scale of QCD, Λ_{QCD}. The production of heavy quarks can as a result be treated completely perturbatively.

In the experimental environment of electron proton scattering, where the probe is electroweak in nature, the measurement of heavy quarks can be directly related to a hard QCD production process. Hence the measurement of heavy quark production is a direct test of QCD.

The QCD production process for *ep*-scattering, boson-gluon fusion, is driven by the proton's gluon content. The gluon density functions of the proton are not obtained through direct experimental measurement, but indirectly, from the scaling violations of the structure function of the proton. The measurement of heavy quark production can therefore also verify the universality of the gluon density function.

Of the heavy quarks, the charm quark is the lightest. At about 1.3 GeV it is roughly four times lighter than the next heavy quark, beauty and therefore copiously more produced. The fact that the electric charge of the charm quark is twice that of the beauty quark further enhances the charm/beauty production ratio.

Measurements of charm production must be inevitably done through the detection of charmed mesons. One particularly popular method for doing this is the identification of the $D^{*\pm}(2010)$-meson, which is formed by 23.5 ± 1.0% of the produced (anti)charm quarks. This meson can follow the decay chain $D^{*+} \rightarrow \pi_s^+ D^0 \rightarrow \pi_s^+ K^- \pi^+$ (or charge conjugate), where the subscript s denotes the so-called slow-pion. Due to the small mass difference between the $D^{*\pm}$ and the D^0 mesons, only 140 MeV, this slow-pion is practically at rest in the D-meson rest frame. The reconstruction of this mass difference results in a very clean signal for charm production. The analysis of this decay chain is the predominant source of the world data for

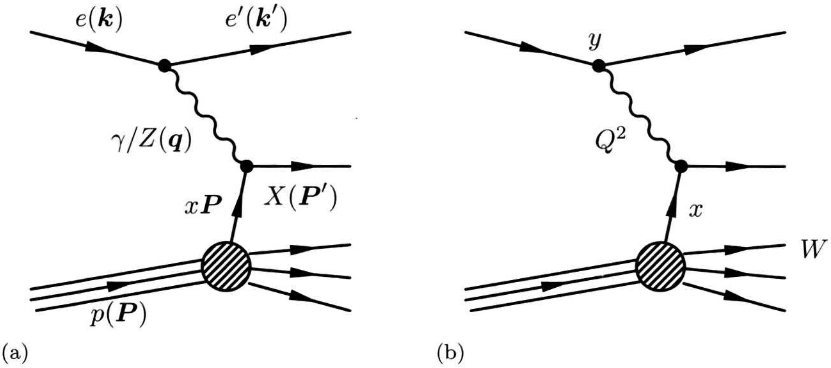

Figure 1.1: *Feynman-diagrams of deep inelastic scattering with the kinematics of the interaction in terms of (a) four-vectors and (b) the invariants.*

deep inelastic *ep* scattering charm production. Unfortunately, there is also a downside to using this method. The combined branching ratio of this decay chain is $67.7\% \times 3.80\% = 2.57\%$: only a small fraction of the all produced charm quarks is *a priori* visible in this channel.

An alternative is the identification of the semileptonic decay of charmed mesons, with a branching fraction $\mathrm{BR}(\bar{c} \to e^-) = 9.6 \pm 0.4\%$. The main body of this thesis (Ch.2-6) will be dedicated to the measurement of these electrons. In this chapter the theoretical framework relevant to the production of charm quarks in deep inelastic *ep*-scattering will first be presented.

1.2. Neutral current deep inelastic scattering

1.2.1. Kinematics of the interaction

In neutral current deep inelastic scattering (NC-DIS) an electron and proton interact, through the exchange of a photon (Z-boson), breaking up the proton in the process:

$$e(\boldsymbol{k}) + p(\boldsymbol{P}) \to e'(\boldsymbol{k}') + X(\boldsymbol{P}' = \boldsymbol{P} + \boldsymbol{q}) \tag{1.1}$$

Here, $X(\boldsymbol{P}')$ denotes any final state that fits energy-momentum conservation. Throughout this text, bold symbols will denote the Lorentz four vectors of the particles. The interaction in fact takes place between the electron and a quark in the proton:

$$e(\boldsymbol{k}) + q(x\boldsymbol{P}) \to e'(\boldsymbol{k}') + q'(\boldsymbol{\zeta}) \tag{1.2}$$

The quark carries only a fraction of the total proton four momentum. This is denoted by the x, the Bjorken scaling variable. The four momentum of the exchanged photon is given by $\boldsymbol{q} = \boldsymbol{k} - \boldsymbol{k}'$, see Fig. 1.1(a). A hard scattering process of the type described above is defined by the following four Lorentz scalars

$$Q^2 \equiv -\boldsymbol{q}^2 = (\boldsymbol{k} - \boldsymbol{k}')^2 \tag{1.3}$$

$$x \equiv \frac{-\boldsymbol{q}^2}{2\boldsymbol{P} \cdot \boldsymbol{q}} \tag{1.4}$$

$$y \equiv \frac{\boldsymbol{P} \cdot \boldsymbol{q}}{\boldsymbol{P} \cdot \boldsymbol{k}} \tag{1.5}$$

$$W^2 \equiv (\boldsymbol{P} + \boldsymbol{q})^2 \tag{1.6}$$

which all have an intuitive interpretation at the leading order of the QCD perturbation expansion. The virtuality or mass of the photon is given by Q^2, which also is the measure of the probing depth of an interaction. A higher value of Q^2 means that the photon will resolve structures at a smaller scale. The interpretation of x was already given. The variable y, the inelasticity, is, in the proton centre of mass frame, the fraction of the energy of the electron transfered to the proton. Finally, the mass of the hadronic system after the interaction, including the proton remnant, is given by W. The four kinematic variables are related through

$$Q^2 = sxy \tag{1.7}$$

where $s = (\boldsymbol{k} + \boldsymbol{P})^2$ is the centre of mass energy squared, and

$$W^2 = sy(1 - x) + m_P^2 \tag{1.8}$$

which includes the mass of the proton, m_P.

1.2.2. Structure functions

Under the assumption that deep inelastic scattering can be described by the exchange of a single virtual gauge boson, the most general form for the unpolarised cross section for positron proton scattering is given in terms of the structure functions F_i:

$$\frac{d^2\sigma}{dQ^2dx} = \frac{2\pi\alpha^2}{xQ^4}\left[Y_+F_2(x,Q^2) - y^2F_L(x,Q^2) - Y_-xF_3(x,Q^2)\right] \tag{1.9}$$

where $Y_\pm = 1 \pm (1-y)^2$. In this equation F_L describes the coupling of the proton to the longitudinal photons, and xF_3 is a parity violating term arising from the Z^0 exchange. F_2 gives the sum of both transverse and longitudinal couplings. When the typical scale of the interactions, Q^2, is much lower than the scale of the weak interactions, *viz.* $Q^2 \ll M_Z^2$, the contribution of xF_3 will be negligible compared to the other contributions.

In comparing the cross section for the interaction of a positron with a free spin-$\frac{1}{2}$ quark with the general expression 1.9 one finds that F_2 can be interpreted as

$$F_2(x) = x \sum_{i=u,d,s} e_i^2(q_i(x) + \bar{q}_i(x)) \tag{1.10}$$

where q_i are the quark densities inside the proton of quark flavour i and e_i is the charge of that quark. In this case helicity conservation also requires that for massless quarks $F_L = 0$.

The quark densities are more often referred to as the *parton density functions of the proton* or PDFs. The parton density functions are not calculable from first principles. They must therefore be obtained from data. The interpretation of structure functions in terms of quark densities is only unique at the leading order of QCD. It is nevertheless a useful and intuitive picture of the meaning of the structure function. The total momentum carried by quarks in the proton can be determined from the parton density functions. It turns out that only about half of the total proton momentum is carried by these charged constituents. The other half of the momentum therefore needs to be taken by the gluons. In the QCD picture of the proton quarks are continuously exchanging gluons. The addition of these higher order QCD interactions also give rise to a non-zero coupling to the longitudinal photon by off mass-shell quarks, so that $F_L \neq 0$.

1.3. QCD dynamics and evolution

1.3.1. Resolving smaller scales

Figure 1.2(a) shows a (low) Q^2 photon probing a quark in the proton. Its 'long' wavelength limits the level of detail to which it is sensitive: it is 'blind' to the gluon emission-absorption that takes place within a distance less that the wavelength, indicated by the circle. A photon with a (greatly) increased value of Q^2 (Fig. 1.2(b)) has a smaller wavelength and can resolve the quark at smaller distance scales (compare the outer and inner 'fields of view'). It can therefore interact with the quark after it emitted a gluon, but *before* this gluon was re-absorbed. The same quark is now probed while it has a lower value of x. For the parton density functions this leads in a shift of the distribution towards lower x for increasing Q^2. Hence, QCD induces the necessity of an additional scale, Q^2 for the description of the parton densities.

A similar effect is also true for gluons. Gluons may fluctuate in $q_i\overline{q}_i$-pairs, by virtue of the Heisenberg Uncertainty Principle: $\Delta E \Delta t \gtrsim \hbar$. Figure 1.2(c) shows what happens when the quantum fluctuation takes place on a spatial distance less than the wavelength of the photon: nothing. The photon cannot resolve the charge of the dipole created by the fluctuation and sees a net charge of zero. With a smaller wavelength (Fig. 1.2(d)) the photon can see the $q_i\overline{q}_i$ pair, and the individual quarks, and couple to it. The quark densities will thus increase with increasing Q^2. Analysis of the cross sections shows that this increase mainly occurs at low x. It is also clear that the change in the quark density distributions is dependent on both the quark and the gluon density; the same is true for the gluon density. The quark-antiquark densities that arise from the gluons are also referred to as the *sea quark densities*, as opposed to the valence quark density, which give the net contribution of the two u and one d constituent quarks in the proton. The sea quark density is symmetric in the flavours (u,d,s) and between particles and antiparticles.

Another consequence of this is the following. The available energy (mass) is inversely proportional to the time scale of the fluctuation. This means that massive quarks (c,b,t) can only occur during short enough times, inverse proportional to their respective masses. They will only become visible when the Q^2 crosses a sort of fuzzy lower boundary. The next section will come to talk about the production of heavy

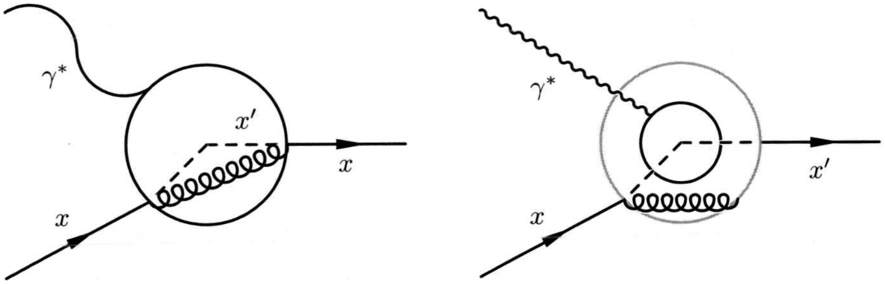

(a) $Q^2 = Q_0^2$, $x > x'$; The photon probes the quark state that is the integral of the circle and misses the effect of the gluon emission/absorption.

(b) $Q^2 \gg Q_0^2$, $x > x'$; In this case, the photon has a higher energy, or higher Q^2. As a result it sees the quark *after* the emission of the gluon, but *before* the absorption: the photon probes a quark with a smaller x.

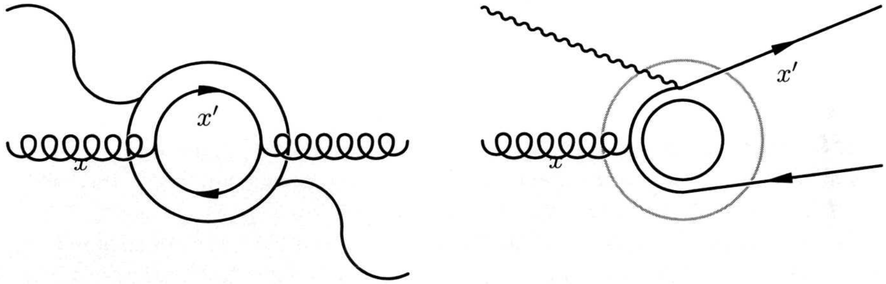

(c) $Q^2 = Q_0^2$, $x > x'$; For low values of Q^2 the photon does not resolve the gluon splitting into a quark-antiquark pair. As a result, it sees the charge integrated over the circle volume (which is zero) and ignores the gluon altogether.

(d) $Q^2 \gg Q_0^2$, $x > x'$; For high Q^2 the photon can resolve the gluon fluctuating and the photon can couple to the (anti)quark. Quarks created in this fashion typically have a low x, roughly half of that of the parent gluon.

Figure 1.2: *The effect of increase in Q^2 for the probing of quarks ((a),(b)) and of gluons ((c),(d)).*

quarks by this process. The massless (light) quarks on the other hand are not subject to such effects and therefore contribute all equally to the sea-quark density in the proton.

1.3.2. DGLAP Evolution of the parton densities

The parton densities of the proton will evolve as a function of the probe scale, due to the increase of detail that will become visible as Q^2 rises. This evolution of the parton densities as a function of Q^2 is given by the following integro-differential equation:

$$\frac{\partial}{\partial \ln Q^2} \begin{pmatrix} q_i(x, Q^2) \\ g(x, Q^2) \end{pmatrix} = \frac{\alpha_s(Q^2)}{2\pi} \int_x^1 \frac{dy}{y} \boldsymbol{P}_1 \left(\frac{x}{y}\right) \begin{pmatrix} q_i(y, Q^2) \\ g(y, Q^2) \end{pmatrix}, \tag{1.11}$$

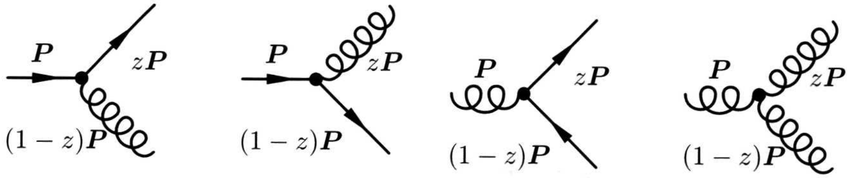

(a) P_{qq} (b) P_{gq} (c) P_{qg} (d) P_{gg}

Figure 1.3: *The diagrammatical representation of the leading order contribution to the splitting functions.*

where the q_i denotes all the active (light) quark flavours. This equation is known as the DGLAP equation, after the authors Dokshitzer [2], Gribov and Lipatov [3] and Altarelli and Parisi [4] of which the latter two derived the equation independently from their Russian colleagues. It describes the coupled evolution of both the quark and gluon densities in the proton. The DGLAP kernel is given by

$$\boldsymbol{P}_i(z') = \begin{pmatrix} P_{qq}(z') & P_{qg}(z') \\ P_{gq}(z') & P_{gg}(z') \end{pmatrix}, \tag{1.12}$$

where the functions P_{qq}, etc are known as the splitting or coefficient functions. The leading order splitting functions are given by[1]

$$P_{qq}(z) = \frac{4}{3}\left(\frac{1+z^2}{1-z}\right)_+ \tag{1.13}$$

$$P_{gq}(z) = \frac{1}{2}\left(z^2 + (1-z)^2\right) \tag{1.14}$$

$$P_{qg}(z) = \frac{4}{3}\left(\frac{1+(1-z)^2}{z}\right) \tag{1.15}$$

$$\begin{aligned} P_{gg}(z) = & 6\left(\frac{z}{1-z}_+ + \frac{1-z}{z} + z(1-z)\right) \\ & + \left(11 - \frac{n_f}{3}\right)\delta(1-z). \end{aligned} \tag{1.16}$$

These correspond to the splitting diagrams given in Fig. 1.3.

The leading order equations can be extended to next-to-leading order according

$$\frac{\partial}{\partial \ln Q^2}\begin{pmatrix} q_i \\ g \end{pmatrix} = \frac{\alpha_s}{2\pi}\int_x^1 \frac{dy}{y}\boldsymbol{P}_1\begin{pmatrix} q_i \\ g \end{pmatrix} + \frac{\alpha_s^2}{4\pi^2}\int_x^1 \frac{dy}{y}\boldsymbol{P}_2\begin{pmatrix} q_i \\ g \end{pmatrix} + \ldots \tag{1.17}$$

where the functional arguments have been omitted for the sake of brevity. The dots denote that this can be extended to any arbitrary order. The splitting functions for

---

[1] The 'plus-prescription' is used to handle the divergences in the splitting functions at $z = 1$. It is defined as

$$\int_x^1 dx\phi(x)[\psi(x)]_+ = \int_x^1 dx[\phi(x) - \phi(1)]\psi(x) - \phi(1)\int_0^x dx\psi(x)$$

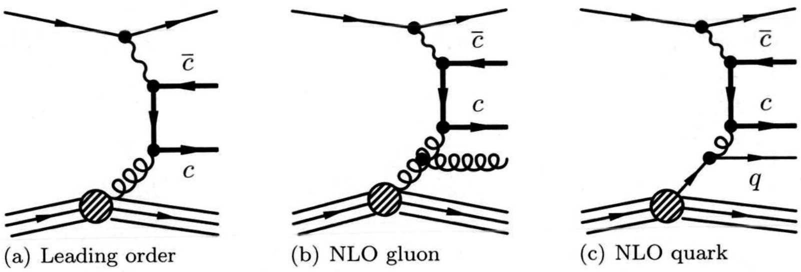

(a) Leading order (b) NLO gluon (c) NLO quark

Figure 1.4: *The leading and next-to-leading contributions to heavy quark production in neutral current deep inelastic scattering. The contribution of the NLO gluon diagram is of the order of 20%. The NLO quark contributes ≈5%.*

higher orders involve more diagrams and therefore these will gain in complexity. At higher orders, the splitting functions are more commonly referred to as the coefficient functions. The NLO splitting functions are known for some time now [4]; work is under way to calculate the NNLO (next-to-next-to-leading order) splitting functions numerically.

The DGLAP equation predicts that when the scale increases, so will the parton density at low x. This will happen at the expense of the initial high x contributions, which migrate to the low x region through the splitting processes. These migrations lead to the violation of the scaling of the parton densities, with terms logarithmic in Q^2. These scaling violations have indeed been observed experimentally, for instance [5]. These scaling violations are mainly driven by the gluon splitting diagrams. Hence, the scaling violations give a handle on the gluon density in the proton.

1.4. Heavy quark production

The double differential cross section for charm production follows directly from Eq. 1.9, which can be restricted to the charm-only case:

$$\frac{d^2\sigma^{c\bar{c}}}{dQ^2dx} = \frac{2\pi\alpha^2}{xQ^2}\Big[(1+(1-y)^2)F_2^{c\bar{c}}(x) - y^2 F_L^{c\bar{c}}(x)\Big]. \tag{1.18}$$

where the inclusive structure functions have been replaced by the charm specific functions. The difficulty of predicting charm production cross sections lies in the calculation or prediction of the charm structure functions. The pQCD inspired picture of the proton tells that charm can be produced by so-called boson-gluon fusion diagrams where a gluon splits in a (off mass-shell) $c\bar{c}$ pair which subsequently interact with a photon.

Figure 1.4 shows the leading and next-to-leading order diagrams for heavy quark production through boson-gluon fusion. The structure functions that follow from these diagrams have been calculated to next-to-leading order [6]. The result of that calculation can be written as

$$
\begin{aligned}
F_k(x,Q^2,m) = {} & \frac{Q^2\alpha_s}{4\pi^2 m^2}\int_x^{z_{max}} \frac{dz}{z} e_Q^2 f_g c^{(0)}_{k,g} \\
& + \frac{Q^2\alpha_s^2}{\pi m^2}\int_x^{z_{max}} \frac{dz}{z}\Big[e_Q^2 f_g (c^{(1)}_{k,g} + \bar{c}^{(1)}_{k,g}\ln\frac{\mu^2}{m^2}) \\
& + \sum_{i=q,\bar{q}} (e_Q^2 f_i (c^{(1)}_{k,i} + \bar{c}^{(1)}_{k,i}\ln\frac{\mu^2}{m^2}) + e_i^2 f_i d^{(1)}_{k,i})\Big], \qquad (1.19)
\end{aligned}
$$

where

$$f_{i,g} = f_{i,g}(\frac{x}{z},\mu^2),$$

and where $k = 2, L$ and $m = m_Q$ with Q the flavour of the heavy quark. The f_i denote the parton densities $(g(x,\mu^2)$,$q_i(x,\mu^2))$ in the proton and μ stands for the mass factorisation scale, which has been put equal to the renormalisation scale. The functions c and d are the coefficient functions represented in the $\overline{\text{MS}}$ scheme. Finally, the integration variable z is given by $z = Q^2/(Q^2+s)$.

Equation 1.19 is related to the diagrams of Fig. 1.4 in that the first line of the equation is equal to the leading order diagram, the second line to the gluon radiation diagram of Fig. 1.4(b) and the last term with the summation over the light quark flavours stems from the diagram in Fig. 1.4(c).

From this expression for the structure function it becomes clear that there is a strong dependence of the cross section on the quark mass

$$\sigma \propto \frac{1}{m_Q^2}. \qquad (1.20)$$

The leading-order contribution to the structure function is directly proportional to the gluon density in the proton. The next-to-leading-order contribution also contains a term that follows the gluon density. As a consequence the production of charm can be used to measure the gluon density of the proton directly, provided that boson-gluon fusion is the only source of heavy quarks in *ep*-scattering.

As Q^2 increases, the cross section becomes dominated by large logarithms that must be resummed to all orders [7]. Asymptotically charm production will behave as if the quark is massless and the evolution will be governed by four flavours. Buza, Matiounine, Smith and van Neerven [8] have shown that at the moderate Q^2 values relevant for this experiment the difference between the charm cross section calculated via the three flavour evolution combined with NLO BGF matrix elements and the full four flavour evolution is small (10% at $Q^2 = 170$ GeV^2 and $x = 0.001$). Several authors have presented methods which incorporate more or less *ad hoc* interpolations between the two schemes. The method proposed by Thorn and Roberts [9] matches the coefficient functions and their derivatives at a certain value of Q^2. The oldest and most commonly used of such interpolation schemes is given by the Zero-Mass Variable Flavour Number Scheme (ZM-VFNS). Within this scheme, the charm quark is completely decoupled from the theory, by assuming an infinite mass, below some mass scale $\mu_T \sim m_c$. Above this scale μ_T charm is treated as a massless parton in the proton, generating a non-zero quark density. However the effects are of the order of the uncertainties on the measured cross section and so will be ignored in the analyses presented in this thesis although some of the parton densities have been extracted in these so called variable flavour number schemes.

1.5. Parton density functions

There is no *a priori* knowledge on the mathematical form of the parton density functions. It is necessary to postulate some functional description, typically inspired by physical insight, and extract (fit) the parameters of those functions from data. The use of functional forms based on arguments derived from dimensional counting and Regge theory is commonplace. Though authors may vary the exact definition, the most common parametrisation has the form

$$\begin{aligned} xg(x,Q_0^2) &\equiv A_g x^{\delta_g}(1-x)^{\eta_g}(1+\gamma_g x); \\ xu_v(x,Q_0^2) &\equiv A_u x^{\delta_u}(1-x)^{\eta_u}(1+\epsilon_u\sqrt{x}+\gamma_u x); \\ xd_v(x,Q_0^2) &\equiv A_d x^{\delta_d}(1-x)^{\eta_d}(1+\epsilon_d\sqrt{x}+\gamma_d x); \\ xS(x,Q_0^2) &\equiv A_s x^{\delta_s}(1-x)^{\eta_s}(1+\epsilon_s\sqrt{x}+\gamma_s x); \\ x\Delta(x,Q_0^2) &\equiv A_\Delta x^{\delta_\Delta}(1-x)^{\eta_\Delta}, \end{aligned} \tag{1.21}$$

where $u_v(d_v)$ is the $u(d)$ valence quark density, $S \equiv 2(\overline{u}+\overline{d}+\overline{s})$ is the density of the sea quarks and $\Delta \equiv (u+\overline{u})-(d+\overline{d})$ is the difference of up and down quarks in the proton.

The parton densities are defined at a starting Q^2 value, Q_0^2, like given in Eq. 1.21 and used together with the DGLAP evolution equations to predict cross sections of a whole host of processes. The parameters are then fitted by comparison with data. The data include inclusive DIS data from fixed target experiments and the HERA experiments and jet production data in $p\overline{p}$ from the Tevatron experiments. The actual choice of which data to include in these fits and the value of Q_0^2 gives room for variations in the extracted parton densities. The analyses presented in later chapters will make use of four different sets of parametrisations. The first of these sets is the result of the ZEUS fits [10] on their own data and fixed target results on deep inelastic scattering, necessary to constrain the value of the high x structure of the proton. The second set is from Glück, Reya and Vogt, the GRV98 set [11]. The fit was performed on the same data set as the ZEUS fit, but also includes the H1 structure function measurement and Drell-Yan muon pair production data. This set distinguishes itself from others by the fact that the sea quark density is created purely dynamically. To do so, the authors start the evolution at a small starting scale, with a vanishing sea quark density. The last two PDF sets are both from the CTEQ consortium. The CTEQ5 parton density [12] is of the same generation as the GRV98 and ZEUS94 sets. The nominal CTEQ5 density is a ZM-VFNS set, but they also provide a pure fixed flavour number scheme set: CTEQ5F3. The gluon densities of the three aforementioned sets are compared in Fig. 1.5(a) for two values of Q^2 and over a wide range in x. Differences between the sets only become visible for $x < 10^{-3}$.

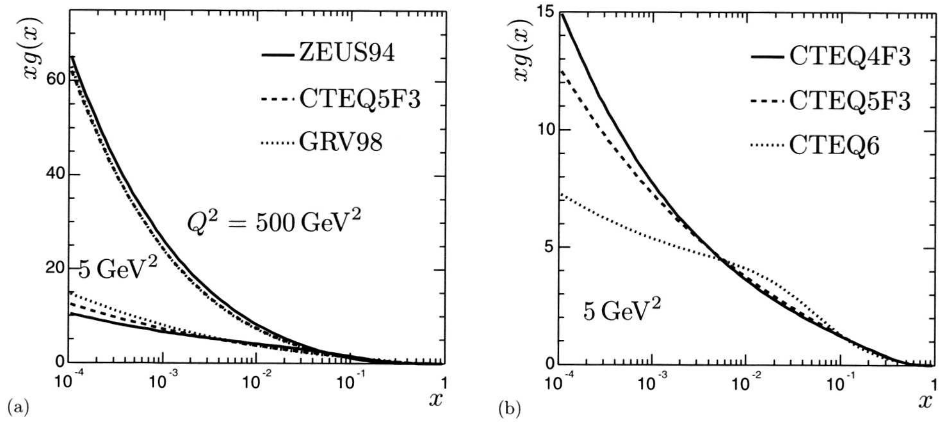

Figure 1.5: *(a) Comparison between three PDF-sets from the same generation: ZEUS94, CTEQ5 and GRV98. The gluon distribution is shown for $Q^2 = 5(500)$ GeV^2 by the lower (upper) curves. (b) Change in the fitted gluon density over time, for the CTEQ family of parton densities. The gluon densities of CTEQ4F3, CTEQ5F3 and CTEQ6 are compared for $Q^2 = 5$ GeV^2.*

At high Q^2 the ZEUS fit systematically has an enhanced gluon density, but follows the same shape as the CTEQ5 and GRV98 gluon densities.

The CTEQ6 set, from 2001, is the most recent of all sets presented here. It includes the 1996-1997 inclusive F_2 data from HERA but also the high E_T-jet data from Tevatron. This last dataset has quite a large impact on the gluon distribution (Fig. 1.5(b)) which becomes harder as a result. This change affects directly the prediction for the visible charm cross section.

The four PDF sets are compared in Tab. 1.1 where the parameters most important for heavy quark production are summarised.

Table 1.1: *A comparison of parameters relevant to heavy quark production from parton densities.*

PDF Set	Q_0^2(GeV^2)	m_c(GeV)	m_b(GeV)	**Flav.Scheme**
CTEQ5M [12]	1.0	1.4	4.5	ZM-VFNS
CTEQ5F3	1.0	1.4	4.5	FFNS
CTEQ6 [13]	1.3	1.3	4.5	ZM-VFNS
GRV98 [11]	0.4	1.4	4.5	FFNS
ZEUS94 [10]	7.0	1.5	5.0	FFNS

1.6. Alternative QCD evolution schemes

The DGLAP scheme for QCD evolution is not the only one. In this section, two (prominent) other schemes are described here. They will be compared to the DGLAP evolution, followed by some discussion on the merits and (lack of) uses of the methods.

BFKL

An (almost) completely orthogonal approach to parton density evolutions is given by the BFKL equations. This work of Kuraev, Lipatov and Fadin [14] and additionally by Balitski and Lipatov [15] is based on the summation of terms in $\ln 1/x$, rather than leading $\ln Q^2$ as for DGLAP. The BFKL approach uses an unintegrated gluon density, $\tilde{g}(x', k_T)$ which is convoluted with a hard scattering coefficient $\mathcal{C}(x/x', Q^2, k_T)$. The gluons and partons in the interaction are allowed to be off their mass shell, unlike the DGLAP case.

CCFM

Both the DGLAP and the BFKL methods only sum over one particular leading behaviour of the evolution problem to obtain their results. A complete (infinite order) calculation should take both the terms in $\ln Q^2$ and in $\ln 1/x$ and sum over them. To accomplish this, Ciafaloni [16] and Catani, Fiorani and Marchesini [17] introduced angular ordering for the emitted gluons. The maximum allowed angle is defined by the hard scattering, where the quark pair is produced. This is combined with the unintegrated gluon densities and off-shell partons, *a lá* BFKL. This method seems very promising, as it can (approximately) reproduce the DGLAP and BFKL equations when taking the appropriate limits.

Comparing the methods

The DGLAP equations have been extended to next-to-leading order and work is well under way, by Vermaseren, Moch and Vogt [18], to expand it to the next-to-next-to-leading order (NNLO). The NLO-DGLAP evolution can reproduce the ZEUS and H1 measurements of the inclusive structure functions, see [19, 20].

The next-to-leading log term of the BFKL kernel has also been calculated, but was found to be comparable in size and opposite in sign to the leading log contribution [21]. This clearly complicates the interpretation of the BFKL evolution, opposed to the DGLAP approach where each next order contributes less than the previous.

In Fig. 1.6 the evolution direction of the three methods is shown in the $1/x$-Q^2 plane. This picture makes very clear that CCFM holds a lot of potential as QCD evolution kernel. Being the youngest of the three evolution kernels, it is also the least explored. The CCFM approach still holds several problems that need to be solved before it can really be compared to data.

Finally, the fact that there is a full NLO-pQCD calculation for heavy quark production in DGLAP NC-DIS available (Sec. 1.4) makes that the focus of the theory-data comparisons in this thesis will lie on the DGLAP-type of parton evolution.

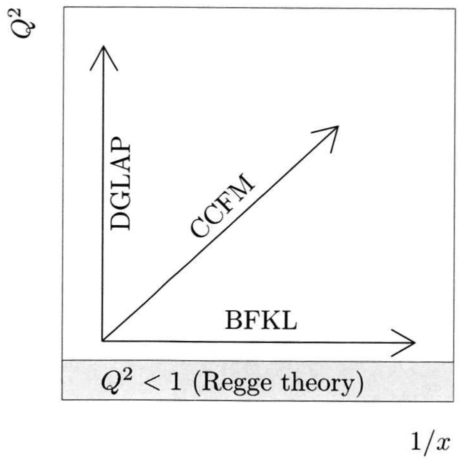

Figure 1.6: *Schematic overview of the effective difference between the three evolution schemes. The direction of evolution of the structure functions for the DGLAP, BFKL and CCFM methods is shown in the $1/x - Q^2$ plane.*

1.7. Final remarks

The theory described in this chapter will return in the comparison with the measurement presented in chapter 6. The differential cross sections will be compared to predictions from the calculation of the boson-gluon fusion process at next-to-leading order. From the measured double differential cross section $F_2^{c\bar{c}}$ will be extracted and compared to predictions from DGLAP structure functions and the alternative parametrisations described in the previous section. The discrepancies between the predicted DGLAP cross sections and the measurements are taken up in chapter 7. There, the ZEUS and H1 data on NC-DIS charm production will be fitted to DGLAP-predictions. This will lead to a quantitative answer for the question whether DGLAP-pQCD can describe todays charm production.

CHAPTER 2

Monte Carlo simulation

In this chapter the different Monte Carlo simulation programmes and their uses will be discussed. Basically the Monte Carlo programmes fall into two distinct categories. One category is used for understanding the acceptance of semileptonic charm events and the determination of backgrounds from processes other than semileptonic charm that appear in the measured electron sample. The second category, which contains only the HVQDIS programme, is used to compare the NLO QCD calculation of charm production to the measured visible cross section of semileptonic charm.

2.1. Factorisation and physics event generation

In the Monte Carlo programmes an attempt is made to simulate, with the highest possible degree of accuracy, the measured data. All the programmes assume that a particular physics channel can be built from three ingredients.

- The initial state, with the proton described by parton density functions and the electron.
- The hard scatter described in terms of quarks and gluons interactions
- The final state fragmentation and hadronisation where hadrons are formed by combining quarks and anti-quarks into colourless hadrons.

This scheme assumes implicitly that any physics process can be factorised into the mentioned processes and that these can be independently calculated.

The assumption of factorisation for physics processes such as *ep*-scattering allows the generation of 'events' in these independent stages. This chain of factorised subprocesses is illustrated in Fig. 2.1 and given by the following.

1. Selection of the particles involved in the interaction.
   In the case of a positron this is trivial: the positron itself, with properties based

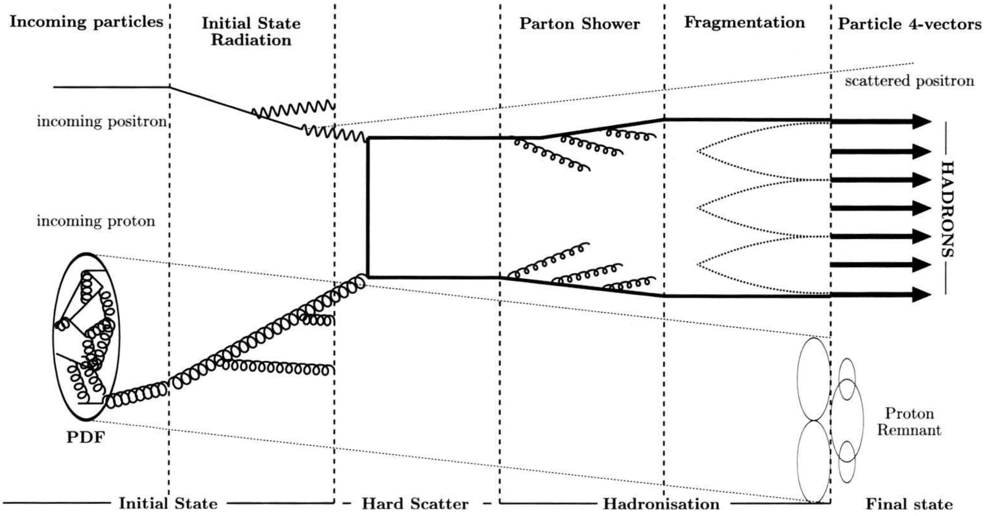

Figure 2.1: *A schematic overview of the Monte Carlo generation of a physics event.*

on the beam parameters. For the proton a parton is taken out of the proton structure, based on the (input) parton density functions.

2. Initial state radiation (ISR)
   Before entering the hard interaction electrons can, and typically will, radiate photons. The QED radiation by the electron is of importance for HERA physics, as it disturbs the kinematics of a event. It is important to have a detailed description of these effects. The initial state gluon radiation is handled as part of the parton shower (4) and is included to simulate the effects of the NLO hard scatter.

3. Hard Scatter
   The hard scatter is calculated from leading order (LO) matrix elements. It only encompasses the interaction between a parton from the proton with the exchanged photon.

4. Parton showering
   The quarks (and gluons) that are available after the hard scatter radiate secondary partons, following the QCD splitting functions described in Sec. 1.3. The splitting functions are completed by their QED counterparts. This process, which can create a tree of newly created partons is stopped at some lower scale μ_F, which is typically taken to be around 1 GeV^2. This stage is used to create a colour-rich environment that can be used to produce the final state hadrons by using the fragmentation algorithms. There are two commonly used methods to do this parton showering. Matrix Element Parton Showers (MEPS) being the first and the colour dipole model (CDM) [22] the second.

5. Fragmentation
   In the fragmentation stage the partons created in the parton shower stage are

transformed into colourless hadrons. This is done by connecting a colour string between two partons. The colour string then produces in a controlled manner extra quarks that dress up the *hard* initial partons into hadrons and yield additional hadrons. The string model used for fragmentation [23] is the Lund fragmentation model. In section 2.3 this topic will be extensively reviewed.

Most Monte Carlo generators include the option to decay short-lived particles. Typically those particles that (should) decay before reaching active detection volumes are handled by the Monte Carlo programmes, while those that decay in the active volume are handled by the detector simulation software. After completing this chain, there will be a (large) list of particles that can be passed through detector simulation. The larger part of these particles will be pions, kaons and protons.

2.2. Leading order Monte Carlo event generators

Leading order Monte Carlo event generators are used to generate completely evolved interactions. The output are events, collections of hadron four vectors, which can subsequently be passed through detector simulation programmes. These generators start with the evaluation of the double differential cross section in Q^2 and y. This is calculated using the LO matrix element of the interaction under study and a parametrisation of the parton density functions. This double differential cross section is used as probability function for the event generation: Q^2 and y are generated according to the calculated distributions. The integral of the calculated cross section is used in the determination of the Monte Carlo luminosity equivalent: $\mathcal{L}_{\mathrm{MC}} = N_{\mathrm{MC}}/\sigma_{\mathrm{MC}}$, where N_{MC} is the total number of generated events. This scale is important when directly comparing distributions from data to the Monte Carlo prediction, or when Monte Carlo events are used for background subtraction.

For the analysis of charm production two such programmes are used: one programme simulates generic DIS events and is used as check on the DIS event selection (chapter 4), while the second is used to specifically generate heavy quark events. The latter is used to determine detection efficiencies for charm mesons and to estimate the background due to beauty production (chapter 6).

2.2.1. QED radiation

The Monte Carlo generators DJANGOH and RAPGAP, described in the next sections, both use the HERACLES 4.5.2 [24] programme to simulate the initial state QED radiation. HERACLES calculates the probability for this radiation from the leading order electro-weak matrix elements. The results of this programme have been compared with higher order calculations of the radiation cross section and found to be in agreement at the percent level. For heavy quark measurements with the statistical accuracy expected from the data samples, this means that the effects induced by the initial state radiation of the electron are well under control.

2.2.2. Generic DIS: DJANGOH

The generic neutral current DIS events were generated with DJANGOH 6.24 [25]. The sample used is a subsample of the one used in the ZEUS inclusive-F_2 analysis [26]. The DJANGOH programme interfaces the HERACLES programme to the LEPTO 6.5 [27] package. LEPTO is responsible for the hard scatter part of the simulation. The parton showering is done through the ARIADNE 4.08 [28] programme that is incorporated in LEPTO. ARIADNE is an implementation of CDM [28]. The fragmentation is performed with the default Lund-string fragmentation routines of JETSET 7.4 [29]. The parton distribution functions were taken from the CTEQ4D [30] set.

2.2.3. Heavy quark production: RAPGAP

For the simulation of specific heavy quark production events the RAPGAP [31] programme was used. The reason for using a different Monte Carlo generator for the heavy quark events is based on an analysis of the mixture of produced charmed mesons [32]: RAPGAP produces a mixture that approximates best the measured mixture [33].

RAPGAP uses the HERWIG [34] code to generate heavy quarks via the boson-gluon fusion process. The parton distribution functions in this case were taken from GRV98. HERACLES is again used to generate the QED radiation. The final state radiation is simulated using leading log parton showers. RAPGAP also uses JETSET to perform the hadronisation. The heavy quark fragmentation was performed according to the Peterson function (Sec. 2.3.2). As these events were specifically used to determine the efficiency of detecting a charm or beauty meson within a DIS event through its semileptonic decay, all events generated with RAPGAP were required to have at least one heavy hadron decaying semileptonicly (either e^+ or e^-).

2.3. Fragmentation

After the hard scatter the produced quarks need to be transformed to colour neutral hadrons. This transformation is initiated by allowing the quarks to radiate gluons, which subsequently produce more gluons and quark-antiquark pairs. Two models are used for this process. The colour dipole model, where gluons are radiated from extended expanding colour dipoles and the MEPS model, which used explicit QCD matrix element calculations for hard gluon radiation and a leading logarithmic approach for the softer gluon radiation. This process is terminated when the relevant scale of the process falls below a value of 1 GeV^2. At this point the coloured partons are combined with colour strings to form colour neutral objects, which are then transformed into hadrons, using the string or Lund fragmentation [23].

2.3.1. String or Lund fragmentation

In the *string* or *Lund* [23] fragmentation model a colour string connects two objects that together could give a colourless object. The string is allowed to break up, allowing $q_i\bar{q}_i$ pairs to appear anywhere on the string. The pairs are then recombined with adjacent formed quark pairs to form bound states of $q_i\overline{q}_j$ or, more rarely, baryonic $q_iq_jq_k$ states.

The $q_i(\overline{q}_i)$ are given some finite transverse momentum with respect to the string. The transverse momentum is compensated locally between the $q_i\overline{q}_i$-pair. The transverse momentum distribution is generated according to

$$P(p_\perp) \propto e^{-\frac{\pi m_\perp^2}{\kappa}}, \text{ with } (m_\perp^2 = m^2 + p_\perp^2) \tag{2.1}$$

where κ is the *string tension* and $m_\perp$ is the transverse mass of the particle. When a quark q_i is combined with some $\overline{q}_j$ to form a hadron, that hadron takes some fraction of the available momentum/energy with it. This fraction is given by z. Various definitions of z can be used; in the Lund scheme the following is used

$$(E + p_z)_{hadron} = z(E + p_z)_{quark} \tag{2.2}$$

from which follows that z is the fraction of the light-cone momentum. The probability density function of z is called the *fragmentation function.* For light quarks this function is given by

$$D(z) \propto \frac{(1-z)^a}{z} \exp\left(-\frac{bm_{h,\perp}^2}{z}\right) \tag{2.3}$$

where a and b are free parameters that need to be adjusted to bring the fragmentation in agreement with measured data. The fragmentation function takes the mass of the formed hadron explicitly into account. The PDG quotes values of $a = 0.11$ and $b = 0.52\,\text{GeV}^{-2}$ (Ch. 15 of Ref. [33]).

2.3.2. Heavy versus light quark fragmentation

Experimentally it was found that the fragmentation of charmed and b-mesons is harder than that of the light quark states. To accommodate for this several new formulations of the fragmentation function were derived. These functions differ from the light quark fragmentation functions in that the heavy quark will transfer most of its energy and momentum to the formed hadron.

The proper description of the fragmentation is crucial as this provides the translation from the calculable production of heavy quarks to the charmed hadrons that are measured in the detector. To illustrate: a significant part of the total charm production cross section remains invisible in the experiment, due to necessary kinematic constraints on the charmed final state. Typically about 10% of the total cross section is *a priori* detectable. Choices in the fragmentation model can change p_T and η (p and θ) distributions which directly will affect the fraction of the total cross section which is available to the experiment.

Peterson et al.

The most commonly used function to describe heavy quark fragmentation is the one as proposed by Peterson, Schlatter, Schmitt and Zerwas [35] (henceforth denoted as Peterson). The *ansatz* at the basis of this function is that almost all the energy of

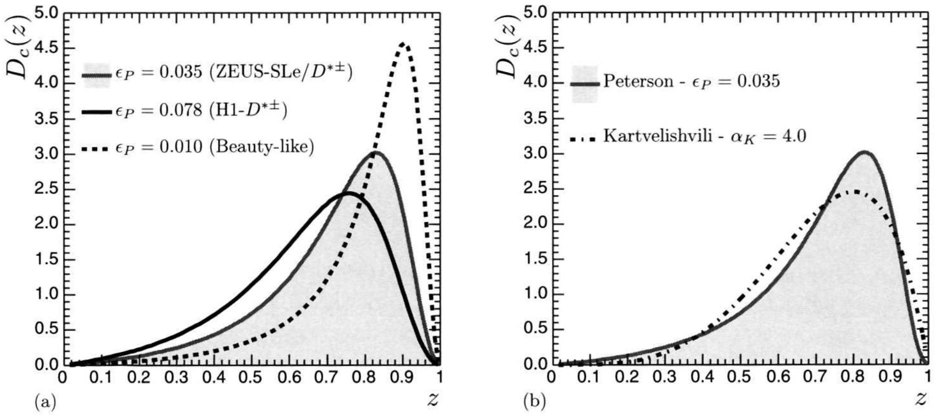

Figure 2.2: *(a) The normalised Peterson fragmentation function for D^* fragmentation as used by ZEUS (filled) and H1 (solid line) and a function with $\epsilon_P = 0.01$, which is approximately correct for beauty production. (b) The Peterson (filled) and Kartvelishvili (dash-dot) fragmentation functions compared. The parameters used are $\epsilon_P = 0.035$ and $\alpha_K = 4.0$.*

that heavy quark will be passed on to the formed meson. The functional form is given by

$$D_c^{Pet}(z) \propto \frac{1}{z} \frac{1}{(1 - \frac{1}{z} - \frac{\epsilon_P}{1-z})^2} \tag{2.4}$$

where ϵ_P, the only free parameter, is typically in the range 0.01 - 0.10 [36]. This parameter is related to the heavy quark mass in that $\epsilon_P \sim m_q^2/m_Q^2$, where m_q denotes the mass of the light quark forming the hadron and m_Q that of the heavy quark. Masses of light quarks are not well defined so ϵ_P remains a free parameter. One can however derive a relationship between the ϵ_P for charm and beauty production: $\epsilon_P^b \simeq (m_c/m_b)^2 \epsilon_P^c$. The Peterson fragmentation function peaks for $z \simeq 1 - 2\epsilon_P$. Comparing the charm and beauty fragmentation, Peterson fragmentation produces a harder fragmentation for beauty: the function peaks closer to $z = 1$.

In Fig. 2.2 the function is shown for three cases for the ϵ_P parameter, the nominal values as used by the ZEUS and H1 experiments for D^*-production and an approximate value for beauty fragmentation where the latter is harder.

Kartvelishvili et al.

A second form for the heavy quark fragmentation function is given by Kartvelishvili, Likhoded and Petrov [37] (from now Kartvelishvili). This function is given by

$$D_c^{Kart}(z) \propto z^{\alpha_K}(1 - z) \tag{2.5}$$

with the only tunable parameter being α_K. The functional form is deduced from a Regge theory based description of the fragmentation. From the analysis the authors conclude that the value of α_K should be of the order of 3 for charm fragmentation.

Table 2.1: *Comparison of the packages used by* DJANGOH *and* RAPGAP *in the event generation.*

sub process	DJANGOH	RAPGAP
(I/F)SR	HERACLES	HERACLES
Hard scatter	LEPTO	HERWIG
Parton shower	ARIADNE	ARIADNE
Hadronisation	JETSET	JETSET
Parton Density	CTEQ4D	GRV98-DIS
SLe selection	No	Yes

The Kartvelishvili fragmentation function is compared to the Peterson distribution in Fig. 2.2(b). The Kartvelishvili function leads to a somewhat broader distributions than the Peterson function and peaks at a lower value of z. It therefore produces a somewhat softer distribution of charmed mesons. It should be noted however that the value of $\alpha_K = 4.0$ (used in the figure) has not been optimised to reproduce experimental results, but rather has been chosen such that the shape most closely approximates the Peterson-curve.

2.4. Wrapping up leading order Monte Carlo

2.4.1. Comparison

Table 2.1 gives an overview of the different packages used by the two event generators. The main difference lies in the hard scatter (LEPTO vs. HERWIG) where the latter uses the leading order matrix element of boson-gluon fusion to generate heavy quarks. In the RAPGAP case the fragmentation of charmed quarks was done specifically with the Peterson model with $\epsilon_P = 0.035$.

2.4.2. Monte Carlo event sample

Of the events generated with RAPGAP only those that had a semileptonic electron or positron in the final state were accepted for detector simulation. This gave a reduction of 5.51 (2.68) from the inclusive charm (beauty) event sample to semileptonic only. With these two generators the event samples of Tab. 2.2 were generated, all with a lower bound on $Q^2 > 0.5\,\mathrm{GeV}^2$. The equivalent luminosities of the heavy quark samples have been corrected for the use of the semileptonic selection.

The Monte Carlo event samples were subsequently fed through a chain of detector response and trigger simulation and the standard offline reconstruction software. The simulation of the ZEUS detector response is done by the MOZART program, which is the GEANT 3.14 [38] implementation of the ZEUS detector. The trigger response is simulated by the ZGANA package. The output is identical to that of data events, with the addition of Monte Carlo truth information and therefore can be fed through the same analysis code as the data.

Table 2.2: *Overview of the Monte Carlo event samples used in the analysis presented in this thesis. The luminosity equivalents are based on the cross sections reported by the generators.*

type	m_Q (GeV)	N_{acc}	N_{gen}	$\mathcal{L}_{MC}$ (pb^{-1})
DJANGOH NC-DIS	-	2.5M	2.5M	1.19
RAPGAP $c \to e^+$ and *c.c.*	1.5	2.0M	11.0M	130.88
RAPGAP $b \to e^-$ and *c.c.*	5.0	1.0M	2.7M	454.48

2.5. HVQDIS: cross sections at next-to-leading order

The HVQDIS [39] programme is the FORTRAN implementation of the fully differential heavy quark structure functions in the fixed flavour number scheme. These differential structure functions ($dF_k/dM_T^Q dy^Q$) were calculated by Harris and Smith [40] who are also the principle authors of the HVQDIS program. The programme evaluates the four dimensional integral over Q^2, y, M_T^Q and y^Q - the heavy quark transverse mass and rapidity in the $\gamma^* p$ c.m. frame. The result of this calculation is the total cross section for charm or beauty production in a given kinematic range. The fact that the structure function $F_2^{c\bar{c}}$ has been extended to be differential in M_T^Q and y^Q is used to obtain the cross section distribution in terms of the kinematic properties of the produced heavy quark pair. The calculated total cross section can be studied by distributions differential in the hard scatter kinematics (Q^2, x, y, W) or the properties of the produced quarks. In order to directly compare the calculation with the measured distributions, the properties of the quark-pair are represented in terms of two four-vectors. These four vectors can be passed through fragmentation code. This transforms the two quark four vectors into the four vectors of D/B-mesons. These mesons can subsequently be decayed semileptonicly. It should be emphasised that *only* the two quark four vectors are available for hadronisation. There is no simulation of the parton showering and thus no jet information is available.

2.5.1. Numerical methods

Integration method

The calculation is based on the (quadruple) differential cross section

$$\frac{d^4\sigma}{dQ^2 dy dM_T^Q dy^Q} \propto \sum \frac{d^2 c_i}{dM_T^Q dy^Q} \otimes q_i$$

where the sum runs over all the coefficient functions and the appropriate NLO parton densities. The results of the calculation always depend on the input parton densities used for the calculation. This may give rise to slightly different results, especially in terms of the total cross section number. The effect of this is studied further in chapter 6.

The integrand is evaluated by an adaptive sampling Monte Carlo integration, using the VEGAS [41] routines. The procedure starts of with N points, or hyper-volumes, distributed uniformly in the 4-dimensional hyper-cube, effectively representing a hyper-volume. The distribution of the hyper-volumes is then optimised such that each point represents the same approximate cross section. This is obtained by evaluating the integral M times and subsequently rearranging the points according to the functional form of the integrand after each iteration. To obtain the final result, the number of points is doubled (to $2N$ points) and the integral evaluated $2M$ times. The cross section is given as the average of the $2M$ evaluations. The leading and next-to-leading order contributions to the cross section can be evaluated either separately or together.

Heavy quark four vectors

Events are generated according to distributions which approximate the calculated cross section. The output consists of the value of Q^2 and y of the event, the four vectors of the heavy quark and antiquark and an event weight which corresponds to the cross section for the generated configuration. The leading order and next-to-leading order parts of the cross section are generated in separate events and so the weights can be negative. Finally event selection cuts are performed on the true kinematics of the event and cuts are made on the D-meson or semileptonic electron momenta and directions. Single and double differential distributions are then obtained by histogramming the accepted events using the event weight.

The quark vectors are produced in the $\gamma^* p$ center-of-mass frame. The vectors are subsequently boosted to the laboratory frame. Here they are transformed into D-meson vectors using the Peterson fragmentation function. The scaling variable z (of the fragmentation function) is applied on the spatial component. The energy is obtained by then requiring $E^2 = M_D^2 + p^2$.

The semileptonic decay is generated in the D-meson rest frame. The decay energy is distributed according to input from JETSET [32]. This distribution has been cross checked with HERWIG and was found to be in good agreement [42]. The spatial momentum is distributed isotropically in the D-meson rest frame. The initial D-meson four vector finally is used to boost the electron to the laboratory frame.

2.5.2. Input parameters

HVQDIS has many free parameters that need to be set to obtain sensible results. These parameters include the number of points and iterations of the hyper-grid used in the evaluation of the integrand, the input parton density function, kinematic range of interest and parameters related to the (fragmentation) of the heavy hadron (hadron mass, ϵ_P). The default implementation of HVQDIS includes interfaces to the CTEQ4, CTEQ5, GRV94 and GRV98 parton density functions.

Choice of integration parameters

As part of the process of understanding the HVQDIS program, studies have been performed to determine the optimal setting of the integration parameters: the number of iterations and the number of sampling points.

By comparing the (simultaneously) calculated cross section in three regions in Q^2 and y for a fixed set of parameters, one can get an idea of the convergence of

Table 2.3: *Calculated cross sections for different choices of integration points for the leading order (LO) and next-to-leading order (NLO) contributions. The number of points are given in thousands (10^3). The shaded cells indicate where the numerical integration has stabilised.*

	Total cross section (nb)					Visible cross section (pb)				
1 LO / NLO	10	20	40	80	160	10	20	40	80	160
15	4.60	4.86	4.85	4.77	4.89	61.6	50.0	62.9	70.4	60.6
30	4.89	4.87	4.82	4.86	4.88	61.1	60.1	61.4	67.8	76.5
60	4.91	4.89	4.92	4.92	4.92	58.8	60.8	60.8	62.0	59.6
120	4.90	4.90	4.93	4.91	4.93	59.9	62.4	63.2	62.7	67.1
240	4.84	4.85	4.92	4.91	4.91	62.0	61.8	62.9	60.2	63.8
2 LO / NLO	10	20	40	80	160	10	20	40	80	160
15	4.35	3.42	4.04	4.08	3.66	67.4	62.4	86.2	77.1	80.9
30	4.08	3.83	3.92	3.74	3.79	78.3	84.3	80.5	75.8	76.5
60	3.80	3.86	3.83	3.73	3.85	88.3	56.3	70.9	80.5	77.5
120	3.81	3.82	3.83	3.86	3.81	77.2	80.5	80.0	80.1	84.4
240	3.78	3.80	3.84	3.81	3.84	83.5	80.0	77.9	80.1	83.8
3 LO / NLO	10	20	40	80	160	10	20	40	80	160
15	3.49	2.80	3.32	3.37	3.35	56.7	56.0	58.4	61.8	148.2
30	3.46	3.40	3.34	3.56	3.41	54.8	60.7	55.6	56.3	55.9
60	3.04	3.40	3.36	3.36	3.53	53.1	56.3	57.8	62.9	63.0
120	3.40	3.35	3.35	3.41	3.62	54.6	58.8	61.2	62.7	66.8
240	3.33	3.23	3.32	3.35	3.33	56.7	57.2	58.2	59.6	59.3

the integration procedure and also of the relative error on the final result. The test calculations were done using the CTEQ6 PDFs and the charm mass fixed to 1.5 GeV. The factorisation and renormalisation scales were chosen to be $\mu_{\mathrm{R/F}} = Q^2 + m_c^2$. Three bins in y were examined with $4 < Q^2 < 9\,\mathrm{GeV}^2$. The y ranges are given by

1 $0.03 < y < 0.12$

2 $0.12 < y < 0.30$

3 $0.30 < y < 0.70$

for which total and visible semileptonic charm cross sections were calculated.

The number of iterations for the integration was kept fixed, at 6(12) relaxation (integration) iterations for the leading order part and 12(24) respectively for the next to leading order contributions. The resulting cross sections are given in Tab. 2.3. The table shows that the convergence for the total production cross section (five columns on the left hand side) is achieved for a moderate number of sampling points, $N_{LO} = 40.000, N_{NLO} = 60.000$. For the visible cross section (five columns on the right hand side), this is however not the case, as large (statistical) fluctuations can still been seen between different settings at this point. Even taking four times as many points, both for N_{LO} and N_{NLO} the predicted visible cross sections are only stable

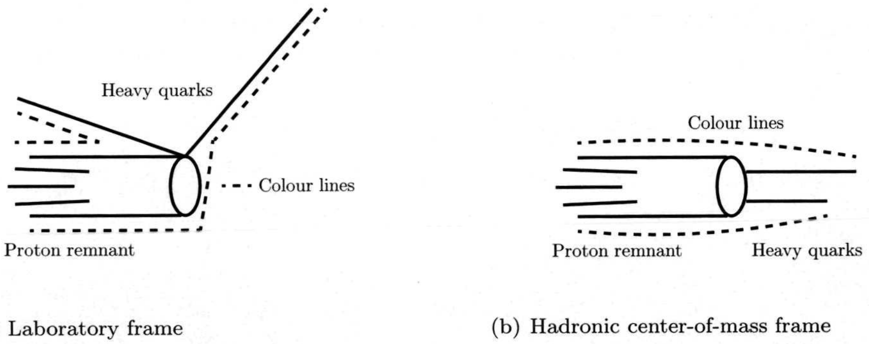

(a) Laboratory frame (b) Hadronic center-of-mass frame

Figure 2.3: *(a) Colour lines for fragmentation in the laboratory frame. (b) Colour lines for fragmentation in the hadronic centre of mass frame.*

at the 5% level. One therefor concludes that the visible cross sections calculated in this manner have an intrinsic accuracy limitation at the level of 5%.

2.6. Implemented improvements

2.6.1. Fragmentation

The original HVQDIS code adopts a very basic approach to fragmentation. Heavy quark fragmentation is performed based on the Peterson function and in the laboratory (LAB) frame. The fragmentation is applied on the spatial part of the quark four-vector only, while the energy of the resulting hadron is fixed to satisfy energy-momentum conservation. In other words, the fragmentation is applied according to

$$p_i^H = z p_i^c \tag{2.6}$$

$$p_0^H = \sqrt{M_H^2 + p_i^H p_H^i} \tag{2.7}$$

where $i = 1, 2, 3$, gives the spatial coordinates and z is the fragmentation fraction which is distributed according to the input fragmentation function. However, the functional form of the Peterson function is derived in the *infinite momentum frame*. When trying to envisage the colour connections between the di-colour quark-(anti)-quark and the proton remnant it becomes clear that the lines are not being stretched out, as in the infinite momentum frame, but are rather warped as shown in Fig. 2.3(a). The notion of a rubber band that is stretched until it breaks will fail for the colour line on the left hand side. The colour line will break, but it will behave differently than the colour line on the right hand side, which has a configuration that has a better resemblance to the infinite momentum frame. A good approximation of the infinite momentum frame is found in the Hadronic Centre of Mass (HCM) or $\gamma^* p$ frame (Fig. 2.3(b)). The di-quark pair is found back-to-back with the proton remnant. The

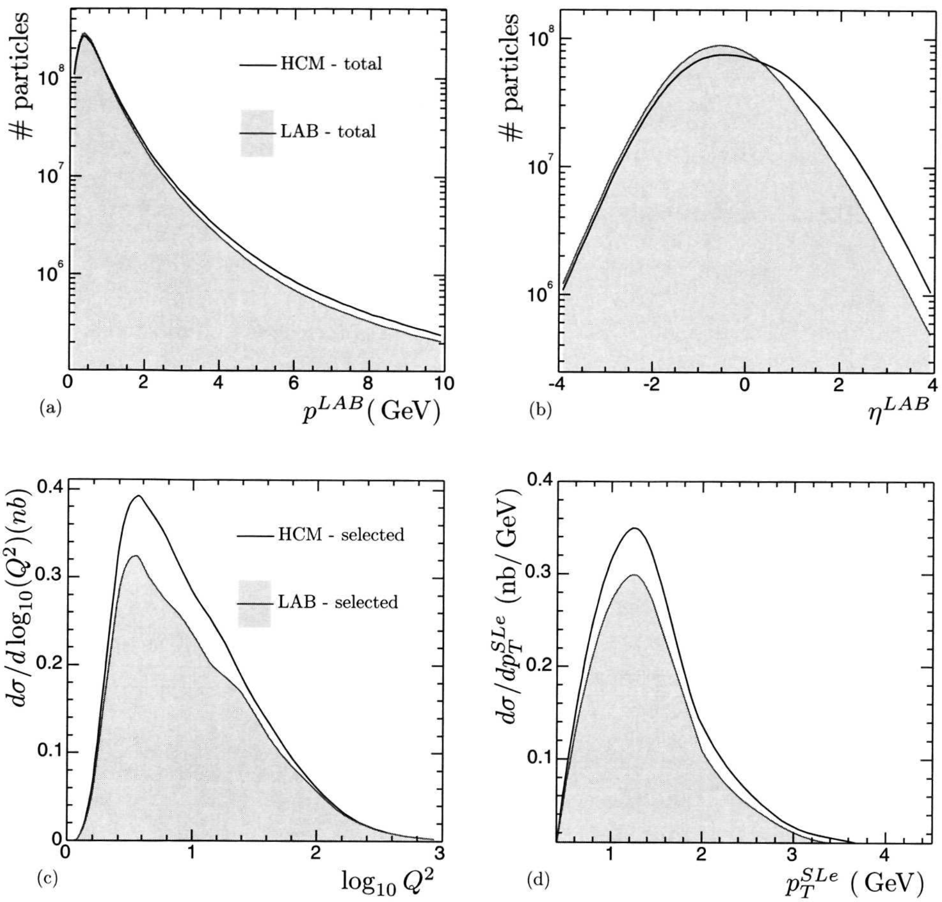

Figure 2.4: *(a) Momentum and (b) η of the semileptonic electron after fragmentation in LAB (solid) and HCM (line) frame. (c) Visible cross sections differential in $log_{10}(Q^2)$ and (d) $d\sigma/dp_T$.*

colour lines stretch out from the two heavy quarks to the proton remnant and are practically straight[1]. The difference between fragmentation in the two frames can be analytically derived [43] for $m_H \simeq m_Q$ and gives a energy difference of

$$\Delta E = \frac{m_Q^2}{2|\vec{p}_Q|} \sinh(\eta) \frac{1-z^2}{z} \tag{2.8}$$

for small $m_Q/|\vec{p}_Q|$. Figure 2.4 shows the effect of the choice of either frames on several distributions, for semileptonicly decaying D-meson, based on CTEQ6 with

---

[1] The 'kink' is an artifact of the way that the parton configuration in this frame has been represented, and does not imply an actual 'bending' of the colour line.

Figure 2.5: *The energy of decay electrons (dashed line) compared to the subset of electrons that passed kinematic selection cuts in the laboratory frame ($1.2 < p < 5.0\,GeV, 0.65 < \theta < 2.5$) (solid line). The scale difference between the two distributions is ≈20. The selected electrons predominantly come from the upper half of the initial distribution.*

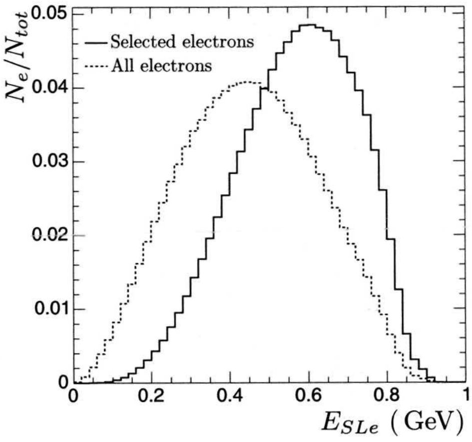

$m_c = 1.3\,\text{GeV}$. The visible cross section is enhanced by ≈10% for low-Q^2 when using the hadronic centre of mass frame.

2.6.2. Semileptonic decay of charmed hadrons

The production of semileptonic electrons is simulated using the decay energy distribution as given by JETSET. In JETSET this distribution is generated by assuming a single decay matrix element given by

$$|\mathcal{M}|^2 = (p_D p_e)(p_\nu p_h) \tag{2.9}$$

where p_D, p_e, p_ν and p_h are the charmed meson, decay electron, decay neutrino and decay (light) hadron four vectors respectively. Figure 2.5 shows the distribution obtained in this way. It is interesting to note that those electrons which pass the experimental cuts mostly originate from the upper end of the spectrum, also shown in Fig. 2.5. This means that the visible cross section is particularly sensitive to the modelling of the high energy part of the decay distribution.

This part of the distribution is sensitive to the particular decay of the meson. Specifically the exclusive decays to scalar mesons produce a different distribution than the decays to vector mesons. In turn the ratio of vector to scalar mesons in the decay depends on the identity of the decaying charm meson. A detailed treatment of semileptonic decay of various charm mesons has been given by Scora [44]. The results of this analysis have been implemented in the programme EVTGEN [45]. Figure 2.6(a-c) show the decay distribution of the D^0,D^+ and D_s^+ as generated by EVTGEN compared to the standard distribution used in HVQDIS. Because of the sensitivity of the results to the modelling of the decay it was decided to implement the Scora decay distributions in HVQDIS. To this end one must first determine the mixture of mesons produced in the fragmentation of the charm quark.

D-Meson mixture

The meson mixture has been derived by counting the decay modes of the higher states (D^*, D^{**}) into the ground state D-mesons. The JETSET ratio of $u : d : s = 3 : 3 : 1$ for the production of light quarks in fragmentation was assumed. Following this, one finds that the mixture of $\overline{D}^0$,D^- and D_s^- is given by,

$$F_{D^-} = \frac{1 - F_b - F_s}{2}(\frac{F_H}{2} + \frac{F_{H^*}}{3} + \frac{2F_{H^{**}}}{3}) \tag{2.10}$$

$$F_{\overline{D}^0} = \frac{1 - F_b - F_s}{2}(\frac{F_H}{2} + \frac{5F_{H^*}}{3} + \frac{4F_{H^{**}}}{3}) \tag{2.11}$$

$$F_{D_s^-} = F_s \tag{2.12}$$

$$\tag{2.13}$$

where

F_b = Fraction of charmed baryons
F_s = Fraction of $\bar{c}s$ mesons
F_H = Fraction of $L = 0$ mesons
= $1 - F_{H^*} - F_{H^{**}}$
F_{H^*} = Fraction of $L = 1$ mesons
$F_{H^{**}}$ = Fraction of $L = 2$ mesons

are the (experimental) input. The baryons contribute between 0 and 8% to the total hadron sample when generated with JETSET.

The fraction of $\bar{c}s$ mesons is obtained from the JETSET ratio for the light quarks. All excited states of $\bar{c}s$ decay finally into the D_s^-. The hadronisation fraction $\bar{c} \rightarrow D^{*-}$ is experimentally well established and found to be 0.255. As fragmentation is indifferent to u and d it follows that $F_{H^*} = 0.51$. Due to the mass differences of $D^{*\pm}$ and D^{*0} to the $D^{\pm}$ and D^0 states, the decays of D^* mesons predominantly produce D^0 mesons: $BR(D^{*\pm} \rightarrow^{(} \overline{D}^{)0}) = 55\%$ and $BR(D^{*0} \rightarrow D^0) = 100\%$. The number for $F_{H^{**}}$ is not so easy to derive. The Monte Carlo generator HERWIG yields 7% of mesons in this state, while RAPGAP has zero. Experimentally this fraction has been measured (with large errors) to be of the order of a few percent. Therefore, this fraction is set to 0.

Semileptonic branching ratios of D-mesons

The branching ratios of the three ground-state D-mesons have all been measured. The PDG quotes in its 2002 edition [33] the branching ratios given in Tab. 2.4. The inclusive branching fraction $c \rightarrow e + X$ has also been measured and is also given in Tab. 2.4.

By combining these branching ratios with one of the meson mixtures from Tab. 2.5 the relative contributions of the mesons to the total charm-electron signal is obtained. These ratios can subsequently be used to calculate the inclusive energy distribution of the semileptonic electrons. It should be noted that the branching ratio for D_s^- is very poorly measured. Therefore this branching ratio is determined from the given particle ratios and the inclusive $\bar{c} \rightarrow e^- X$ branching ratio. The used value of 11% is

Table 2.4: *Inclusive branching ratios of charmed mesons to electrons.*

Decay	Γ_i/Γ (%)
$D^- \to e^- X$	17.2 ± 1.2
$\overline{D}^0 \to e^- X$	6.9 ± 0.3
$D_s^- \to e^- X$	8.0 ± 6.0
$\bar{c} \to e^- X$	9.6 ± 0.4

Table 2.5: *Comparison of the effect of different choices for the mixture of meson states. The Monte Carlo generators* RAPGAP *and* HERWIG *are compared to the used set of choices. The last column gives the inclusive semileptonic branching ratio obtained from the given meson mixture.*

Model	F_B	F_s	$F_{H^{**}}$	F_{H^*}	F_{H^*}	F_{D^-}	$F_{\overline{D}^0}$	$F_{D_s^-}$	BR
RAPGAP	0.08	0.13	0.00	0.75	0.25	0.202	0.592	0.132	9.0%
HERWIG	0.02	0.13	0.07	0.40	0.53	0.282	0.509	0.132	9.2%
Used	0.08	0.13	0.00	0.51	0.49	0.263	0.529	0.132	9.7%

still in good agreement with the measured branching ratio. Table 2.5 gives the final numbers used in the subsequent analysis. Figure 2.6(d) shows the final total electron energy distributions obtained from these settings.

2.7. Comparing cross sections

A natural question now arises: how do the cross sections of HVQDIS compare to the cross sections of RAPGAP? The first are based on the NLO matrix element, the second on the leading order matrix element of boson gluon fusion with the kinematics modified by initial state parton showering. This question is relevant in two ways, which necessitates answering it.

First we compare the visible cross sections. The programs are expected to give (slightly) different results for this quantity. This is a direct consequence of the inclusion of an additional order of the perturbation series in the matrix element definition in HVQDIS.

By comparing the HVQDIS and RAPGAP predictions for this cross section for various bins in Q^2 any biases due to this effect can be evaluated. Table 2.6 gives the results for charm production cross sections, with the visible final state being chosen to be the semileptonic cross section of chapter 6. For these results, the proton structure functions from the CTEQ5F3 set were taken and m_c fixed to 1.50 GeV. The reason for the relative high charm mass lies in the fact that RAPGAP uses this mass natively. The comparison in the table shows that the two programs produce similar values for the visible cross section, although there is a tendency RAPGAPproduces a slightly less steep distribution in Q^2. From this it can be concluded that RAPGAP can be used for detection efficiency evaluation without biasing the signal

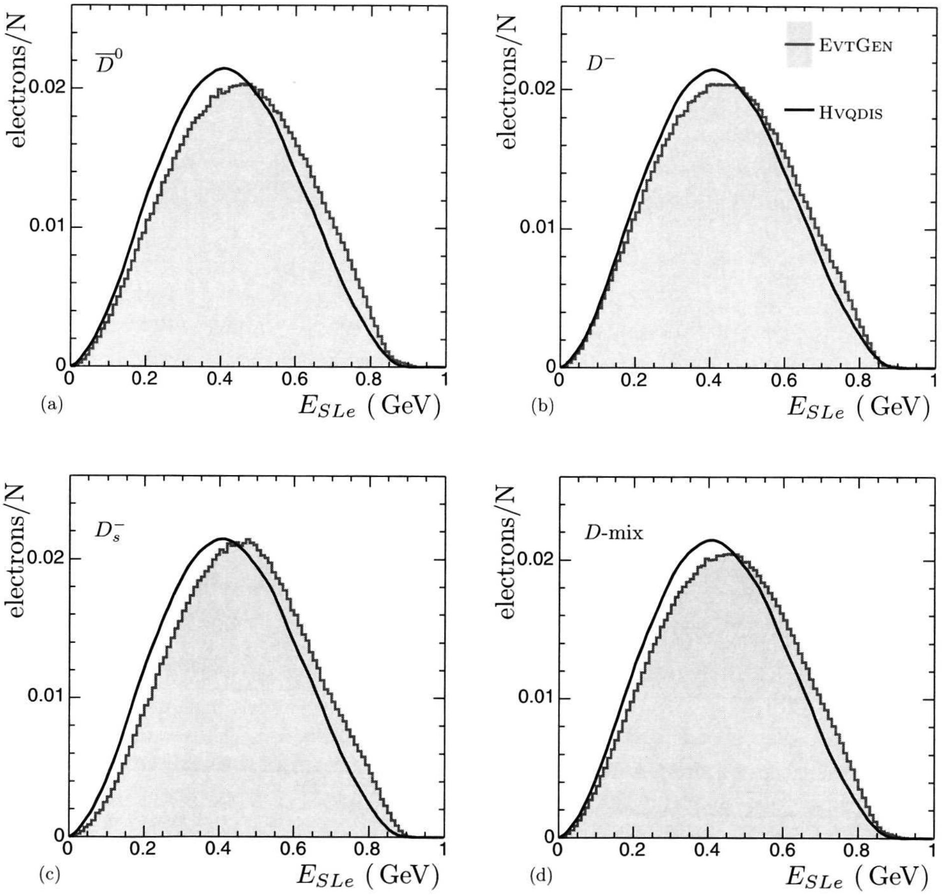

Figure 2.6: *The energy distribution of the semileptonic electron. The calculation of* EvtGen *for different charmed mesons is compared to the default* Hvqdis *implementation: (a) $\overline{D}^0$, (b) D^- and (c) D_s^-. (d) The combined energy distribution of the D-mixture given by Tab. 2.5 compared to the distribution used by* Hvqdis *in the simulation of the decay.*

Table 2.6: *The visible cross section for* HVQDIS *and* RAPGAP *for various bins in* Q^2. *All bins satisfy* $0.03 < y < 0.70$.

Q^2 range	HVQDIS	RAPGAP
2 - 4	12.8	10.8
4 - 9	10.7	10.0
9 - 15	4.4	4.6
15 - 25	2.9	3.2
25 - 40	1.7	2.0
40 - 70	1.2	1.5
70 - 130	0.7	0.9
130 - 1000	0.4	0.7

Second we estimate the contribution of $b\bar{b}$-production. Beauty will contribute to any charm measurement. The decay $b \to \bar{c}W^+$ gives rise to a charm component. For any experiment that attempts to measure direct charm production from a pure QCD process this is a background. For the measurement of charm production through the semileptonic decay it also contributes through the decay $\bar{b} \to cW^- \to ce^-\bar{\nu}_e$, which is a pure semileptonic decay of the b and which is very hard to distinguish from the charm decay. This beauty contribution needs to be subtracted using a Monte Carlo estimate. This estimate is directly proportional to the calculated production cross section and the accepted fraction of b-events:

$$N^b_{Bkg} = \frac{N^{acc}_b}{N^{gen}_{b\bar{b}}} \cdot \mathcal{L}_{data} \cdot \sigma^{gen}_{b\bar{b}} \tag{2.14}$$

where *gen* denotes the number at generator level, *acc* the number after applying selection criteria, and N_{Bkg} is the actual background estimate. It is in particular important that the calculated cross sections behave similarly for different regions of phase space (Q^2, y), such that there is no sensitivity to the edge of phase space.

To investigate this, the cross sections as determined by RAPGAP and HVQDIS are compared for various choices of phase space, both for charm and beauty production. The phase space definitions are given by combined Q^2-y ranges. In addition the events are counted that were generated by RAPGAP within the kinematic domain. The results are summarised in Tab. 2.7. The ratio between the two is practically constant, with HVQDIS predicting a 2% higher total production cross section than RAPGAP. The number of generated events is determined by applying cuts on the true kinematics of a sample of events generated in the first kinematic domain. This shows that the number of generated events indeed follows the calculated total production cross section. One concludes that the beauty background to the charm cross sections can be effectively determined with the Monte Carlo event sample.

Table 2.7: *Comparison of the total open beauty production cross section calculated by* RAPGAP *and* HVQDIS *for different kinematic regions. The beauty mass was fixed at 5 GeV together with the GRV98 PDFs.*

KINEMATIC RANGE							
$y_{\min}$	$y_{\max}$	$Q^2{}_{\min}$ (GeV^2)	$Q^2{}_{\max}$ (GeV^2)	σ_{RPG} (nb)	σ_{HVQ} (nb)	**Ratio**	**Events**
$3.0 \cdot 10^{-3}$	1.0	1.0	1000	0.784	0.805	1.02	323781
$1.0 \cdot 10^{-2}$	0.9	1.5	1000	0.670	0.685	1.02	277433
$3.0 \cdot 10^{-2}$	0.7	2.0	1000	0.521	0.529	1.02	214799

2.8. Summary

In this chapter an overview has been given of the Monte Carlo programs that will be used in the measurement of charm production through detection of the semileptonic electron. The process of fragmentation, and that of heavy quarks in particular, has been discussed in detail. The implementation of the NLO-pQCD calculations for heavy quark production in neutral current DIS, HVQDIS, has been highlighted in particular.

The use of the Monte Carlo programs breaks down into three separate targets. The DJANGOH Monte Carlo is used to examine the DIS event selection. The RAPGAP Monte Carlo is used to determine the detection efficiencies of semileptonic charm electrons. The programme HVQDIS is used to confront the measurement directly with QCD predictions that are the results of an exact calculation, unlike the event generators where phenomenological (data tweaked) models have to be used.

Several improvements to the HVQDIS treatment of the fragmentation and the semileptonic decay have been discussed. The choice of the frame of reference in which the fragmentation takes place is non-trivial. In fact, the predicted visible cross section is non-invariant to this. Performing fragmentation in the γ^*p frame rather than in the laboratory frame gives an increase of about 10% and 5% for the visible semileptonic and D^* cross section, respectively.

The implementation of the semileptonic decay of charm in JETSET uses a softer energy spectrum than what is obtained from direct calculations. By replacing the JETSET based HVQDIS implementation with the D-meson mixture weighted spectrum obtained from EVTGEN an additional 10% is gained in the visible cross section.

The effect of variations in the integration settings for HVQDIS has been studied as well. Based on these results the integration settings for the distributions shown in later chapters were chosen.

CHAPTER 3

The HERA accelerator and the ZEUS detector

In this chapter the electron-proton collider HERA is described including a short description of the experiments that use this machine. This is followed by a more extensive treatment of the ZEUS detector, in particular those detector components, used in the analysis presented in the following chapters, are discussed in detail.

3.1. The HERA accelerator

The Hamburg, Germany based Hadron Elektron Ring Anlage, or HERA, is an accelerator with colliding electron (positron) and proton beams. This makes it unique in the world, being the first machine to collide two different types of particles. The first collisions in the interactions points at HERA were recorded in 1991. In this thesis data of the 1996-1997 running period will be presented.

3.1.1. A short history

The experiments at HERA started data taking in 1991, after the commissioning of the accelerator. The first two years of data were taken with electron-proton collisions. In July 1994 the electrons were substituted by positrons and this has remained so until the end of 1997. The reason for this switch was inspired by the better lifetime of positron beams leading to better background conditions for the experiments. During this period the protons were accelerated to an energy of 820 GeV, and the positrons to 27.5 GeV. The resulting centre of mass energy of $\sqrt{s} = 300$ GeV offered many possibilities for measurements to study perturbative QCD and the structure of the proton. During the 1996-1997 running period HERA delivered a total integrated luminosity of $17 + 36 = 53$ pb^{-1} (Fig. 3.1(b)).

3.1.2. Physics programme

HERA hosts four experiments, as shown in Fig. 3.1(a).

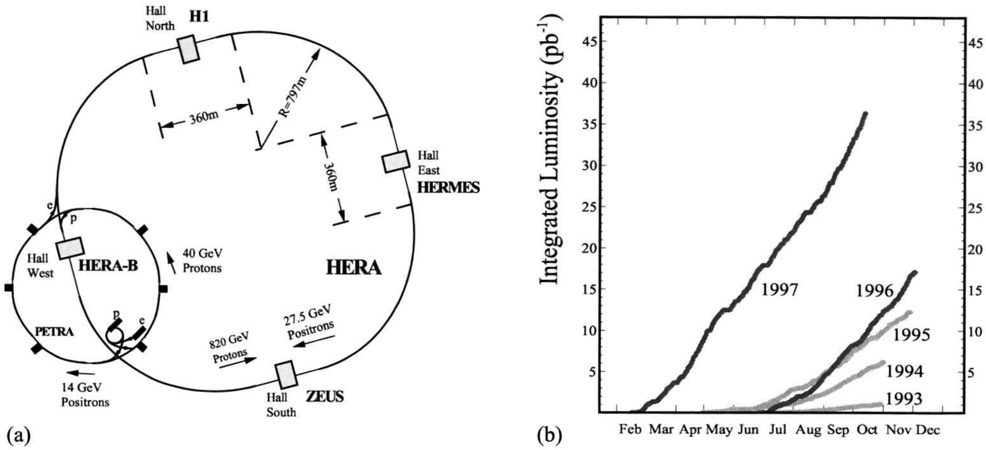

Figure 3.1: *(a) An overview of the HERA machine and its preaccelerator chain. The location of the four experiments is also shown. (b) The collected integrated luminosity of the ZEUS experiment for the period 1993-1997 as function of time. The 1996 run started after a long shutdown in which the experiments improved their detectors.*

The H1 detector [46] is situated in the North Hall and has been designed to study *ep* interactions. It is a general purpose experiment and the most notable component is its calorimeter which consists of a liquid-argon calorimeter [47] and the high-granularity 'Spaghetti Calorimeter', or SPACAL [48] in the rear direction, which allows the very precise measurement of scattered positrons at low scattering angles.

The HERMES experiment [49], found in the East Hall, only uses the positron beam. This experiment measures the spin dependent structure functions of nucleons by looking at deep inelastic scattering of the polarised positron beam on a polarised gaseous jet target that is injected into a storage cell located in the beam vacuum.

In the West Hall the last addition to the HERA experiments is found: HERA-B [50]. Designed as an experiment to measure CP violation in the b-sector in proton-nucleon interactions it only uses the HERA proton beam on a fixed target consisting of wires in the beam halo.

The two general purpose experiments, ZEUS and H1 have been around from the start of HERA operations, whereas the HERMES experiment and HERA-B were commissioned at a later date.

3.2. The ZEUS detector

The ZEUS detector [51] has an almost 4π coverage, except for the beam pipe entrance and exit; here only those subcomponents relevant to the presented analysis will be treated in detail. Figure 3.2 shows a cross section of the ZEUS detector, up to the Backing Calorimeter (BAC) which is the outermost detector shown. The

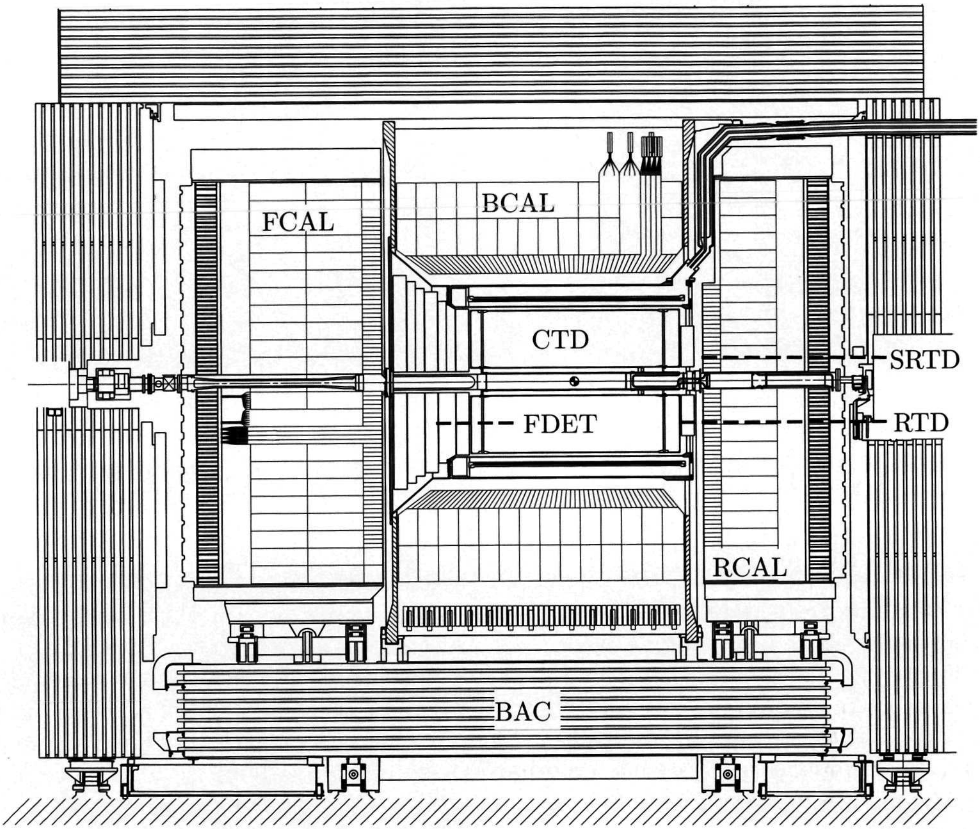

Figure 3.2: *The ZEUS detector. The protons enter the detector on the right hand side, the positrons on the left hand side.*

calorimeter system (Rear, Barrel and Forward Calorimeter) and the tracking system (Central Tracking Detector - CTD, Forward Detector - FDET, Rear Tracking Detector - RTD and Small Angle Rear Tracking Detector - SRTD) are the two most important subcomponents for the measurement of charm production in DIS.

The ZEUS coordinate system is a right-handed Cartesian system, with the Z axis pointing in the proton beam direction, referred to as "forward direction", and the X axis pointing left towards the center of HERA. The coordinate origin is at the nominal interaction point.

3.2.1. The central tracking detector

The Central Tracking Detector of ZEUS, the CTD, is a cylindrical wire chamber that covers 2.05 meters in Z and extends from 16.2 cm to 79.4 cm in r. The drift chamber is organised in 9 *superlayers* (Fig. 3.3), each layer consisting of 8 wires, giving a total of 72 wire-layers. Five of the superlayers, the odd numbered ones, have a zero angle

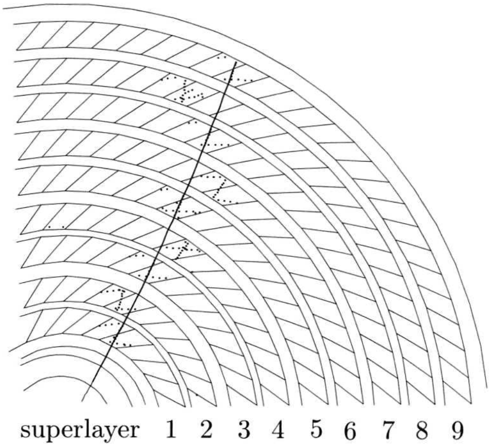

Figure 3.3: *Track hits in the Central Tracking Detector (CTD). The nine superlayers are labelled appropriately.*

with respect to the CTD-axis, whereas the even numbered superlayers all have small stereo angles with respect to this axis. The CTD is surrounded by a thin superconducting solenoid coil that generates a magnetic field of 1.43 T. The CTD covers the polar angle region $15° < \theta < 164°$.

The hits from the CTD are combined to form tracks by a pattern recognition software package in the offline event reconstruction, called VCTRAK, as described in Ref. [52]. These tracks are then used to fit a primary or secondary vertex. Tracks that are associated with a vertex are refitted using that vertex as an additional constraint.

The transverse-momentum resolution for full-length tracks is $\sigma(p_T)/p_T = 0.0058p_T \oplus 0.0065 \oplus 0.0014/p_T$ [53], with p_T in GeV. The resolution is built up from three independent contributions. The first is the error on the measurement on the hit, the second is due to multiple scattering *within* the CTD and the third stems from multiple scattering in (inactive) material *before* a particle reaches the CTD.

Particle identification

Charged particle identification can be achieved by measuring the ionisation energy that is deposited in the CTD per unit path length, or the dE/dx for short. The energy loss by ionisation is given by the Bethe-Bloch formula [54]:

$$\frac{dE}{dx} = -4\pi N_A r_e^2 m_e c^2 z^2 \frac{Z}{A}\frac{1}{\beta^2}\Big(\ln\Big(\frac{2m_e c^2\gamma^2\beta^2}{I}\Big) - \beta^2 - \frac{\delta}{2}\Big) \tag{3.1}$$

which relates the energy loss to the velocity of the particle, its electrical charge and properties of the medium it is traversing. The charge of the particle is given by z, the velocity and Lorentz factor are $\beta = v/c$ and $\gamma = 1/\sqrt{1-\beta^2}$. The medium is summarised by Z, the atomic number and A, the atomic weight. The density effect, δ, accounts for the screening of the particles electrical field in a dense medium and flattens off the relativistic rise of the energy loss. The mean ionisation potential, I, is given approximately by $16Z^{0.9}$ eV for $Z > 1$. N_A denotes Avogadro's Number, m_e the electron mass and r_e the classical electron radius.

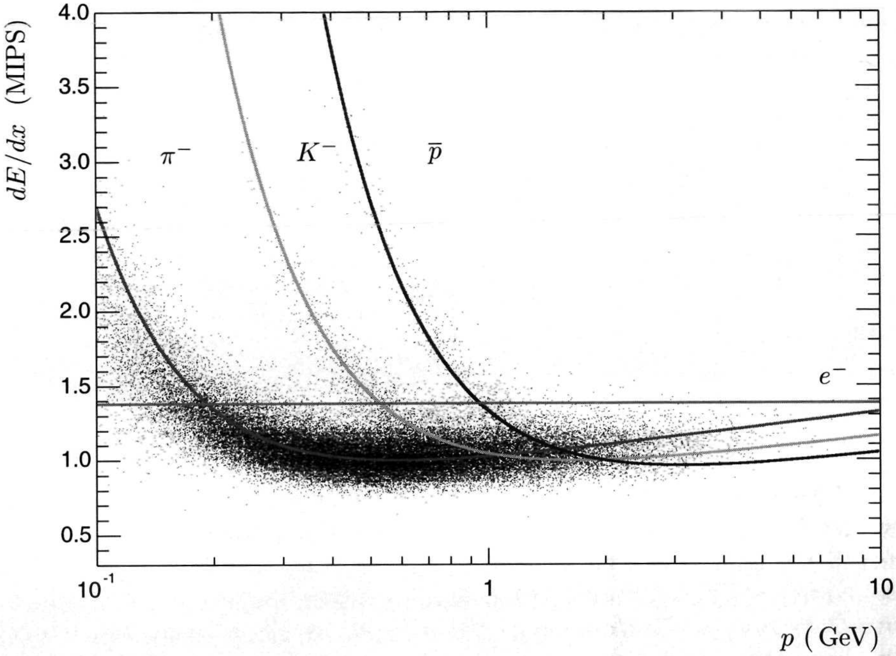

Figure 3.4: *The measured dE/dx versus momentum for a sample of tracks in the CTD. The lines show the Bethe-Bloch prediction for different particles. In certain momentum ranges a perfect particle identification can be achieved for the hadrons.*

With the dependence of dE/dx on v the mass of the particle can be measured through the relation between the velocity and the momentum of relativistic particles. Figure 3.4 shows the actual reconstructed dE/dx as function of track momentum. Clear bands are seen corresponding to pions, kaons, protons and electrons traversing the detector.

dE/dx in the CTD

The calibration of the CTD output to the true energy loss is based on the signal of a pion. The ionisation of these pions is considered as the standard of a minimum ionising particle: MIP. Technically, the peak in the energy loss distribution (Eq. 3.1) is estimated by the truncated mean of the measured energy loss per wire. The use of the truncated mean (lower (upper) 10(30)%) allows to compensate for the very asymmetric shape of the energy loss, which follows a Landau-distribution [32]. If the number of saturated wire responses exceeds the 30% of the truncated mean than all saturated wires are removed from the calculation and the calculation of the truncated mean is adjusted to accommodate this. From a sample of charged pions the scale of the response of a 1 MIP particle can be determined; all dE/dx measurements can subsequently be expressed in this unit. As the CTD is operated at atmospheric

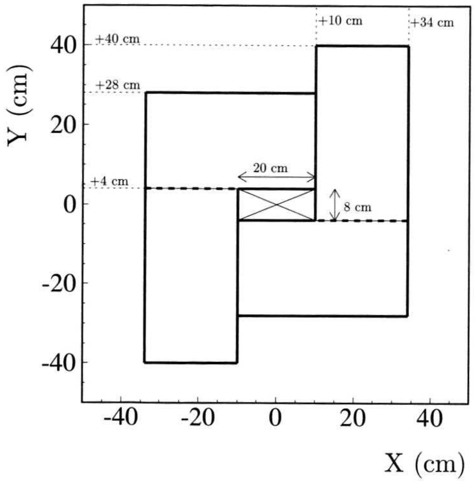

Figure 3.5: *A schematic overview of the geometry of the Small angle Rear Tracking Detector (SRTD). The distances are with respect to the nominal beam line.*

pressure it is necessary for the 1 MIP value to be determined on a run-by-run basis, to correct for atmospheric pressure fluctuations between runs. The typical duration in time of the runs allows pressure fluctuations within one run to be ignored.

When tracks are considered that pass through (at least) 7 superlayers, which is necessary for a good measurement of dE/dx, a polar angle range of $37° < \theta < 143°$ ($= 0.65 < \theta < 2.5$ rad) is available. In this case dE/dx is measured with a resolution of about 9%. The resolution is measured by fitting a Gaussian to the dE/dx distribution of a sample of conversions. These conversions have been selected using very strict criteria on the reconstructed invariant mass of and the opening angle between an electron and positron pair.

3.2.2. The small angle rear tracking detector

The small angle rear tracking detector (SRTD) is a scintillating strip detector that consists of two planes of strips with horizontal (vertical) orientation [55]. It is located between the RTD and RCAL. The SRTD has been designed to improve the precision of reconstruction of the (angle of the) scattered positron and correct the measurement of the electron energy.

Figure 3.5 shows the layout of the SRTD on the RCAL surface. Each plane is divided in four quadrants, 24×44 cm^2 each. The original layout was such that the four quadrants had a perfect square outline, but due to the decision to move the central calorimeter modules closer to the beam this was changed to the shape presented in Fig. 3.5. The hole of 20×8 cm^2 in the centre accommodates the beam-pipe.

The SRTD yields a position measurement with an accuracy of 3 mm in both X and Y and the measured pulse height information is used to correct the RCAL energy measurement of the scattered positron. Finally, the SRTD gives timing information for minimum ionising particles, with a resolution better than 2 ns. This information is used at the first level trigger stage to reject beam-gas events from upstream of the

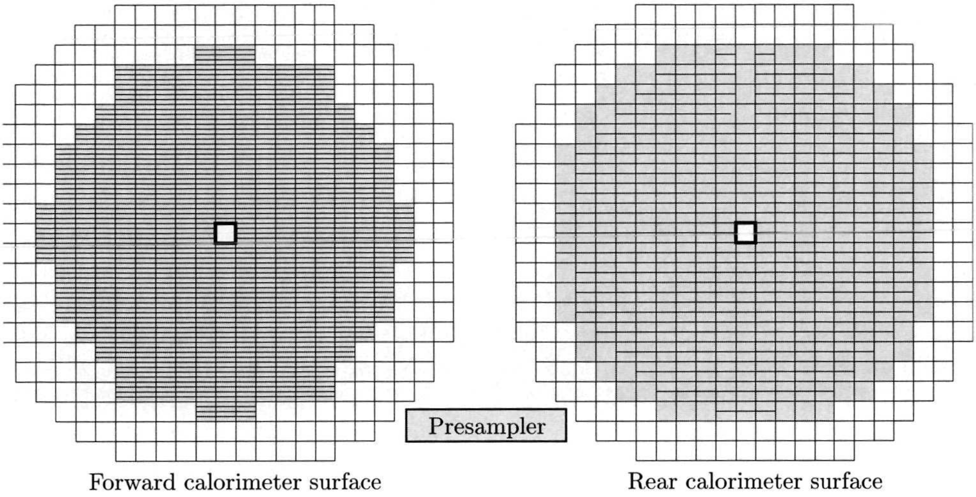

Figure 3.6: *The coverage of the presampler on the calorimeter surface for both the forward (left) and rear (right) calorimeter surfaces is shown by the shaded colour. The calorimeters cell granularity is also shown. The forward region has twice the granularity in the electromagnetic calorimeter (EMC) modules compared to the rear direction. The modules that are shadowed by the barrel instrumentarium only have a single EMC cell.*

detector.

3.2.3. The presampler system

The presampler system (PRES) was installed on the rear and forward calorimeter surface during the 1995 shutdown. It identifies early showering particles and will improve the energy measurement of the calorimeter by taking into account energy loss information in the reconstruction. The presampler consists of 576 20×20 cm^2 scintillator tiles with a thickness of 0.5 cm, see Fig. 3.6.

The rear presampler (RPRES) system is used in the reconstruction of the energy of the scattered positron.

3.2.4. The uranium calorimeter

Surrounding the tracking system is the ZEUS uranium-scintillator sampling calorimeter [56] (CAL), as shown in Fig. 3.2. The calorimeter consists of three independent detectors: the rear (RCAL), barrel (BCAL) and forward (FCAL) calorimeters. The three detectors cover almost completely the solid 4π angle, with adequate overlap between RCAL-BCAL and BCAL-FCAL.

The calorimeters are divided in towers. Each tower is segmented into two hadronic sections (HAC) (only one for RCAL) and one electromagnetic section (EMC). The BCAL EMC towers are projective in both θ and ϕ. The HAC towers have a surface of 20 × 20 cm^2 and the two individual sections are called cells. The EMC section consists of four 5 × 20 cm^2 cells in the FCAL and two 10 × 20 cm^2 cells in the barrel and rear calorimeters. The layout of the EMC cells of both FCAL and RCAL are shown in Fig. 3.6. The thickness of the calorimeter varies between 7 interaction lengths λ for the F- and BCAL (1λ for the EMC and 3λ per HAC section) and 4λ in the RCAL ($1(3)\lambda$ for the EMC(HAC) section).

Each cell consists of alternating slabs of 3.3 mm depleted uranium and 2.6 mm scintillator material. One interaction length (1λ) consists of 25 slabs of depleted uranium and scintillator material. The light from scintillator tiles is transported by wave length shifters that are mounted on two sides of the tiles. These wave length shifters are read out with photomultiplier tubes. By applying readout on two sides a redundancy is introduced that, to a large extent, prevents dead spots, or holes, in the calorimeter readout. An additional feature is that for isolated particles position reconstruction can be done with the measured energy asymmetry in the cell. This is used to reconstruct the position of the scattered positron in the absence of the SRTD.

The calorimeter is calibrated using the natural radioactivity of the depleted uranium. It allows the monitoring and calibration of the scintillator light yield and the gain of the photomultiplier tubes, at the level of 1% [51].

The thickness of both the depleted uranium and the scintillator material has been tuned such that the measured response for hadronic (h) and electromagnetic showers (e) is equal for particles of equal energy, throughout the whole calorimeter. In the case that e/h is not equal to one, a deterioration of the energy resolution arises because of the creation of π^0 in the first hadronic interaction. Neutral pions give a electromagnetic component within hadronic showers, as they decay into two photons. As π^0-production in hadronic interactions follows a non-Gaussian distribution [57], the pure $\sqrt{E}$ scaling of the energy resolution gets violated. The compensating design therefore optimises the energy resolution for hadrons. This is reflected in the energy resolution of the calorimeter which is an excellent $\sigma(E)/E = 0.35/\sqrt{E}$ for hadrons and $\sigma(E)/E = 0.18/\sqrt{E}$ for electrons (E in GeV).

Because of the importance of the calorimeter response to electrons and hadrons for the analysis presented in chapter 5, a digression is made here to give a more detailed treatment of the development of showers for electrons and hadrons.

An electromagnetic shower

For electrons, with $E > 9$ MeV moving through uranium, the primary source of energy loss is the *bremsstrahlung* process. The incident electron radiates a photon under the influence of the electromagnetic field of the atomic nuclei in the absorber material. The energy spectrum of the radiated photons falls as $1/E$, where E is the energy of the photon. The photon is radiated more or less collinear to the trajectory of the electron, which in its turn deviates a little from its original path. The electron will continue to do this until it reaches the *critical energy*. At that point the energy loss of the electron will be mainly driven by the ionisation and excitation of the absorber atoms.

As long as the *bremsstrahlung* photons have an energy that is larger then twice the electron mass they will produce electron-positron pairs. These leptons will undergo

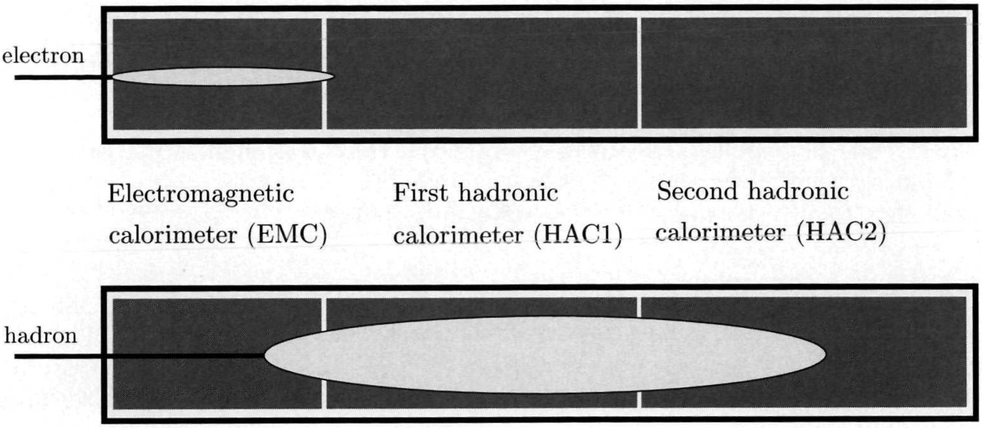

Figure 3.7: *Energy deposition profile for electrons and hadrons in the ZEUS calorimeter (oval shaped forms). Electrons deposite the larger part of their energy in the EMC section. Hadrons on the other hand have a slower shower development which is also less spread out in the direction perpendicular to the incident particle's direction of movement.*

the same energy deposition trajectory as the initial electron, until the electron is absorbed by an ion and the positron annihilates with an atomic electron.

If the photon energy is below the pair-production threshold it will dissipate its energy by incoherent (*Compton*) scattering on the atomic electrons. At even lower energies the photon can be absorbed by an atom.

The shower starts to develop as soon as the electron enters the material. The longitudinal length of an electron shower is logarithmically proportional to its energy. In the first stage of shower development, before the maximum number of particles is reached, the transverse spreading of the shower is dominated by the multiple scattering of the electrons and positrons due to the repetitive radiation of *bremsstrahlung*-photons. After this initial stage, the main processes involved in the energy deposition are *Compton* scattering and the photo-electric effect. These processes have a more isotropic nature, thus contributing extensively to the broadening of the shower profile.

A hadronic shower

The development of a hadronic shower follows a different mechanism than in the electromagnetic case. Unlike in the electromagnetic case the hadrons do not start to radiate photons in *bremsstrahlung* interactions. This is due to the large difference in mass between hadrons and electrons/positrons: $m_\pi/m_e \approx 300$. The *bremsstrahlung* cross section is proportional to the inverse of the mass of the parent particle squared. Instead, the shower develops through hadron-nucleus scattering, producing secondary hadrons in the process. The produced secondary hadrons typically have a transverse momentum with the shower axis of about 350 MeV. As a result a typical hadronic shower is much broader than the electromagnetic shower of an electron with the same initial energy. If the secondary hadron is a π^0 then an electromagnetic component develops in the shower due to the decay of the pion into two photons.

The cross section for hadron-nucleus scattering is in the order of 100 mb for a 1 GeV hadron [36]. Compared to the *bremsstrahlung* cross section of 1 GeV electrons, which is of the order of 400 barns this is relatively low. A direct result of this difference is that an electron starts to produce a shower as soon as it reaches the calorimeter while (on average) a hadron will be able to pass through a significant amount of calorimeter material before developing a shower.

A qualitative comparison

The differences in the average shower development behaviour of an electromagnetic and hadronic shower have been summarised in Fig. 3.7: an electron (or positron) produces a relatively narrow shower, starting as soon as it hits the calorimeter whereas the hadron only starts to shower after it has traversed a good part of the EMC section. Also, the shower produced by the hadron tends to be much wider and extends to a larger depth in the calorimeter. Electrons can be differentiated from hadrons with the measurement of the longitudinal depth of the shower in terms of the energy profile in the three (two) section of a calorimeter tower.

3.2.5. Luminosity measurement

The delivered luminosity at ZEUS is determined by measuring the *bremsstrahlung* process $ep \rightarrow ep\gamma$. The cross section of the Bethe-Heitler process has been calculated to high accuracy [58]. This process is measured using a lead-scintillator calorimeter that is placed at Z =-107 m from the interaction point. It accepts photons at angles ≤ 0.5 mrad with the electron beam. The data equivalent luminosity is measured with this detector with an $\approx 3\%$ uncertainty [59].

CHAPTER 4

Event reconstruction and selection

The focus of this chapter will be on the methods and strategies used to select neutral current DIS events. First an introduction will be given on the reconstruction of the kinematic variables of the events. This will be followed by a discussion of the event selection criteria. This chapter ends with a comparison between the selected data and the Monte Carlo simulation results.

4.1. Event reconstruction

The final state of a DIS event contains two distinct objects: the scattered positron and the hadronic system (Fig. 4.1). The hadronic system combines everything that is not attributed to the scattered positron in one single object. There are methods available that relate the scattered positron (E'_e, θ_e), the hadronic system $(\delta_h, P_{\mathrm{T},h})$ or a combination of the two to the kinematic variables that characterise the hard process that lay at the basis of a DIS-event. The hadronic system can be further broken down into the current jet, which is the result of hadronisation of the struck quark, and the proton remnant.

4.1.1. The scattered positron

Identification

The scattered positron which interacted through a photon with a quark in the proton, is experimentally described by its final state energy and the polar scattering angle. The key detector signature of the scattered positron is an isolated electromagnetic energy deposit in the calorimeter ($E \gg 5$ GeV).

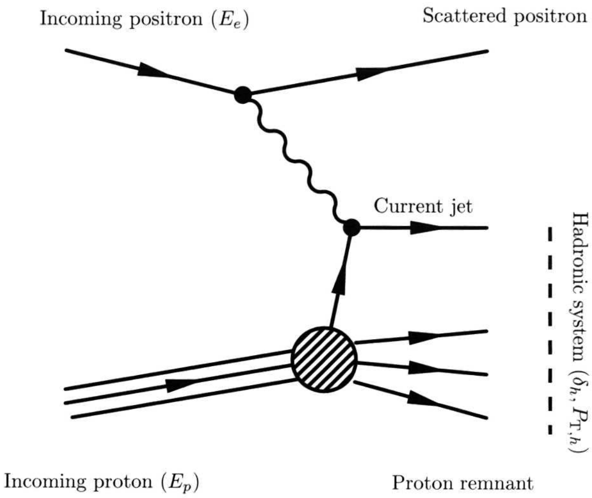

Figure 4.1: *A schematic view of a DIS-Event. The initial state is, apart from initial state radiation, completely determined by the HERA-beam parameters.*

Reconstruction

The standard ZEUS reconstruction software includes a feed-forward neural network [60] called SINISTRA. This neural network is fed 54 energy measurements from a cluster of 3×3 calorimeter towers with 2 EMC and 1 HAC sections, separated in the individual left and right photomultiplier signals. As the shape of the energy profile is also dependent on the angle of incidence with the calorimeter surface, the cosine of the angle of incidence is given to the network as well. This makes a total number of 55 input variables. The output of the network is a single variable that can be interpreted as the probability that the given input was caused by a positron. The positron candidate with the highest probability is assumed to be the scattered DIS-positron.

The final state energy E'_e is reconstructed using the calorimeter. To improve the energy resolution ZEUS utilises the pre-shower measurement of either the presampler system or the SRTD. The energy corrections have been obtained by the ZEUS-inclusive F_2 working group after an extensive analysis of the detector responses [61].

The scattering angle θ_e is determined by combining the position measurement at the calorimeter surface with the vertex that is obtained from the track/vertex reconstruction. When the positron enters within the fiducial surface, at least 0.5 cm from the borders of the SRTD, it is used to determine the impact point. In all other cases the calorimeter is used to determine the entry point.

4.1.2. The hadronic system

The hadronic final state can be divided in several *jets* where one jet, typically the most energetic, can be directly associated with the struck quark of the hard interaction. Any other jet is produced by gluons that are radiated by the struck quark. The

Figure 4.2: *An example of the cell-island clustering algorithm. The squares are calorimeter cells. The filled squares are cells that have energy deposited in them. Island 1 shows a normal case of the clustering algorithm. The islands 2 and 3 show an example of two cells that touch each other only at the corner.*

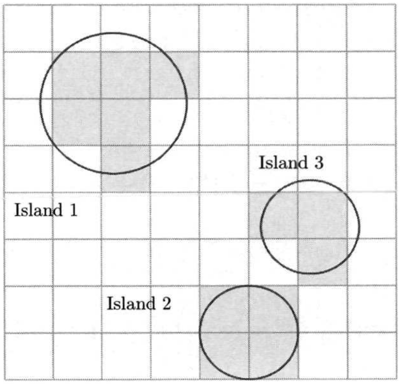

analysis of jets is a topic on its own, and for the analysis of the semileptonic decay of charmed hadrons it is of no principle interest. Here it suffices to look at the hadronic final state in a very course manner, namely by looking at the energy deposited in the calorimeter that has not been attributed to the scattered positron. The hadronic final state is defined in terms of detector observables: δ_h, the hadronic $E - p_Z$ and and the transverse momentum of the hadronic system, $p_{\mathrm{T},h}$, which are defined as

$$\delta_h = \sum_{i=1}^{N}(E_i - p_{Z,i}) \tag{4.1}$$

$$p^2_{\mathrm{T},h} = (\sum_{i=1}^{N} p_{X,i})^2 + (\sum_{i=1}^{N} p_{Y,i})^2 \tag{4.2}$$

where the sums run over all the calorimeter clusters that are not associated with the scattered positron. These two observables can be combined to give another variable, γ_h:

$$\cos\gamma_h = \frac{p^2_{\mathrm{T},h} - \delta^2_h}{p^2_{\mathrm{T},h} + \delta^2_h} \tag{4.3}$$

which is, at leading order, the polar angle of the struck quark.

These three variables are reconstructed by combining calorimeter cells to form cell-islands. A cell-island is a cluster of neighbouring calorimeter cells with a signal as shown in Fig. 4.2. This is done for the EMC, HAC1 and HAC2 sections separately. The cell-islands of the different layers are then combined into cone-islands, again with a nearest neighbour algorithm. The position of the cone-island is determined by the center-of-gravity of the energy deposits.

The next step is to combine the cone-islands with tracking information. Only tracks that are fitted to a vertex and have a reasonable transverse momentum, 0.1 $< p_T <$ 20 GeV, are considered. The distance between the track projection on the calorimeter surface and the cone-island is used to determine if a track is matched to a cone-island. This results in a list of cone-islands, unmatched tracks and tracks with a matched cone-island. These three objects are all called ZUFOs [62], where ZUFO stands for Zeus Unidentified Flow Object.

The last step in the reconstruction of the hadronic system is the *backsplash* correction. The term backsplash is used for a range of effects that cause isolated energy deposits away from the 'true' hadronic system [63], which includes

- Calorimeter backsplash - an effect occuring when a highly energetic particle hits the calorimeter surface. Occasionally this will yield low energy neutral particles that scatter back from the calorimeter (albedo effect). These particles can pass through the tracking detector and deposit their energy in another part of the calorimeter.

- Pre-calorimeter showering - particles always pass some material before they reach the calorimeter. Once in a while this will trigger the development of a shower before the calorimeter.

- Noisy calorimeter cells - noisy cells that are not already identified as such can give a signal coinciding with actual events in the detector.

In general any of these effects is characterised by the fact that it involves low-energy deposits in the calorimeter without a matched track and relatively far (in terms of polar angle) from the hadronic system. Backsplash is removed by rejecting those low-energy clusters ($E < 3\,\mathrm{GeV}$) that have a large pull on the γ_h of the event and do not have a vertex fitted track associated to them. An exception is made if the cluster has an energy of more than 1.5 GeV and has a timing that is correct for coming from the primary vertex, in which case the cluster is not removed.

After the clustering, matching and the backsplash correction there is a list with ZUFOs that all have an energy and momentum assigned to them. The ZUFOs are then combined to give the δ_h, $p^2_{\mathrm{T},h}$ and γ_h of the event.

4.1.3. Kinematic estimators

All the information of the hard scatter is contained in a combination of any two of the variables Q^2, x and y, which are related through $Q^2 = sxy$, where s is the centre of mass energy squared. To relate the measured final state objects, the scattered positron and the hadronic system, to the hard scatter information several methods are available. In figure 4.3 the isolines for the used four observables of the final state are shown.

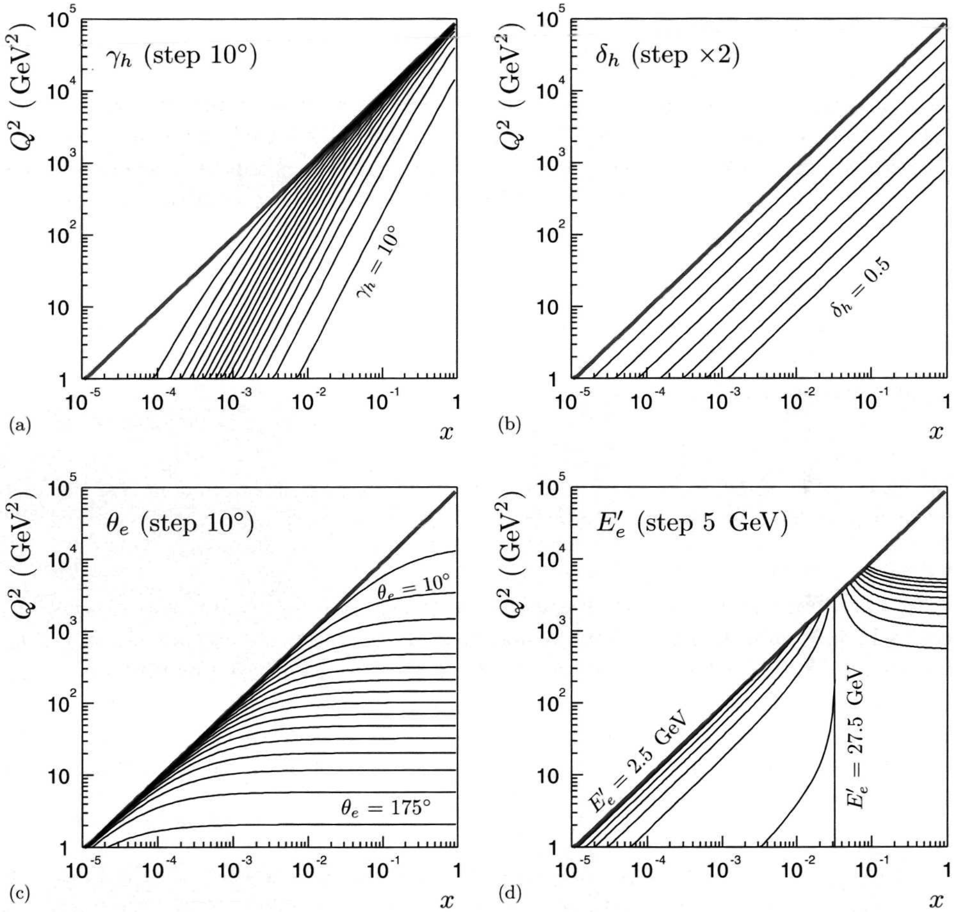

Figure 4.3: *The isolines in the $Q^2 - x$ plane of (a) the hadronic angle, (b) the hadronic δ, (c) polar angle of the scattered positron and (d) the energy of the scattered positron. The diagonal line (from left-bottom to right-top) gives the kinematic limit for the ZEUS experiment, where $y = 1$.*

Jacquet-Blondel method

The Jacquet-Blondel method uses only the hadronic system to reconstruct the kinematics of the event. The following set of equations is used:

$$y_{JB} = \frac{\delta_h}{2E_{e,\mathrm{beam}}} \tag{4.4}$$

$$Q^2_{JB} = \frac{p^2_{T,h}}{1-y_{JB}} \tag{4.5}$$

where $E_{e,\mathrm{beam}}$ is the energy of the incoming positron beam. The use of this reconstruction method is very limited in the case of NC-DIS. A large fraction of the hadronic system, the proton remnant, will escape detection as it goes down the beamline, in the beam-pipe, distorting the $p^2_{T,h}$-measurement. This unavoidably makes that, especially for low Q^2, moderate x the resolution of this method is poor. A second problem is the fact that in the determination of y_{JB} the nominal positron beam energy is used. In the case of initial state (QED) radiation (ISR) events this underestimates the y of the event. For charged current interactions on the other hand, it is the only available method, as in that case the neutrino escapes undetected and thus removes the information of the leptonic part of the interaction.

Electron method

Where the Jacquet-Blondel method uses solely the hadronic system, this method relies on the measurement of the scattered positron. The kinematic variables are reconstructed with the following equations:

$$y_e = 1 - \frac{E'_e}{2E_{e,\mathrm{beam}}}(1-\cos\theta_e) \tag{4.6}$$

$$Q^2_e = 2E'_e E_{e,\mathrm{beam}}(1+\cos\theta_e) \tag{4.7}$$

Both the y_e and Q^2_e are directly dependent on the energy of the scattered positron, E'_e. This variable does not have very good discriminative power in the region of moderate x ($x = 10^{-4} - 10^{-2}$), as can be seen from Fig. 4.3(d). This is however the region that is of most interest for this analysis. This therefore disqualifies the electron reconstruction method as the algorithm of the kinematic reconstruction.

Double angle method

The double angle method is a reconstruction method that is based on the angles of both the hadronic system and the scattered positron [64]

$$y_{DA} = \frac{\sin\theta_e(1-\cos\gamma_h)}{\sin\gamma_h + \sin\theta_e - \sin(\gamma_h-\theta_e)} \tag{4.8}$$

$$Q^2_{DA} = 4E^2_{e,\mathrm{beam}}\frac{\sin\gamma_h(1+\cos\theta_e)}{\sin\gamma_h + \sin\theta_e - \sin(\gamma_h-\theta_e)} \tag{4.9}$$

The principle strength of this method is that there is no dependence on the measurement of any of the energies. The two observables, θ_e and γ_h, used in this method both have good discriminative power in the region of interest, which combined will allow for a good reconstruction of the kinematic variables.

Sigma method

The sigma method attempts to tackle two of the problems of the Jacquet-Blondel reconstruction method. To accommodate the effect of ISR the $\delta_{\text{tot}} = E - p_Z$ of the event is used instead of the positron beam energy. The second improvement can be found in the replacement of the hadronic p_{T} with the p_{T} of the scattered positron. With these enhancements the equations become

$$y_\Sigma = \frac{\delta_h}{\delta_{\text{tot}}} \tag{4.10}$$

$$Q^2_\Sigma = \frac{p^2_{\text{T},e}}{1 - y_\Sigma} \tag{4.11}$$

The resolution of the Σ-method is better than that of the double-angle in the low Q^2 region ($Q^2 \lesssim 40\,\text{GeV}^2$). At intermediate and high Q^2 the two are comparable.

For this analysis

The present analysis uses several of the presented reconstruction methods. The Jacquet-Blondel and electron methods are used to reject certain specific regions of phase space (Sec. 4.3). Because of the better resolution in the low-Q^2 region the Σ-method is preferred above the double angle algorithm. As a consequence, the kinematic variables for the single and double differential cross sections are reconstructed using this method.

4.2. Event pre-selection with the trigger

The ZEUS data acquisition system uses a three level trigger system. After each step the data volume is reduced and more time is available, allowing for the reconstruction of more (complicated) information on which to base trigger decisions.

4.2.1. The first level trigger

At the FLT level all components store their data in a 52 step deep pipeline buffer. The data is moved down the pipeline following the HERA clock-cycle of 96 ns, which is equal to the bunch crossing interval. During these 52×96 ns=4.68 μs component trigger logic must reach a decision and allow the Global First Level Trigger (GFLT) to combine all such input into a global trigger flag. This leaves a maximum time of 2 μs for the local FLT-systems to process information and another 2 μs for the GFLT. The extra time is needed to ensure proper read out of all the components on an ACCEPT signal. The most important systems at this level are the CAL [65] and the CTD [66]. The SRTD-FLT is used to veto events that have a signal in the SRTD but did not coincide with the beam-crossing time.

At the FLT-stage a neutral current DIS event is identified by tagging the scattered positron. For the analysis presented here, there are four trigger slots at the FLT that were used to select the events. Three of these slots are designed to select events where the scattered positron enters the rear calorimeter. The first trigger requires an isolated cluster with the larger part of the energy in the electromagnetic calorimeter (ISOe). This condition is defined as

$$\mathrm{ISOe} = (\mathrm{E}_{HAC} < 0.95 \text{ GeVor } \mathrm{E}_{HAC}/\mathrm{E}_{TOT} < 1/3) \text{ and } \mathrm{E}_{EMC} > 2.08 \text{ GeV}$$

where the energies are the respective sums of hadronic (HAC), electromagnetic (EMC) and combined parts of the associated isolated cluster. In total there are three trigger slots defined to identify electrons in the RCAL:

FLT1 - ISOe and $\mathrm{E}_{CAL} > 0.46$ GeV and a signal in the SRTD,

FLT2 - *threshold* $\mathrm{E}_{EMC}^{RCAL} > 3.75$ GeV,

FLT3 - *nominal* $\mathrm{E}_{EMC}^{RCAL} > 3.4$ GeV,

where the labels *threshold* and *nominal* denote different calorimeter energy sum strategies. In the case of the *nominal* energy sum all the towers with $\mathrm{E} < 464$ MeV are set to zero, as well as the inner ring of the towers in the RCAL. The *threshold* energy sum excludes no towers and is the total sum of measured energy. These combinations of trigger logic select events with positrons in the RCAL with an efficiency of well over 99% for $E'_e > 7$ GeV.

The events where the scattered positron ends up in the barrel calorimeter are selected by

FLT4 - *threshold* $\mathrm{E}_{EMC}^{BCAL} > 4.78$ GeV and a track in the CTD FLT

These four trigger definitions were combined to form two trigger selection bits:

- GFLT46 = FLT1 or FLT2
- GFLT44 = FLT3 or FLT4

The rates for data and Monte Carlo for these trigger bits are shown in Fig. 4.4(a).

4.2.2. The second level trigger

The second level trigger is built up of per-component transputer based sub-triggers and a Global Second Level Trigger (GSLT) network. The GSLT decides on the event-ACCEPT based on the information passed by the trigger components, like the GFLT. The most important information for the GSLT is found in global energy sums (E_T, $\delta = E - p_Z$), primary vertex information and timing of the event. The output rate of the SLT is capped at 60 Hz.

To select the data sample for this analysis no explicit cuts on SLT-bits were made.

Table 4.1: *The data sample split into the years of running and trigger configuration. All luminosities are given in* pb^{-1}.

Year	$\mathcal{L}_{\mathrm{DIS01}}$	$\mathcal{L}_{\mathrm{DIS03a}}$	$\mathcal{L}_{\mathrm{DIS03b/d}}$	$\mathcal{L}_{\mathrm{TOT}}$
1996	5.7	2.4	-	8.1
1997	-	0.6	24.7	24.7
combined	5.7	3.0	24.7	32.8

4.2.3. The third level trigger

At this stage the event is completely reconstructed. The reconstructed primary vertex allows δ to be determined with better precision, so the event selection can be more stringent than at previous trigger levels. The TLT runs four different electron finder algorithms, among which is the SINISTRA programme. Events are selected as a DIS-type event if any of them returns a suitable candidate. Events are selected if they satisfy all of the following criteria:

- $E'_e > 4$ GeV for any one of the electron finders best candidates
- $\delta + 2E_{Lumi\gamma} > 30$ GeV
  where $E_{Lumi\gamma}$ is the measured energy in the photon calorimeter of the luminosity monitor.
- Scattered positron position.
  During the 1996-1997 run period the trigger has been operated with various selection criteria:
  - DIS01 :$|X| > 12$ cm **or** $|Y| > 6$ cm
  - DIS03a : $|X| > 14.5$ cm **or** $|Y| > 14.5$ cm
    DIS03b/d : $\sqrt{X^2 + Y^2} > 25$ cm

The DIS01 and DIS03 trigger bits are called the low- and medium-Q^2 trigger, respectively. The rate for the DIS01 trigger was too high during high luminosity operation and therefore this trigger was disabled for the larger part of the 1996-1997 running period. The period that it was active has proven to be long enough to do a reasonable measurement in the low-Q^2 region. The difference between DIS03b and DIS03d is purely in the definitions of the used electron finders.

The exact definition of the electron finder algorithms changed four times during the 1996-1997 running period. As the Monte Carlo simulation only incorporates one set of these definitions, a separate simulation package was developed to allow a proper treatment of data and Monte Carlo for the whole running period [67].

The contribution of the different years and triggers to this luminosity is given in Tab. 4.1.

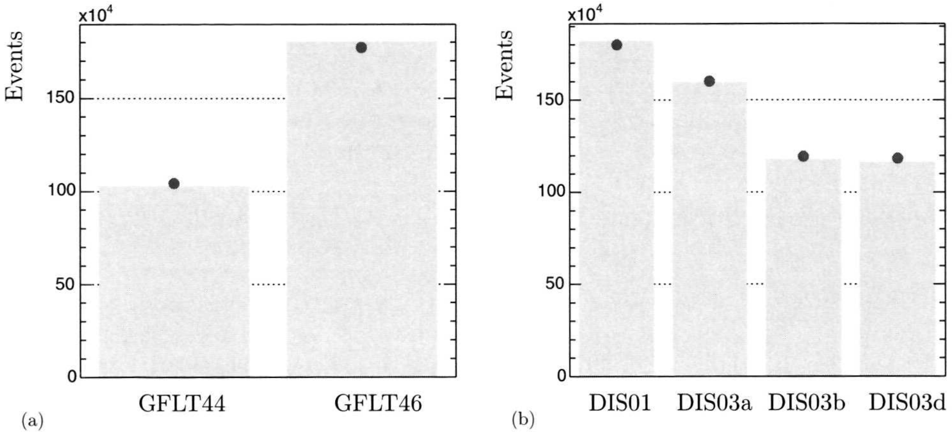

Figure 4.4: *Accepted events for the FLT and TLT trigger bits used in the analysis. The points are accepted events from data. The bars give the (luminosity) corrected numbers from the* DJANGOH *MC-sample.*

4.3. DIS Selection criteria

In the offline stage the final event selection criteria are applied. These selection cuts are based on the selection of a neutral current DIS sample in favour of backgrounds from other production processes, which for DIS analyses is exclusively photoproduction (PHP). The ratio of signal to background events is optimised by the kinematic cuts (δ,Q^2,y) and further tightening of the selection criteria of the scattered positron candidate. On the event sample that passed the TLT requirements the following, additional, criteria were applied to select the set of events that will be further used for analysis:

- $38 < \delta < 65$ GeV

  For a perfectly contained and measured DIS event the δ should be 55 GeV ($= 2E_{e,beam}$), which follows from energy and momentum conservation. Particles that escape down the forward beam-pipe have almost identical energy and longitudinal momentum, which nullifies their contribution to the overall δ. In photoproduction events the 'scattered' positron escapes down the rear beam-pipe. This effectively lowers the measured δ for these type of events, as the E'_e and p_Z do not cancel.

- $|Z_{vertex}| < 50$ cm

  The Z of the vertex is restricted to this range to ensure an excellent understanding of the acceptances of both the calorimeter and the central tracking detector.

- $y_{EL} < 0.95$

Sometimes SINISTRA identifies an electromagnetic cluster in the FCAL as the most probable candidate for the scattered positron. Usually this is due to a π^0, while the *real* scattered positron can be found elsewhere in the detector. As these fake 'positrons' are produced in a decay, they have an energy that is much lower than expected for a high Q^2 event. From Eq. 4.6 it then follows that y_{EL} will be very high for such misidentified positrons. Rejecting those events that have a y_{EL} larger then 0.95 removes those events from the final sample.

- Combined positron energy and probability cut
  The scattered DIS positron is selected by a combination of energy and SINISTRA probability requirements. A previous analysis [61] showed that the rejection of photoproduction backgrounds could be improved if an energy-dependent probability cut is applied. Therefore the following set of criteria is applied:
  - $10 > E'_e$ GeV: all rejected
  - $10 < E'_e < 20$ GeV: probability $> 0.94 + 0.0025E'_e$
  - $20 < E'_e < 30$ GeV: probability $> 1.17 - 0.0090E'_e$
  - $E'_e > 30$ GeV: probability > 0.9
- Scattered positron position projection on RCAL surface (if on RCAL surface, Fig. 4.5)
  - DIS01 : $|X| > 13$ cm or $|Y| > 7$ cm + excluding 'ears' (see Fig. 4.5)
  - DIS03a : $|X| > 14.5$ cm or $|Y| > 14.5$ cm
    DIS03b/d : $\sqrt{X^2+Y^2} > 25.5$ cm
- $y_{JB} > 0.02$
  This cut removes the part of the phase space that is characterised by low total hadronic energy in the calorimeter. This particular part is hard to properly reconstruct and is therefore rejected.

Finally, events are required to lie in the kinematic domain of interest, defined by:

- $2.0 < Q^2_{DA} < 1000$ GeV^2,
- $0.03 < y_{DA} < 0.70$.

4.4. Event sample

With this set of criteria a data sample of slightly over $2 \cdot 10^6$ NC-DIS events has been selected. In figure 4.6(a-e) distributions of the reconstructed final state objects are shown. The data (points) are compared to the DJANGOH Monte Carlo sample (histogram), after event selection. The positron final state (E',θ_e) shows agreement (Fig. 4.6(a,b)). The different cuts on the scattered positron position are immediately visible in the distance between the positron impact point on the RCAL surface and the nominal beamline (Fig. 4.6(c)). The Monte Carlo has a slightly higher tail in

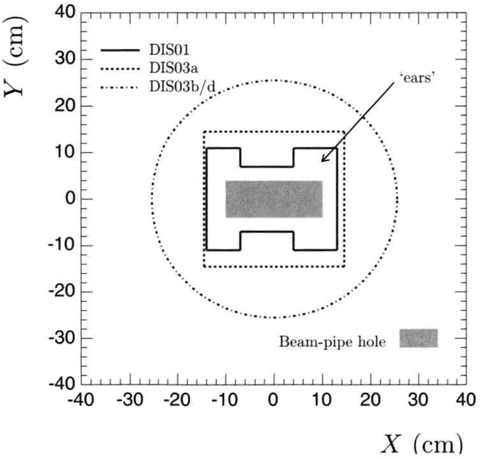

Figure 4.5: *Overview of the three sets of position cuts that are used to select the scattered positron*

the $p^2_{\mathrm{T},h}$ distribution (Fig. 4.6(e)). The γ_h distribution is however well described by the Monte Carlo (Fig. 4.6(d)). The reconstructed δ combines both the positron and the hadronic final state in the detector and is shown in Fig. 4.6(e). Figures 4.6(g-i) show the results of the track/vertex reconstruction. For these selected events the reconstructed double angle variables are compared in Fig. 4.7. Overall, data and Monte Carlo agree.

This event sample will be the starting point for the quest for the electrons from the semileptonic decay of charmed mesons. The event samples contain roughly 15 million tracks, which will serve as the haystack in which the electron-needles need to be found.

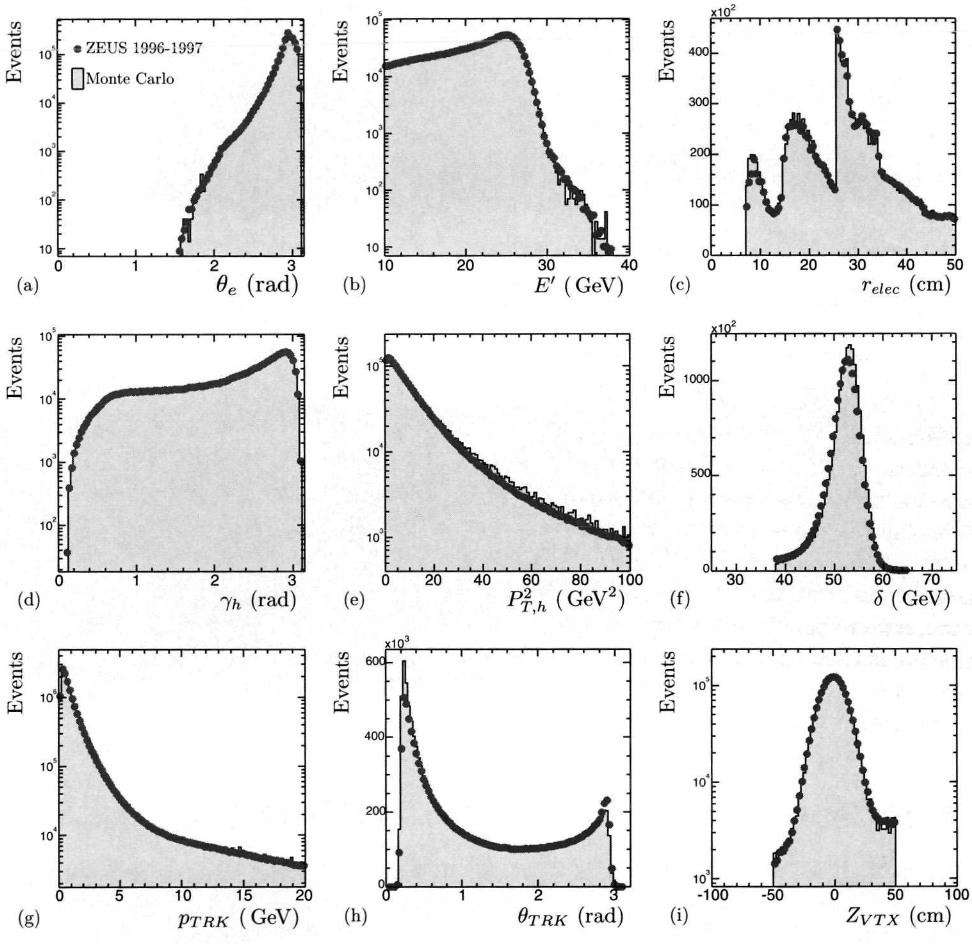

Figure 4.6: *Comparison between data (points) and Monte Carlo (histogram) for some selected properties of the positron (a-c), the hadronic final state (e-f) and the track reconstruction (g-i).*

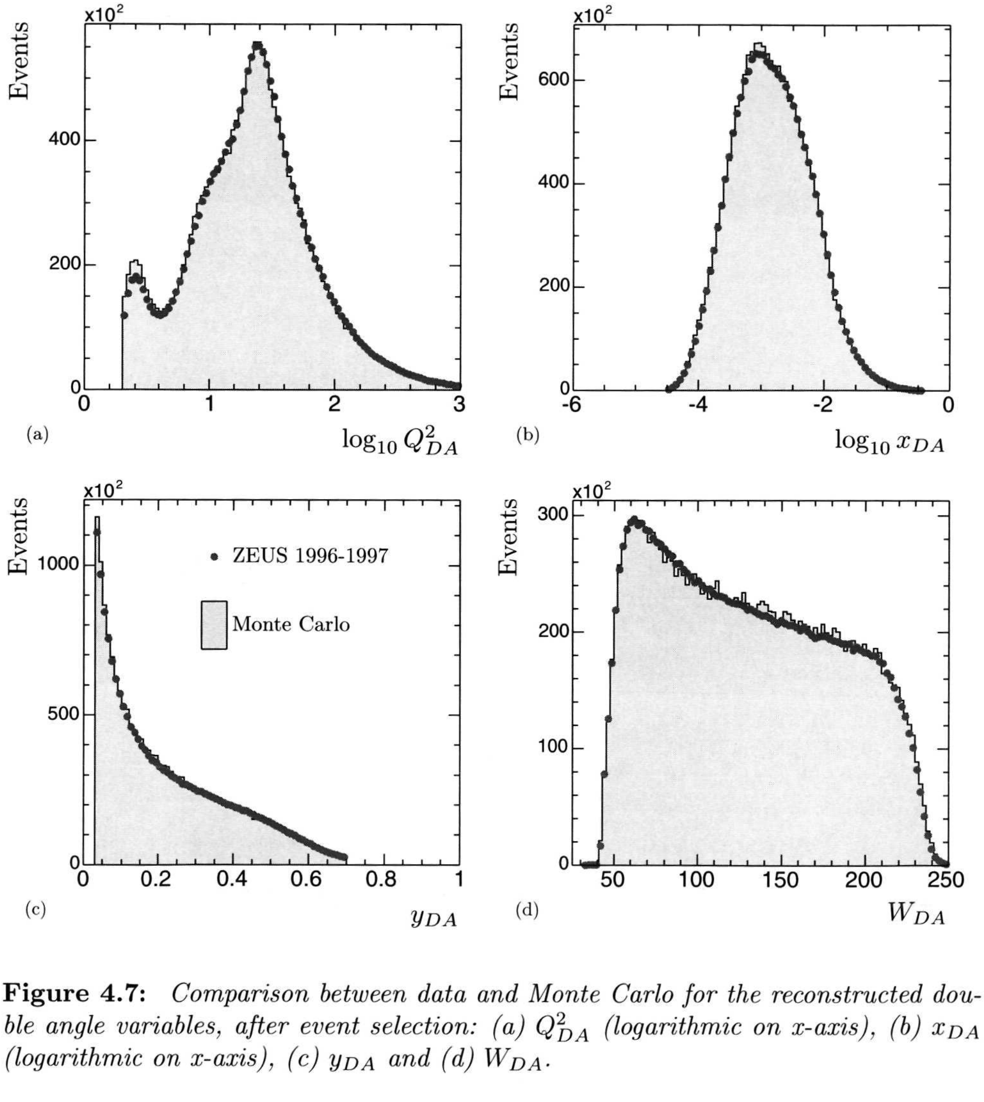

Figure 4.7: *Comparison between data and Monte Carlo for the reconstructed double angle variables, after event selection: (a) Q^2_{DA} (logarithmic on x-axis), (b) x_{DA} (logarithmic on x-axis), (c) y_{DA} and (d) W_{DA}.*

CHAPTER 5

Charm electron signal extraction and backgrounds

To examine the semileptonic decay of charmed hadrons an event sample with electron track candidates will be selected. The primary detector tools for doing this are the calorimeter and the central tracking detector. However, still a large fraction of these electron candidates are hadrons. The final number of events with real electrons is estimated after subtraction of this hadron contamination. To enable subtraction a pure hadron sample is selected, again with the calorimeter and central tracking detector, to make a precise estimate of the hadronic content in the electron sample. The extracted electron signal contains electrons from the semileptonic decay of charmed hadrons, photon conversion, Dalitz decay of π^0's and the semileptonic decay of beauty.

5.1. Electron identification in the calorimeter

In chapter 3 it has been explained how a distinction between an electromagnetic and hadronic shower can be made. In the ZEUS detector the energy deposit can only be measured in terms of total energy deposits in the different sections of the calorimeter (*EMC/HAC1/HAC2*). A good quantity to select electrons is the fraction of the total energy that is deposited in the electromagnetic section of the calorimeter (E_{EMC}/E_{TOT}). In figure 5.1 this ratio is shown for a Monte Carlo sample of both electrons and hadrons. The electrons indeed deposit well over 90 percent of the total energy in the *EMC*-section of the calorimeter. By applying a cut at a value of the ratio of $E_{EMC}/E_{TOT} = 0.9$ only 3.6% of the initial electrons are lost, compared to 37.9% of the initial hadrons. Hadrons clearly deposit their energy more evenly in both the electromagnetic and the hadronic sections. However, the tail above the 0.9 boundary in the distribution of the hadrons is non-negligible: the abundance of hadrons with respect to the number of electrons makes that the number of hadrons that satisfy this criterium dwarfs that of the electrons. An extra handle is needed to separate the produced electrons from the hadrons.

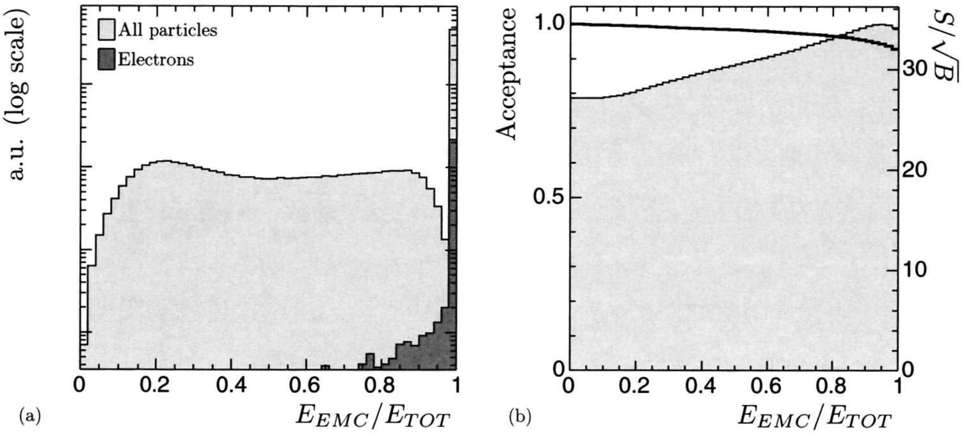

Figure 5.1: *(a) The calorimeter response in terms of* E_{EMC}/E_{TOT} *for both electrons and hadrons is shown. The particles were selected to have* $1.2 < p < 5.0$ *GeV. The electrons deposit almost all energy in the electromagnetic section of the calorimeter. The hadrons deposit their energy more evenly in the hadronic and electromagnetic sections. (b) The electron acceptance (solid line) and the signal/*$\sqrt{}$*(background) (filled histogram) as a function of the* E_{EMC}/E_{TOT} *ratio.*

5.2. Particle identification with dE/dx

In chapter 3 it has been argued that there is a relation between the normalised energy loss of a particle (dE/dx) and its momentum. In the momentum range that is of interest for this analysis (0.1-20 GeV) the dE/dx distribution of electrons is completely flat (Fig. 3.4). For particle momenta below 1 GeV the electron band is crossed by that of the π^-,K^- and $\overline{p}$, respectively. In this momentum region ($p \lesssim$ 1 GeV) it will be impossible to uniquely identify an electron. For momenta above 1.2 GeV the dE/dx does give the handle to identify an electron, as then the electron dE/dx -band becomes slightly separated from the rising hadron-bands. For particle momenta of the order of 10 GeV the correlation again becomes non-unique as the electron band is merged with the hadron bands, that are undergoing the so called relativistic rise.

The measurement of dE/dx with the ZEUS detector has been treated in chapter 3. In this section the motivation and methods of additional calibrations on the dE/dx will be given.

5.2.1. Space charge correction

The measured dE/dx of a particle shows a dependence on the polar angle θ of the trajectory. This polar angle is equivalent to the opening angle between the particle trajectory and the CTD sense wires. The dependence can be understood in terms of a geometrical effect, known as the *space charge effect* [68]. The total volume of gas

Figure 5.2: *Average value of dE/dx for a sample of conversion electrons as a function of polar angle. The error band shows the Gaussian spread of the fit on the peak position. A clear dip is visible when the particles pass the CTD wires with an angle close to 90°. The dashed line shows the expected average position of the peaks. The line shows the fitted 4th order polynomial that is used to correct for this effect.*

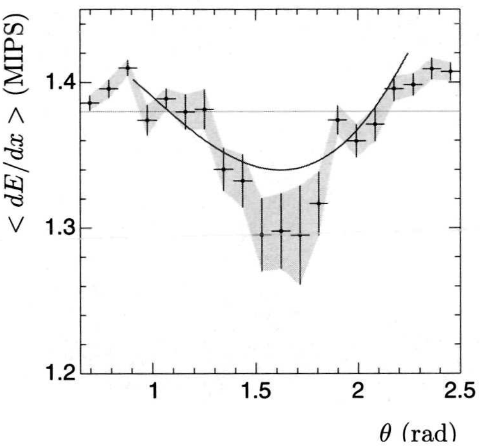

that can contribute to the signal on the wire is limited to a cylinder with a radius equal to the free electron drift velocity times the response time used in the read-out. This volume is further reduced by the length of the trajectory of the particle through this volume. The larger the volume of the contributing gas, the larger the number of potentially free electrons is and hence the lower the chance of saturation of the gas.

The gas saturation effect is directly proportional to the 'true' dE/dx of a particle: a lower true dE/dx means less secondary electrons, effectively reducing the needed gas volume to allow the secondaries to evolve into a full electron avalanche towards the sense wire. A direct effect of this is that the space charge effect is not visible for minimum ionising pions, so these can be used as the unity measure for the energy loss without complications. Other particles, with higher 'true' dE/dx value do show this effect, as is shown in Fig. 5.2 for a sample of photon conversion electrons. Photon conversion electrons have a very distinct topology which allows the selection of a very clean sample of pure electrons; the selection criteria applied will be discussed in Sec. 5.5.2. The dependence of the measured average dE/dx on the polar angle of the track, and thus of the angle with the CTD sense wires, is clearly visible as the drop in the average for θ values around 1.6 radians ($\approx 90^o$). To correct for this effect a fourth order polynomial in θ has been fitted to the conversion electron results. This fit is also shown in Fig. 5.2, as the solid line. Measured dE/dx -values are shifted by the difference between the function value for the tracks θ and the nominal dE/dx (= 1.38 MIPS).

5.2.2. Local multiplicity correction

The CTD response also shows a dependence on the local multiplicity of tracks, $\rho(n)$. To reveal this dependence, the average dE/dx is plotted for good tracks, where a good track is defined as vertex fitted, $1.2 < p < 5.0\,\mathrm{GeV}$ and $0.65 < \theta < 2.5$, rad binned in the number of other nearby good tracks, as illustrated in Fig. 5.3. Figure 5.4(a) shows the average dE/dx, $< dE/dx >$, for given $\rho(n)$ as a function of the opening angle Ω. For $\Omega = 0.7$ rad the distributions have flattened off enough that

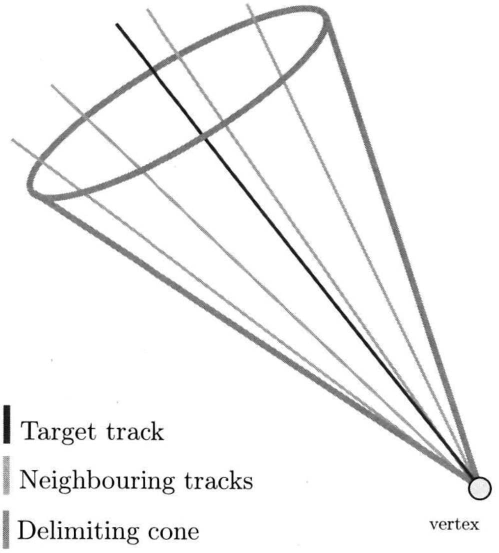

Figure 5.3: *A schematic view of the definition of $\rho(n)$: the number of tracks found in the cone that takes the target track as central axis and has an opening angle of 0.7 radians. In this case one would find $\rho(n)$ equals 4.*

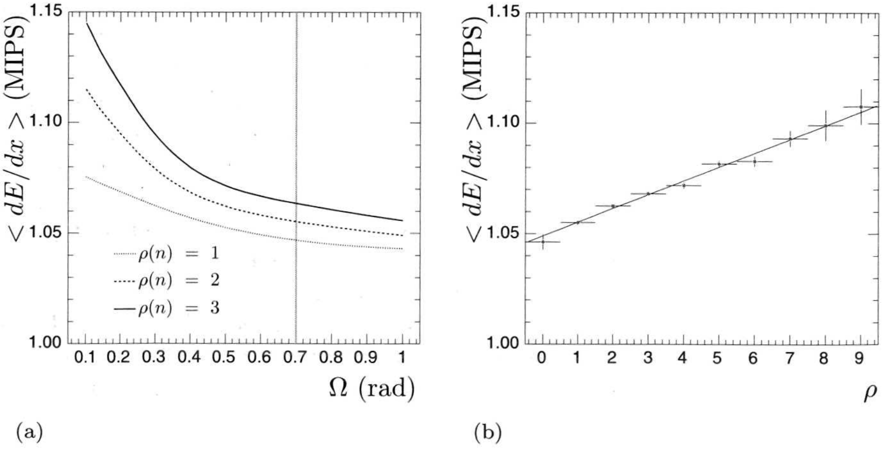

Figure 5.4: *(a) dE/dx as a function of the opening angle of the cone (Ω) at fixed values of charged track multiplicity. The effect stabilises for higher values of Ω. The value of 0.7 has been chosen in order to optimise the correction for a large range in $\rho(n)$. (b) dE/dx as a function of $\rho(n)$ is shown for a sample of pions ($1.2 < p < 5.0$ GeV, $0.65 < \theta < 2.5$ rad). The line is a first order polynomial that has been fit to the data for a cone opening angle of $\Omega = 0.7$ rad.*

it can be used as the defining opening angle for calibration. In Fig. 5.4(b) the average dE/dx is shown as function of the local multiplicity. There is a clear linear correlation between the two. The fitted function, also shown, is used to correct the data for this effect. The fact that this function does not pass through $dE/dx = 1$ for zero multiplicity is due to the selected momentum range, which selects pions with a higher than average momentum.

5.2.3. Track constraints

In order to maximise the use of the dE/dx-information, constraints have to be applied on the properties of the candidate tracks. The first set of selection criteria come from the desire to have an optimal resolution on the dE/dx measurement itself. A track that passes at least seven of the CTD superlayers has a well measured dE/dx value. This can be related to a cut on the polar angle of tracks that has an equivalent effect: $0.65 < \theta_{TRK} < 2.5$ radians. A second constraint arises from the wish to identify electrons: only tracks with a momentum above 1.2 GeV will be considered, to assure that the (p,dE/dx)-correlation can be used to identify electrons. These cuts allow the target electrons to be tagged with a very high efficiency, well over 90%. The downside of these two constraints is that almost 90% of the total semileptonic electron sample is lost due to the phase space constraints. This is illustrated in Fig. 5.5, where the results of pQCD calculation are shown for electron production from the semileptonic decay of charm. The accepted contribution is based on the polar angle ($0.65 < \theta_{TRK} < 2.5$ rad) and momentum ($1.2 < p_{TRK} < 5.0$ GeV) selection criteria.

5.3. Clusters and tracks

Based on the properties of electron showers in the calorimeter and the dE/dx measurement for tracks, a sample of electron candidates can be devised. The two reconstructed objects containing this data are *calorimeter clusters* and *vertex fitted tracks.* These two objects are reconstructed independently of each other and therefore it is needed to match a track uniquely to a calorimeter cluster. The match is made by extrapolating the track-trajectory until it reaches the calorimeter surface. This gives a set of coordinates on the calorimeter inner surface which allows for the calculation of distances between the track projection and calorimeter clusters center-of-gravity. A track is matched to the cluster if all of the following criteria are met:

- Distance between track projection and calorimeter cluster < 20 cm
- No other track projection within 25 cm of that of the matched track.
  Though it might be suspected that this cut would affect the charm signal greatly, this is fortunately not the case. This is due to the fact that the leptons from the semileptonic decay of the charmed hadron, which is produced in a jet itself, have a relative large transverse momentum with respect to this jet. Effectively this detaches them from the parent jet. The rationale behind this criterium is that if several tracks can be projected to the same calorimeter cluster, as tends to happen in jets, then the E_{EMC}/E_{TOT} ratio is not purely

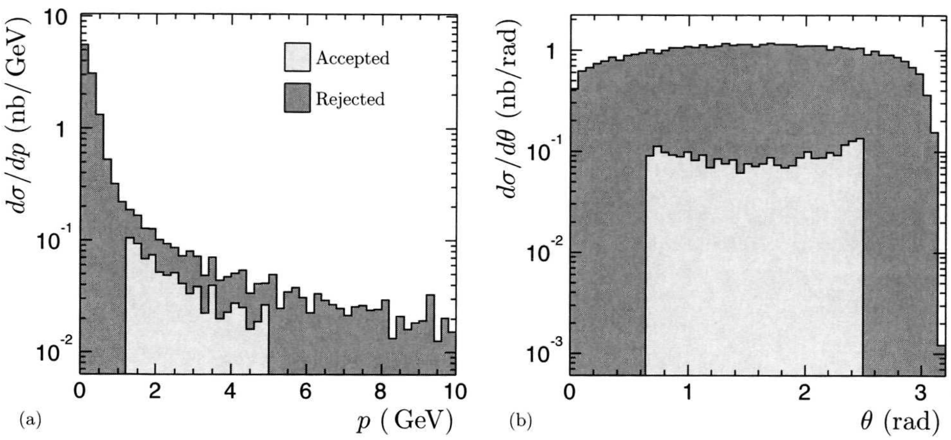

Figure 5.5: *Theoretical predictions (NLO pQCD) for the production of semileptonic electrons from charmed hadrons as function of the observables (a) p and (b) θ. The parts of phase space that are rejected are also shown. The motivation for also excluding the range of p larger than 5 GeV will be given in section 5.4.2 (page 62). A large fraction of the electrons produced by the semileptonic decay of the charm is lost due to the relative low momentum with respect to the lower boundary.*

that of the track associated with it. It will be a superposition of the responses of all particles that contributed to the cluster; such a cluster is not fit for identification uses.

- $0.2 < E_{CAL}/p_{TRK} < 3.0$
  These requirements ensure that the measurement of the energy of the cluster is not spoiled by neutral hadrons that may also deposit their energy there.

The distributions of these aforementioned variables are shown in Fig. 5.6. A comparison is made in the generic DIS Monte Carlo sample between an inclusive electron sample and a hadron sample ($E_{EMC}/E_{HAC} < 0.4$). This set of criteria selects the semileptonic electrons with a efficiency of about 70%. The dE/dx spectrum of the selected electron sample is shown in Fig. 5.7. The signal of electrons is still overwhelmed by a hadronic background which is the (stochastic) tail of the calorimeter ratio distribution for hadrons, resulting in hadrons that have a E_{EMC}/E_{TOT}-ratio bigger than 90%. This, convoluted with the resolution of the dE/dx measurement gives a very large 'tail' of hadrons in the dE/dx region where the electrons are located. There is need for 'a cunning plan' to remove this background from the signal.

5.4. The subtraction method

The ZEUS detector does not offer other observables that can be used to distinguish the electrons from the hadrons. However, a very clean hadron sample can be selected

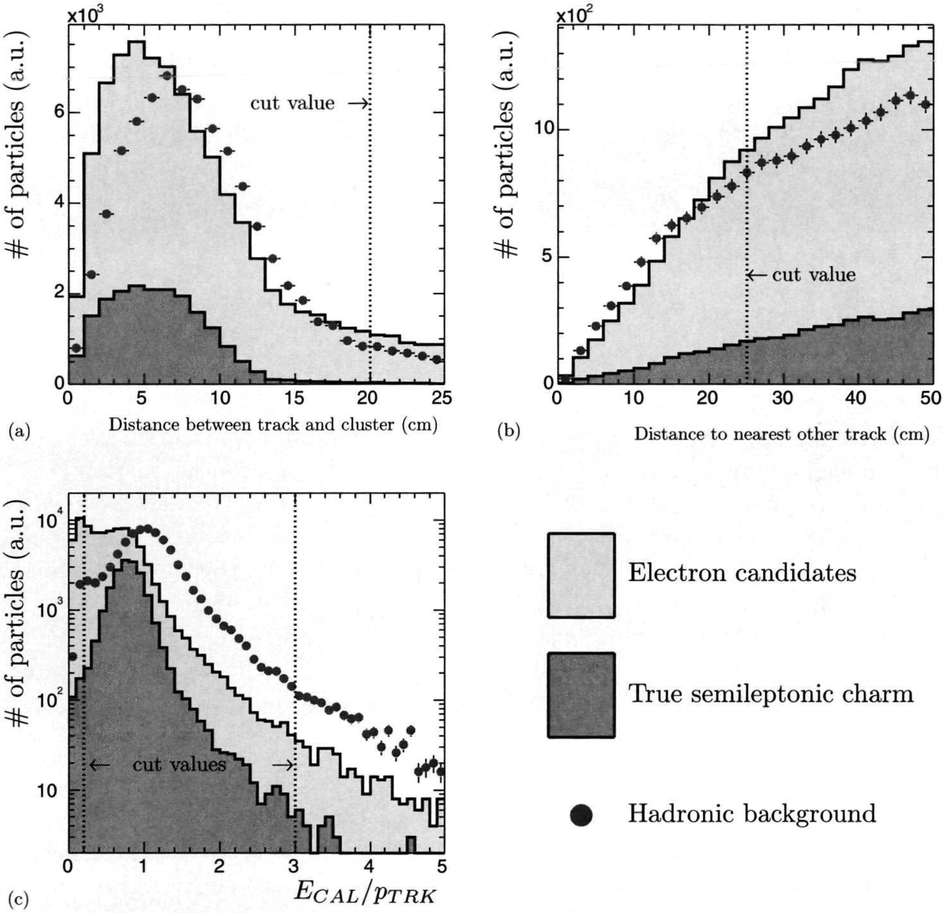

Figure 5.6: *Monte Carlo results for the three track-cluster variables used in the selection, for tracks in the used (p,θ)-window. The hadron sample has been scaled to the same integrated number of entries as the electron candidate sample. (a) The distance between the track projection on the CAL surface and the associated CAL cluster. (b) The isolation on the CAL surface of the track projection. (c) The generic match quality cuts on E_{CAL}/p_{TRK}.*

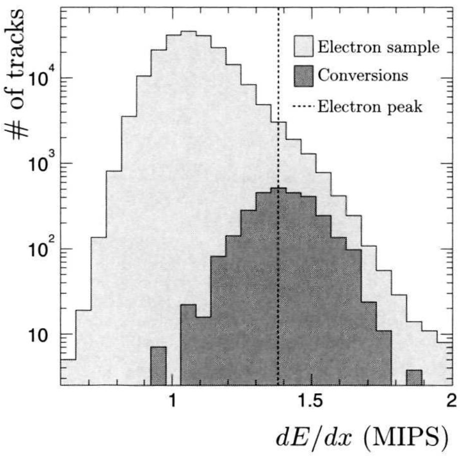

Figure 5.7: *The measured dE/dx distribution of all semileptonic candidate tracks. The dashed line indicates where the electron signal peak should be expected. The dE/dx distribution of a sample of clean conversion electrons, which is contained in the first sample, is also shown. The fact that the electron candidate sample peaks at 1 MIP makes clear that the sample suffers from a large hadronic background.*

by reversing the calorimeter principle that is used to select electrons. With a selection cut of $E_{EMC}/E_{TOT} < 0.4$, which replaces the ratio criterium of the electron sample, and keeping all other criteria the same, a clean hadron sample is obtained that can be used to understand the hadronic contamination of the electron candidate sample. The most direct approach to do this is found in the subtraction of the hadronic content from the electron candidate sample. To this end it has to be ensured that the pure hadronic sample has the same dynamical properties as that of the background in the electron candidate sample. The recipe that has been followed to perform the statistical subtraction is as follows.

5.4.1. Reweighting of the hadronic background

In figure 5.8 the ratio of hadron candidates over the number of electron candidates is shown in bins of p and θ. To correct for the differences the pure hadron sample is reweighted. The corrections are calculated on a two dimensional grid in p and θ.

This reweighting procedure also gives rise to the last cut that is necessary on the sample: all tracks with a momentum greater than 5 GeV have to be excluded to make the reweighting procedure stable: allowing higher momentum tracks would introduce (p, θ) bins that contain too few tracks to do proper reweighting.

5.4.2. Absolute calibration

After the reweighting the scaling factor for the hadronic sample to the electron sample is already close to unity. But since it is of utmost importance that the hadronic background beneath the electron peak in the electron candidate sample is quantitatively exactly described by the pure hadron sample, the hadronic sample is scaled to the electron candidate sample in a fiducial region of the dE/dx distribution: $0.8 < dE/dx < 1.1$. This includes the pion peak but is slightly asymmetric with respect to it, toward the lower edge. In this way a region in the dE/dx distribution is chosen that is extremely clean: in this region there are about 20 electrons in the elec-

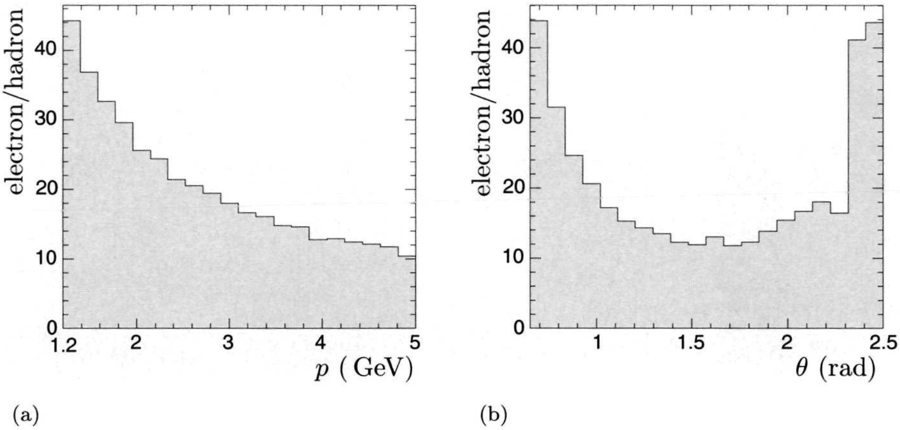

Figure 5.8: *(a) The ratio in bins of p of hadronic background candidates over the semileptonic candidates. The two distributions show large differences in some parts of the phase-space spanned by these the observables. (b) Likewise for the θ-distribution. The reweighting itself is performed using a two dimensional grid in (p, θ)-space.*

tron candidate sample, compared to 120.000 hadrons. This means that the hadronic purity is 99.98%. The scaling region is also indicated in Fig. 5.9(a).

5.4.3. Signal extraction and errors

The last step is the extraction of the number of electrons. By subtracting the hadronic sample from the electron candidate distribution the electron signal from Fig. 5.9(b) is obtained. The errors on the electron signal are calculated directly from the contents of both the electron candidate sample and hadronic background in the bin, *i.e.*

$$\sigma_i^2 = \sigma_{i,elec}^2 + \sigma_{i,had}^2 \tag{5.1}$$

As a consequence, bins that lie closer to the pion peak have larger errors. To reduce the sensitivity to these fluctuations the total number of electrons is extracted by integrating the upper half of the electron distribution only and subsequently extrapolating this to also include the lower half of the distribution. The dE/dx distribution of the electron signal is Gaussian. By gauging the centre and the width on a distribution of photon conversion electrons this method does not introduce any biases which might be hidden in the electron distribution itself. Fixing these two parameters in the fit on the electron signal only leaves the height of the distribution free, which is a direct measure for the actual number of electrons contained in the electron signal.

The funnel leading from the initial DIS sample to the final electron signal is summarised in Tab. 5.1. For completeness the numbers of charm tracks from the RAPGAP charm Monte Carlo sample are also given.

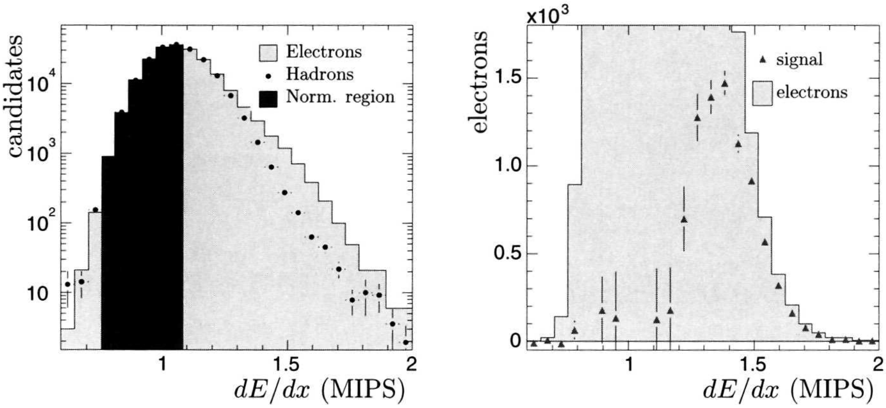

(a) (b)

Figure 5.9: *(a) The electron candidate and hadronic background dE/dx -distributions, after the reweighting and scaling of the latter. On the rising flank, the hadronic distributions follow the shape and size of the electron candidate sample perfectly. (b) The dE/dx -signal of the electrons in the semileptonic candidate sample after the subtraction of the hadronic background. The dE/dx -distribution of the initial semileptonic candidate sample is shown in the background. Statistical fluctuations in the original distributions have a relative large effect in the signal distribution, as can be seen on the rising flank of the electron signal, where some bins are even well below 0 (and thus of scale for this plot).*

Table 5.1: *Overview of the numbers of events/tracks available for the determination of the electron signal.*

Type	Source/Target	Sample size
Data	selected DIS events	1913128
	electron candidates	194676
	hadron candidates	134234
	- after reweighting and scaling	186415
	Electron signal	7758
Monte Carlo	SLe-c events	1938049
	SLe-c in (p,θ)-window	38493

5.5. Other relevant contributions to the signal

The electron signal that is obtained is an inclusive one. Apart from electrons from the semileptonic decay of the charm there are also electrons from other sources and a remnant of anti-protons. The contribution from each of these sources is determined and subtracted from the total number of electrons in the signal distribution. The backgrounds to this analysis are: anti-proton background (the only non-electron background), photon conversion, Dalitz decay of π^0 and semileptonic beauty decay.

5.5.1. Anti-proton background

The subtraction of the hadronic background is not 100% efficient for anti-protons. Though rather modest in size, it still contributes around 8% of the total electron signal [42]. This contribution is subtracted directly from the total number of electrons.

5.5.2. Photon conversion electrons

The process $\gamma \to e^+e^-$ is the second largest source of electrons in the electron signal. Photons are produced in large numbers at the primary vertex, mainly by the decay of the π^0 into two photons. Due to momentum conservation photon conversions only occur in the presence of a second object. This means that conversions take place in the detector material. There is a distinct displaced secondary vertex at which the conversion occurs. At this vertex an electron and a positron are produced and they can be reconstructed to a system with a invariant mass of virtually zero.

Electrons from photon conversions can be successfully identified by exploiting the distinct topology of the photon conversion. The efficiency for the reconstruction of the trajectory of the leptons is 95% for particles with a momentum over 200 MeV and $0.65 < \theta < 2.5$ rad (Fig. 5.10(a)). For lower momenta the efficiency drops rapidly. The reconstruction of the correct number of electrons that come from a photon conversion is assured by only looking at tracks with a momentum over 200 MeV. Inevitably some electrons that have a photon-parent will not be identified as a photon conversion electron, because the photon conversion leptons are known to sometimes have a large asymmetric momentum sharing, *i.e.* some photons produce a low momentum positron while the electron has a relative large momentum. It is crucial to correctly determine the number of these invisible conversions. In 1974 Tsai [69] derived the next-to-leading order quantum electro-dynamical (QED) equation for the initial energy sharing between the two leptons from a photon conversion. In Fig. 5.10(b) the number of reconstructed conversions where both leptons have a track momentum above 200 MeV is compared to the prediction from the Tsai calculation. There is good agreement between the measured numbers and the theoretical prediction. This shows that the Tsai equation can be used to correct for the fraction of conversions that are missed due to the momentum requirement. Figure 5.11 shows the fraction of visible conversions as function of the energy of the parent photon with the requirements $p_{e+} > 200\,\mathrm{MeV}$ and $p_{e-} > 1.2\,\mathrm{GeV}$. This histogram is used to correct for the *a priori* invisible conversion electrons.

In short, the contribution of photon conversions to the total electron signal can be determined by making use of the accurate reconstruction of the distinct event

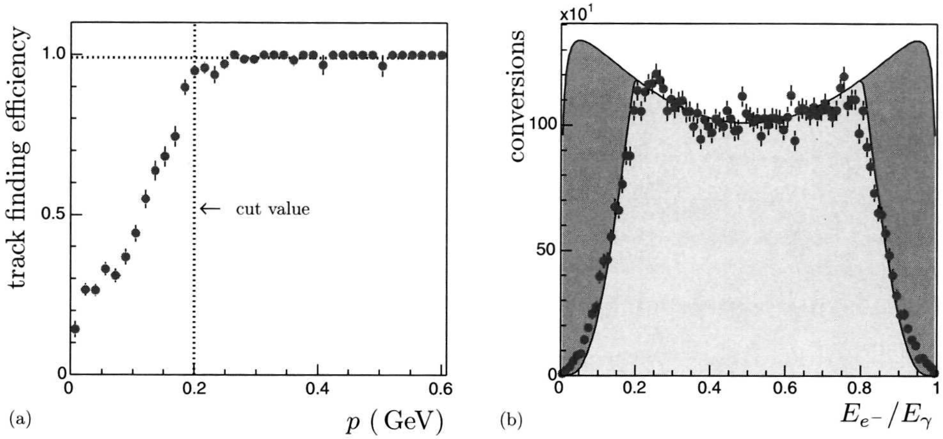

(a) (b)

Figure 5.10: *(a) The efficiency for reconstructing a vertex track as a function of the particle momentum. (b) The measured energy sharing distribution (E_{e^-}/E_γ) from the clean conversion sample with the momentum of the tracks > 200 MeV. The light area gives the prediction of the Tsai calculation. The dark area gives the prediction for the case with no track-momentum cuts applied.*

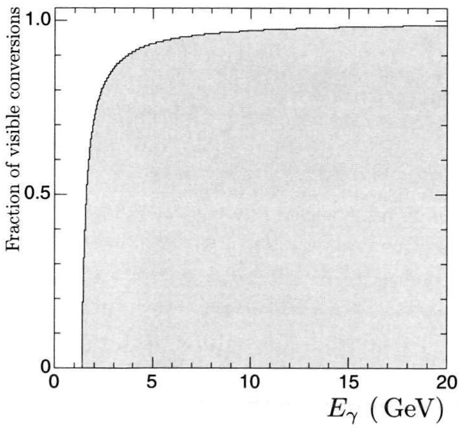

Figure 5.11: *The fraction of visible conversions over invisible conversions, due to the applied cut on the lepton momentum ($p^{e+} > 200\,MeV$,$p^{e-} > 1.2\,GeV$), as a function of the reconstructed photon energy according to the Tsai calculation. The weight that is applied to the found conversions is the inverse of this fraction.*

topology in a well understood part of the phase space, which can be expanded to the full phase space by using NLO-QED calculations.

The conversion tagging is still not 100%, even allowing for the minimal track momentum requirement. The efficiency to tag a conversion electron was found to be 89.5% in Monte Carlo. The found number of electrons have been corrected for this.

5.5.3. Dalitz decay of the pions

The second largest non-charm contribution of electrons to the signal is by the Dalitz decay of neutral pions: $\pi^0 \rightarrow \gamma e^+ e^-$. The branching ratio for this decay is very

Figure 5.12: *The smallest reconstructed invariant mass for a sample of Dalitz decay electrons and electrons from the decay of charmed hadrons. Electron candidates are tagged as a Dalitz electron if they reconstruct to a minimum invariant mass of less then 0.2 GeV.*

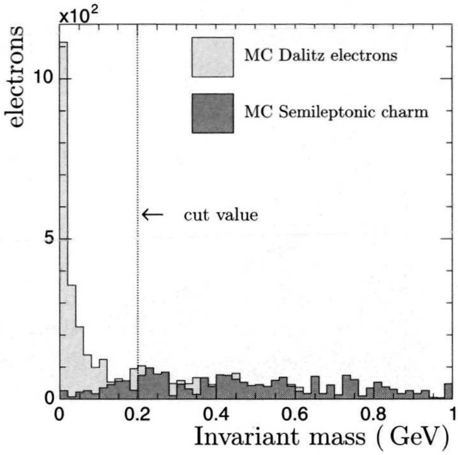

small, only 1.198 ± 0.032 % [36]. Nevertheless, due to the large abundance of neutral pion production in generic DIS events it is a background that has to be estimated correctly.

The Dalitz decay of pions occur directly at the primary vertex. Therefore, electrons produced in this process are experimentally *a priori* not distinguishable from the electron produced by the decay of a charmed hadron. To determine the background from this process three, in principle independent, methods have been investigated.

Monte Carlo prediction

The first, and most simple, is the counting of selected electrons from a Dalitz decay in a large sample of generic DIS Monte Carlo. This method is cumbersome as it relies on a very large Monte Carlo sample to get a statistical accurate estimate. This method also implicitly shows a great dependence on the Monte Carlo simulation of π^0 production in DIS. Data from e^+e^- collider experiments on π^0 production have been used as input for the Monte Carlo. In first order this will certainly be a valid *ansatz*, but this is by no means an assurance that, for the case of e^+p scattering, it will describe the pion production well enough to allow the extraction of the size of the background directly from Monte Carlo.

Invariant mass reconstruction

The second method is based on the reconstruction of the invariant mass. As the Dalitz decay of the π^0 occurs virtually at the primary vertex, the following algorithm is used:

1. every electron candidate, not tagged as a photon conversion electron, is combined with every other vertex fitted track of the opposite charge, not tagged as conversion positron.

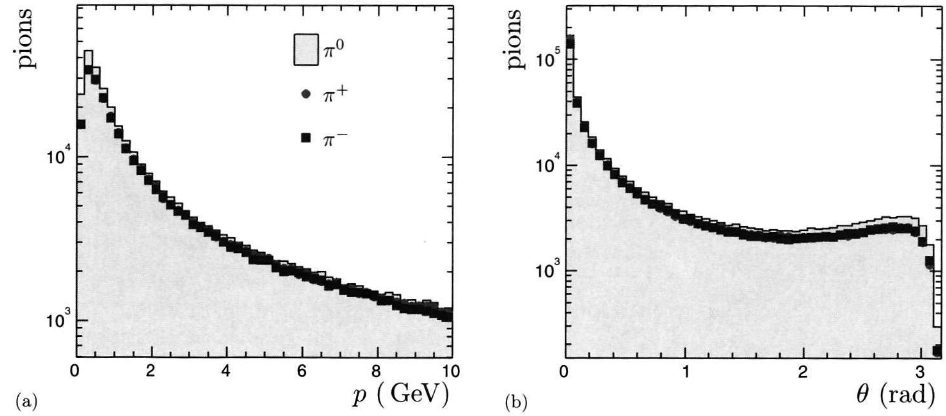

Figure 5.13: *A direct comparison of the (a) production momentum and (b) production angle between the three pionic flavours. The three distributions are, apart from a slight normalisation factor for the π^0, in excellent agreement. The π^+ results are mostly hidden by the distributions of the negative pion.*

2. an invariant mass is reconstructed based on the assumption that the tracks are an electron and a positron.
3. if the invariant mass is less then 200 MeV then the electron candidate is tagged as a Dalitz electron.

The combination with the smallest invariant mass is plotted in Fig. 5.12. The number of electrons found in this manner needs to be corrected for the in-efficiency of the method. The methods efficiency is determined from Monte Carlo simulation and is found to be 68.1 ± 9.1%, where the error is purely statistical. This algorithm has quite good accuracy, due to the fact that it takes the actual data to determine the background and it is only moderately dependent on Monte Carlo results.

Charged track multiplicity

The last method is also the most elaborate method. It takes advantage of the total charged track multiplicity. Figure 5.13 shows the comparison of production momentum and angle for the three flavours of pions, π^+,π^- and π^0. The three pions show similar production distributions, apart from a slight normalisation difference. This shows that it is reasonable to use the charged pions to estimate the number of electrons from the Dalitz decay of the π^0.

The first step in this process is to determine the fraction of charged pions in the total charged track multiplicity. This number has been obtained from a large sample of inclusive DIS Monte Carlo. The result of this study is

$$\frac{N(\pi^+ + \pi^-)}{N(X^+ + X^-)} = 0.57$$

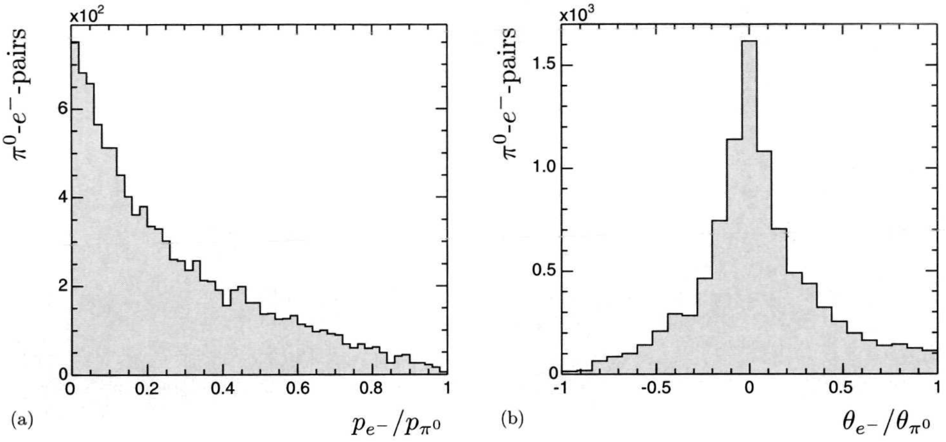

Figure 5.14: *(a) The fraction of momentum from the parent pion carried of by the Dalitz electron. On average, the electron only gets a very small fraction of the initial momentum, greatly reducing the number of electrons that are accepted by the momentum range. (b) The direction of the produced electron with respect to the parent direction of the polar angle. These two distributions are used to estimate the number of electrons from the Dalitz decay that contribute to the total electron signal by using the total charged track multiplicity.*

in the momentum and polar angle window that is of interest for this analysis.

The second ingredient is the normalisation factor between the neutral and the total charged pion rates. The number is also obtained from Monte Carlo (effectively from the distributions in Fig. 5.13) and is found to be

$$\frac{N(\pi^0)}{N(\pi^+ + \pi^-)} = 0.55,$$

which is almost in accordance with isospin conservation. It is expected that the isospin symmetry for pion production is slightly broken in the *ep* DIS events, which is in good agreement with this number. These two numbers are constant over a wide range in p and θ and with these two numbers one derives the initial number of π^0 in the total sample. The charged tracks have to be convoluted with the energy sharing of the parent pion to the electron and the recoil angle (in the polar plane) of the electron with respect to the parent. The distributions of Fig. 5.14 are used for this. Random numbers are generated according to these two distributions, which hold all the information of the Dalitz decay, and applied on the momentum and polar angle of the charged track. Only those tracks are considered that after this convolution still pass the track selection criteria. The integrated total of such tracks is corrected for the branching ratio of this decay to yield the size of the Dalitz decay contribution.

The last step is to correct for the difference in selection efficiency of Dalitz decay electrons and semileptonic charm electrons. Whereas the later have a high detection efficiency, based on the set of cuts described earlier, this is not true for the Dalitz

Table 5.2: *An overview of results of the three methods to reconstruct the contribution of the Dalitz decay to the electron signal. The combined result the average of the last two quoted methods with the error based on the spread between them.*

Method	Contribution
Monte Carlo counting	154 ± 30
Invariant mass reconstruction	310 ± 18
Total charged track multiplicity	352 ± 8
Combined result	331 ± 27

decay electrons. This difference can be easily understood in terms of the decay itself: the pion has a lower mass than the charmed hadrons. A higher mass translates into to a higher relative transverse momentum for the decay products with respect to the initial vector: electrons from the semileptonic decay are found on the outskirts of the jet profile, while the Dalitz decay products stay in the core of the initial jet and are thus vetoed by the isolation criterium.

The method described above is dependent on the correct description of the Dalitz decay in the Monte Carlo. However, it can safely be assumed that the kinematics of this decay are well known to allow for the extraction of the convolution distributions in momentum and polar angle. There is also a Monte Carlo simulation dependence in the numbers that translate the total charged track multiplicity to the number of produced neutral pions. However the advantage is a high statistical accuracy that is obtained by using all the charged tracks available: a sample of almost 1.5 million tracks.

In table 5.2 an overview is shown of the results of the three methods described above, based on the 1996-1997 event sample. Though the results are all of the same order of magnitude there is no clear agreement, nor disagreement, between the methods. The Monte Carlo counting method deviates so much from the other two that it is not used further. The subtracted Dalitz electron background is based on the average of the remaining two methods.

5.5.4. Semileptonic decay of beauty

Not only the charm quark is subject to a semileptonic decay. The same is also true for beauty quarks. Beauty production in QCD has a higher threshold in terms of Q^2 due to the higher mass of the quark: 4.5 GeV compared to 1.3 GeV for charm quarks. Beauty pairs will only be produced if the energy of the process is around twice the square of the quark mass: it starts to develop at $Q^2 \approx 30\,\text{GeV}^2$. The production cross section of beauty is additionally suppressed by the lower electric charge of the quark. The beauty quark has a charge of 1/3 compared to 2/3 for charm. As the boson-gluon-fusion process is proportional to the square of the electric charge, this reduces the cross section by a factor of four with respect to the charm production cross section. All this results in a small contribution of the semileptonic decay of

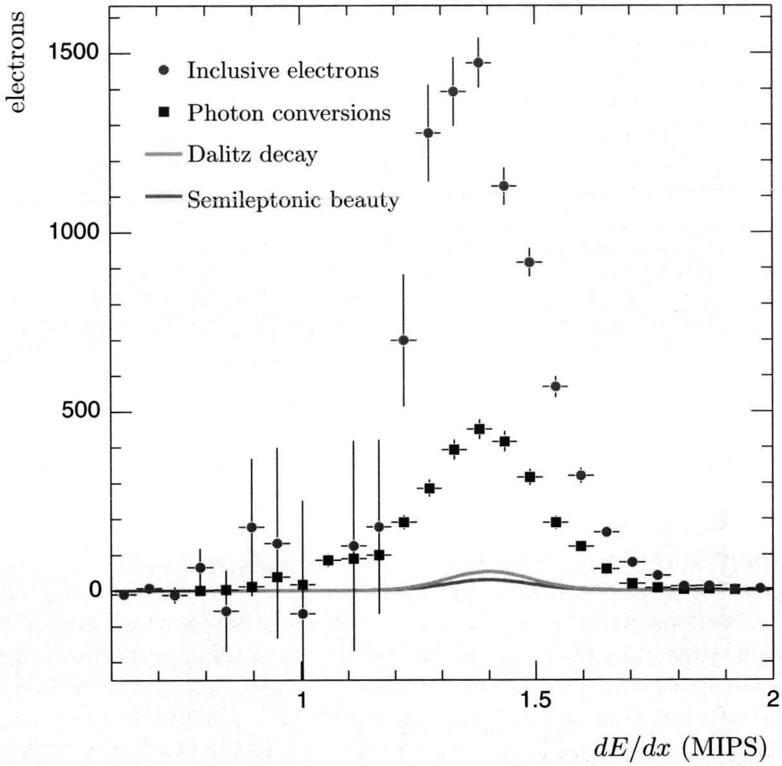

Figure 5.15: *The electron signal broken down into the different electron contributions. The quoted uncertainty is the statistical error only.*

beauty to the total electron signal. The most straightforward method to estimate this background is therefore chosen: directly from Monte Carlo simulation. The RAPGAP generator is used for the generation of the sample, with all settings identical to that for the signal sample, but for the produced quark. The contribution is estimated from a sample of 179.328 events with a semileptonic electron, either from beauty or charm decay. Of these events, 9589 electrons passed all the requirements for events and track selection. When corrected for luminosity, this yields a contribution of 211 electrons or 3% to the total electron sample.

5.6. Putting it together

By combining the calorimeter information with the differential energy loss in the CTD (Fig. 3.4) it is possible, to extract an electron signal (Fig. 5.9). With the inclusion of the four background sources from the previous section all the non-charm

Table 5.3: *The total number of electrons broken down to the different contributions.*

Category	Number of electrons
total signal	7758 ± 174
photon conversion	3127 ± 87
proton background	622 ± 14
Dalitz decay of pions	332 ± 27
semileptonic decay of beauty	211 ± 2
semileptonic decay of charm	3468 ± 197

contributions to the total electron signal are known. Figure 5.15 shows again the total electron signal but also shows the electron background sources superimposed. The semileptonic charm signal is the result of the subtraction of all the background sources from the total number of electrons in the signal. The results are also summarised in Tab. 5.3.

The largest background contribution, photon conversions, is well understood. The contribution from Dalitz-electrons is perhaps not as well understood, but considering the relevance to the total signal, around 4%, the overall contribution to the systematic uncertainty is small. Beauty production hardly contributes at all and at this stage it is clear that this analysis, with this set of cuts, holds no sensitivity to measure it concurrently with charm production.

The result is a sample of 3468 electrons from the semileptonic decay of charmed hadrons. In the next chapter this is converted to a visible cross section. The analysis will be extended to give differential cross sections. The double differential cross section (in Q^2 and x) will be used to determine the contribution of charm to the proton structure.

CHAPTER 6

Results from the semileptonic charm

From the events with a possible electron from charm we want to determine a production cross section. In this chapter the cross section calculation is explained, followed by a review of experimental uncertainties. The differential cross sections give more detailed information about the underlying hard production process, which then can be compared to NLO-pQCD predictions. Finally the charm structure function $F_2^{c\bar{c}}$ is extracted to allow a direct comparison of the inclusive charm production measurement of this analysis with the published D^* measurements of the ZEUS [70] and H1 [71] experiments.

6.1. From signal to cross section

The production cross section in a given region of phase space is given by

$$\sigma = \frac{N^{data}_{electron}}{\epsilon_{DIS} \cdot \epsilon_{SLe} \cdot \mathcal{L}} \tag{6.1}$$

where $N^{data}_{electron}$ is the measured number of electrons from the semileptonic decay of charm, ϵ_{DIS} is the efficiency to select a DIS event with a semileptonic electron, ϵ_{SLe} is the efficiency to tag the semileptonic electron in this sample and $\mathcal{L}$ is the integrated luminosity used. For a single differential cross sections the following equation is used:

$$\frac{d\sigma}{dX} = \frac{N^{data}_{electron}}{\epsilon_{DIS} \cdot \epsilon_{SLe} \cdot \mathcal{L} \cdot \Delta X} \tag{6.2}$$

where X can be any kinematic observable and ΔX denotes the size of a given bin in X. The double differential cross section is given by

$$\frac{d^2\sigma}{dXdY} = \frac{N^{data}_{electron}}{\epsilon_{DIS} \cdot \epsilon_{SLe} \cdot \mathcal{L} \cdot \Delta X \cdot \Delta Y} \tag{6.3}$$

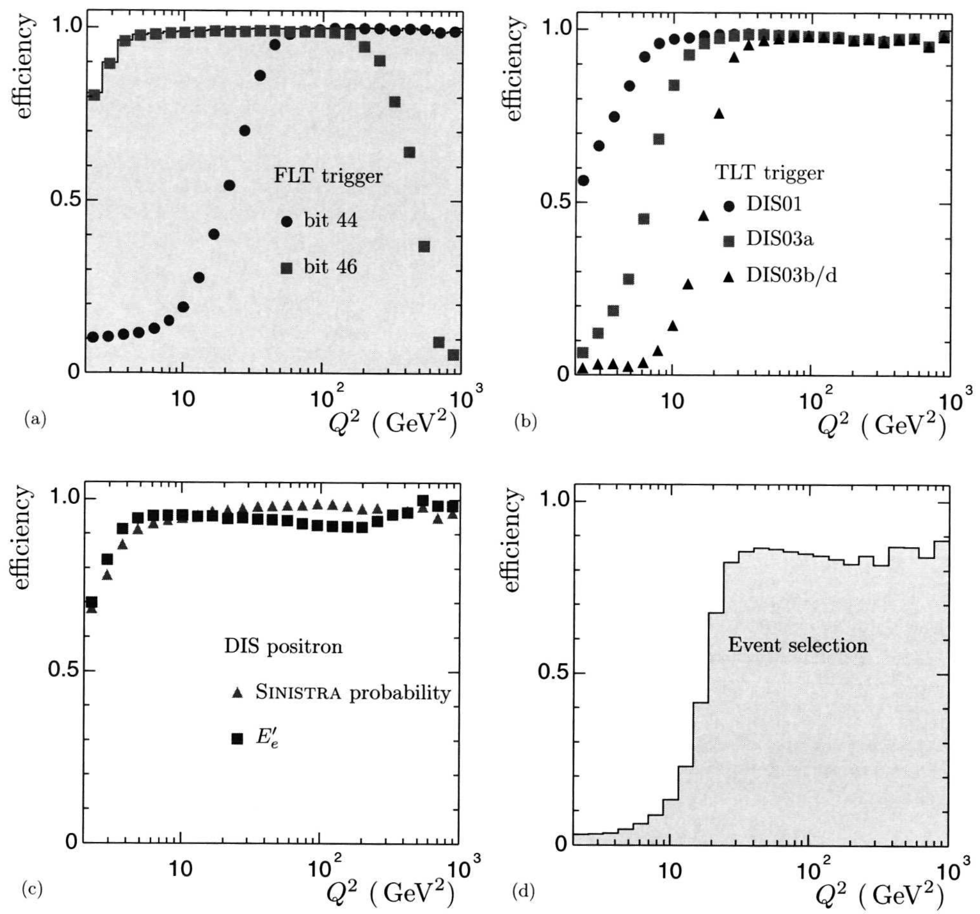

Figure 6.1: *The selection efficiencies for the different components of the event selection as a function of Q^2 as well as the combined (total) selection efficiency.*

where X and Y are different kinematic observables. With these tools in hand the measurement of the number of electrons can be confronted with theoretical predictions.

6.2. Selection efficiency

6.2.1. Event selection efficiency

The efficiency to select DIS semileptonic charm production events is estimated from Monte Carlo. The event selection efficiency is given by:

$$\begin{aligned} \epsilon_{DIS} &= \frac{N^{selected}}{N^{generated}} \qquad (6.4) \\ \text{for events with} &: \; 2 < Q^2 < 1000 \text{ GeV}^2, \\ & \quad\; 0.03 < y < 0.70. \end{aligned}$$

Figures 6.1(a) and (b) show the selection efficiency for the different trigger slots at the first and third level respectively and (c) for the selection criteria of the scattered positron. The combined event selection efficiency is shown in Fig. 6.1(d). All are shown as a function of Q^2. At low Q^2 there is a clear effect of the cuts on the position of the scattered electron in the third level trigger. For $Q^2 \gtrsim 20$ GeV^2 the selection efficiency converges to a value of 0.90. The event selection efficiency for the whole Q^2-region was found to be 38.3%.

6.2.2. Semileptonic electron finding efficiency

For the electron tagging efficiency the following relation is used:

$$\begin{aligned} \epsilon_{SLe} &= \frac{N^{selected}}{N^{generated}} \qquad (6.5) \\ \text{for electrons with} &: \; 1.20 < p^{SLe} < 5.00 \text{ GeV}, \\ & \quad\; 0.65 < \theta^{SLe} < 2.50 \; rad, \end{aligned}$$

with the additional requirement that the semileptonic electrons are produced in events that have passed the event selection criteria. This electron selection efficiency is the convolution of the track finding, calorimeter selection and cluster-track matching efficiencies. These efficiencies are shown separately in Fig. 6.2 both as a function of track momentum, p^{SLe}, and as a function of the polar angle, θ^{SLe}. The dip in the efficiency for $\theta \approx 2.25$ rad is due to the super crack region, which is the opening between RCAL and BCAL for the readout cables an cooling of the inner detector subcomponents. The tagging efficiency, after integrating over the whole p^{SLe} and θ^{SLe} range, was found to be 72.4%.

6.3. Sources of systematic uncertainties

Before a sensible comparison between data and theory can be made it is necessary to quantify the uncertainties in the measurements. Looking at the source of these uncertainties, they can be divided in three different categories: *event selection*, *electron selection* and *background subtraction related*. The effect of these uncertainties is estimated by changing the selection thresholds for the first two categories, and by varying the net contribution to the total electron signal within the limits of the expected uncertainty for the background sources.

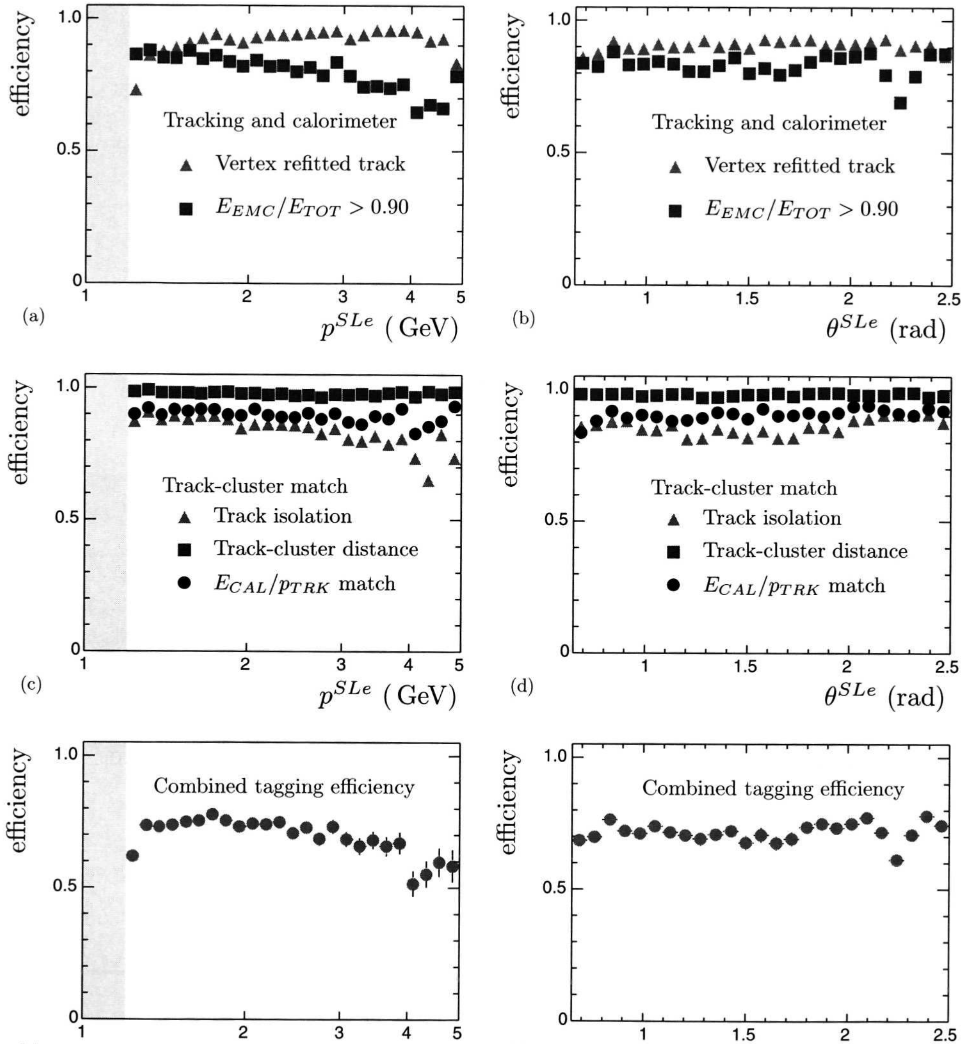

Figure 6.2: *The efficiency to select a semileptonic electron in a sample of events that have passed the initial event selection criteria. The efficiencies from top to bottom: track finding and calorimeter tagging, cluster-track matching and combined selection. On the left hand side these are shown as a function of momentum, the right hand side as a function of polar angle.*

Table 6.1: *An overview of the event selection related systematic studies.*

Variation	effect (%)
Increase δ window	-0.56
Decrease δ window	0.87
Increase z_{vertex} window	0.25
Decrease z_{vertex} window	0.83
Expand H1-box cut	-0.70
Increase minimum E'_e energy	-0.87
Decrease minimum E'_e energy	-0.78
Combined up	1.23
Combined down	1.47

6.3.1. Event selection induced uncertainties

In the selection of the DIS events, both online and offline, a bias might be introduced to the final event sample. The checks performed to study the size of such effects are

- δ of the event
  The δ-distribution is typically the place where photoproduction background raises its head. By varying the borders of the acceptance window with 4 GeV, such a background can be identified.

- vertex distribution
  The efficiency of track finding and the subsequent vertex fitting is dependent on the location of the primary vertex. As this analysis is exceptionally sensitive to any effects in the track and vertex finding the accepted vertex region was varied by ± 5 cm.

- the scattered electron position
  The simulation of the detector response in the region which corresponds to a (relative) low scattering angle for the DIS positron is known to be very difficult. To quantify this effect the H1-box cut was expanded in every direction by 1 cm.

- scattered electron energy
  The minimum required energy for the scattered DIS electron was varied by 1 GeV to account for any differences in the electron finding efficiency of the neural network SINISTRA.

The effect of these variations of event selection criteria is summarised in Tab. 6.1. The studies give an estimated uncertainty on the final results of (+1.23;-1.47)%, which was obtained by adding the individual sources in quadrature.

6.3.2. Electron selection induced uncertainties

The electron selection efficiency as a function of the applied selection criteria is studied as follows.

Kinematic acceptance

As only a small part of the allowed phase space is accepted for this analysis, there can be a sensitivity to effects in the modelling of the hadronisation and semileptonic decay processes in the Monte Carlo. To estimate any such systematic biases the dependence of the electron finding efficiency on the allowed phase space is studied in Monte Carlo.

- variation of momentum window by ± 0.1 GeV
  The momentum range was in total made larger (smaller) by 0.2 GeV, *i.e.* the momentum range was changed $1.1 < p < 5.1$ GeV and $1.3 < p < 4.9$ GeV in Monte Carlo. As this variation exceeds the detector resolution of the track momentum, this is a measure of the biases introduced by the Monte Carlo in the modelling of the semileptonic decay of charmed hadrons.

- variation of the polar angle window by ± 0.05 rad
  The same holds here as for the study of the momentum range dependence.

Track-cluster matching

- track isolation
  The radius of the circle that defines the isolation space has been varied by ± 5 cm. This will quantify any differences in the particle-jet structure[1] as seen in the data and simulated in the Monte Carlo.

- track-cluster matching
  The separation between the track-projection and the cluster-center was varied by ± 3 cm around the default. This study effectively compares the Monte Carlo parametrisation of the detector material to the real setup that was used for the measurements.

Calorimeter

The ratio of electromagnetic and hadronic energy that define the electron candidate and hadron samples are the core of the analysis. The effect of the hadron mixture in both the electron candidate and hadron sample, and thus the shape of the inclusive electron candidate and hadronic background sample dE/dx distribution, is investigated.

- electron candidate
  The calorimeter energy ratio E_{EMC}/E_{TOT} is varied with ± 5% from 0.9, to 0.85 and 0.95 respectively.

- hadronic background selection
  E_{EMC}/E_{TOT} is changed by ± 10%, which is larger than for the electron selection. It is expected that the mixture of the hadron sample depends more critically on the ratio-requirement than that of the electron candidate sample.

---

[1] In the case of the electrons this also tests the subsequent separation of the decay electron from the parent jet.

Table 6.2: *An overview of the track selection related systematic studies.*

Variation	**Effect (%)**
Increase momentum window	-1.53
Decrease momentum window	2.05
Increase polar angle window	-1.17
Decrease polar angle window	2.05
Increase isolation	-0.75
Decrease isolation	0.00
Increase match distance	-0.09
Decrease match distance	0.09
Increase E_{EMC}/E_{TOT} for electron	-0.11
Decrease E_{EMC}/E_{TOT} for electron	1.35
Increase E_{EMC}/E_{TOT} for hadron	-0.58
Decrease E_{EMC}/E_{TOT} for hadron	0.74
Combined up	3.29
Combined down	2.15

In Tab. 6.2 the results of these studies are summarised. The quoted combined result is obtained by adding the separate sources in quadrature. This group is the second largest source of (systematic) uncertainty on the final result (+3.3;-2.2)%.

6.3.3. Background sources uncertainties

- photon conversions
  By loosening (tightening) the cuts on the reconstructed secondary vertex of the conversion the contribution of this background to the signal was systematically raised (lowered).

- Dalitz decay of π^0
  The contribution of this process to the total electron signal was varied by ±6.6%, which covers the spread on the average number of the two methods used to determine the background.

- Semileptonic decay of beauty
  Current measurements show that there might be a rather large discrepancy between the theoretical prediction for the beauty production cross section and the measurements. The contribution of the semileptonic decay of beauty was varied by a factor of 2, both up and down. This accounts for the current differences between the data and theory.

The effect of these studies is given in Tab. 6.3. The uncertainty on the beauty contribution to the total electron signal is the single largest contribution to the systematic uncertainty in this analysis. The total systematic uncertainty due to electron backgrounds is (+3.69,-6.20)%.

Table 6.3: *An overview of the background related systematic studies.*

Variation	Effect (%)
Increase conversion acceptance	-0.92
Decrease conversion acceptance	1.95
Increase Dalitz background	-0.61
Decrease Dalitz background	0.61
Increase Beauty background	-6.09
Decrease Beauty background	3.03
Combined up	3.67
Combined down	6.18

6.3.4. Total systematic uncertainty

Overall it can be concluded that the event selection hardly induces any systematic effects to the final result. The typical size for the effects is of the order of 1%. The electron selection contributes about 3.5% to the systematic uncertainty. Especially the variation of the kinematic acceptance contributes a large fraction to the total error. The uncertainty due to the background electrons is the largest source of systematic uncertainty. The sole culprit for this is found in the semileptonic decay of beauty. This uncertainty can not be further reduced without accurate measurements of the beauty production cross section, preferable at HERA. The uncertainty due to the electron backgrounds is +3.7/-6.2%. In Fig. 6.3 all the results of these studies are summarised. The sequence of the points follow the list of studies as presented in this section. The total systematic uncertainty adds up to +5.1/-6.7%, which is comparable to the statistical error.

6.4. Total production cross section

The first experimental result that is extracted using the methods and knowledge described previously is the total visible production cross section. This is the cross section restricted to that region of phase space that is directly measurable. In the case of this analysis this turns out to be, based on the kinematic restrictions on the event and track samples: $2 < Q^2 < 1000$ GeV^2, $0.03 < y < 0.7$, $1.2 < p_{SLe} < 5.0$ GeV, $0.65 < \theta_{SLe} < 2.5$ rad. Within this region of phase space the results as shown in Tab. 6.4 were obtained.

The visible cross section measurement can be compared to NLO-pQCD predictions obtained with the HVQDIS programme, using the same phase-space restrictions. The results of the calculations are given in Tab. 6.5. The visible cross section was calculated for four different PDFs (ZEUS94, GRV98, CTEQ5F3 and CTEQ6) and in each case for three values of the charm quark mass: $m_c = 1.15/1.30/1.45$ GeV. The measured cross section is in agreement with all these results. The GRV98 set however yields a significantly lower value for the predicted cross section, but it is still consistent with the experimental result. The table also shows the effect of varying the

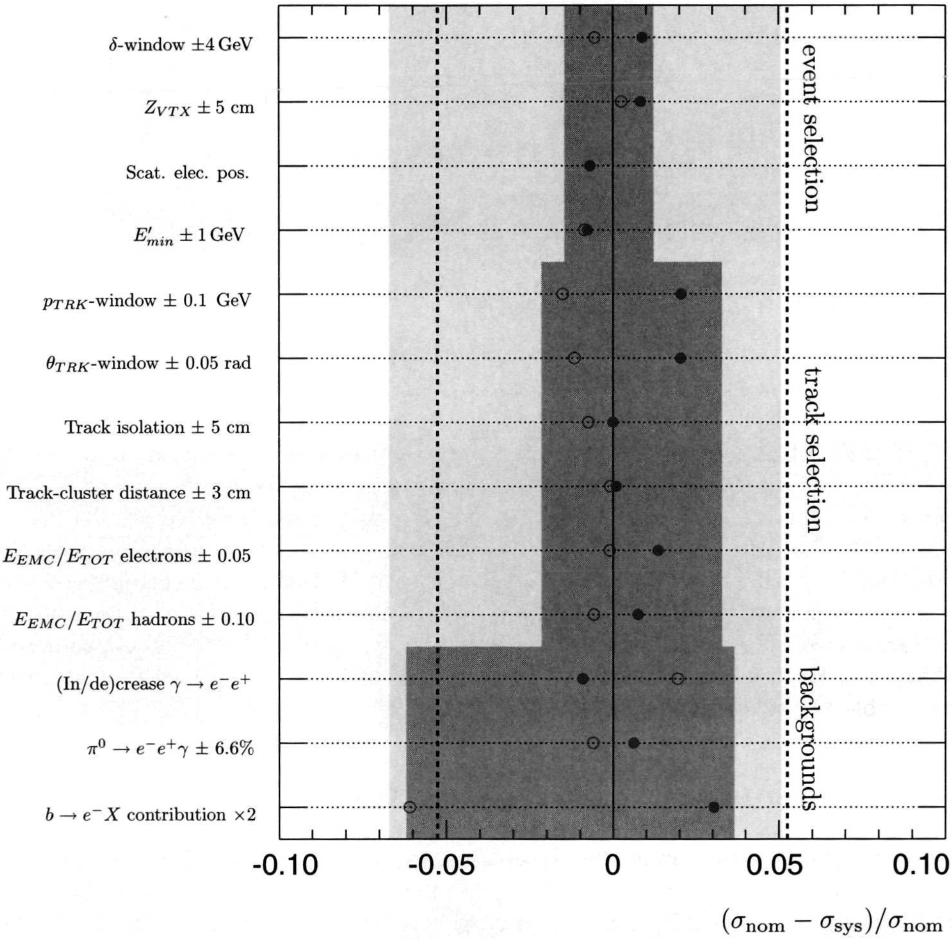

Figure 6.3: *The size of the contribution of the different systematic studies to the total systematic error for the total inclusive cross section. The light shaded band shows the total systematic uncertainty. The contribution of the three categories is shown as the dark band. The statistical error is given by the vertical dashed lines. The closed (open) points show the effect of the +(−)-variation. The labels refer to the descriptions in Sec. 6.3.1-6.3.3.*

Table 6.4: *Overview of the experimental results that lead to the visible cross section extraction.*

electrons	**number + stat. err.**
total signal	7758 ± 173
of which	
conversions	3126 ± 87
proton background	622 ± 14
Dalitz decay of π^0	331 ± 27
semileptonic decay of b	211 ± 2
semileptonic decay of $\bar{c}$	3468 ± 197

detection efficiencies & luminosity	
ϵ_{DIS}	38.3%
ϵ_{SLe}	72.4%
$\mathcal{L}$ (pb^{-1})	32.8 ± 0.7

visible cross section	
$\sigma^{\bar{c}\to e^- X}_{e^+p\to e^+c\bar{c}p}$ (pb)	380 ± 21 (stat) $^{+22}_{-18}$ (sys)

fragmentation function (parameter). This shows that both the charm mass and the fragmentation function change the measured total cross section significantly. This fact is taken up in Ch. 7, where m_c and ϵ_P will be extracted from the differential cross sections presented in the following section.

6.5. Differential cross section results

The available data sample allows the study of several differential cross sections. In this analysis two features of the production process can be examined: the kinematics of the underlying hard interaction and the cascade of processes that lead to the detected electron itself. The kinematics are studied by looking at the shape of cross sections differential in Q^2, x and W. This allows a comparison with the perturbative QCD calculation and a verification of the parameter settings as they were used in the numerical evaluation of the theoretical prediction. The cross sections differential in p_T and η of the produced electron give a more detailed handle on the production mechanism that is involved in the soft cascade of fragmentation and decay, but they also give a handle on the parameters that are involved in the hard scattering process itself. Notably, the p_T^{SLe} relates closely with the charm mass and the η^{SLe} gives information on the parton distribution of the gluon in the proton.

The measured differential cross sections are shown in Fig. 6.4. The efficiencies, backgrounds and systematic uncertainties were determined for each kinematic bin separately. The theory curves that are shown are the result of the HVQDIS pro-

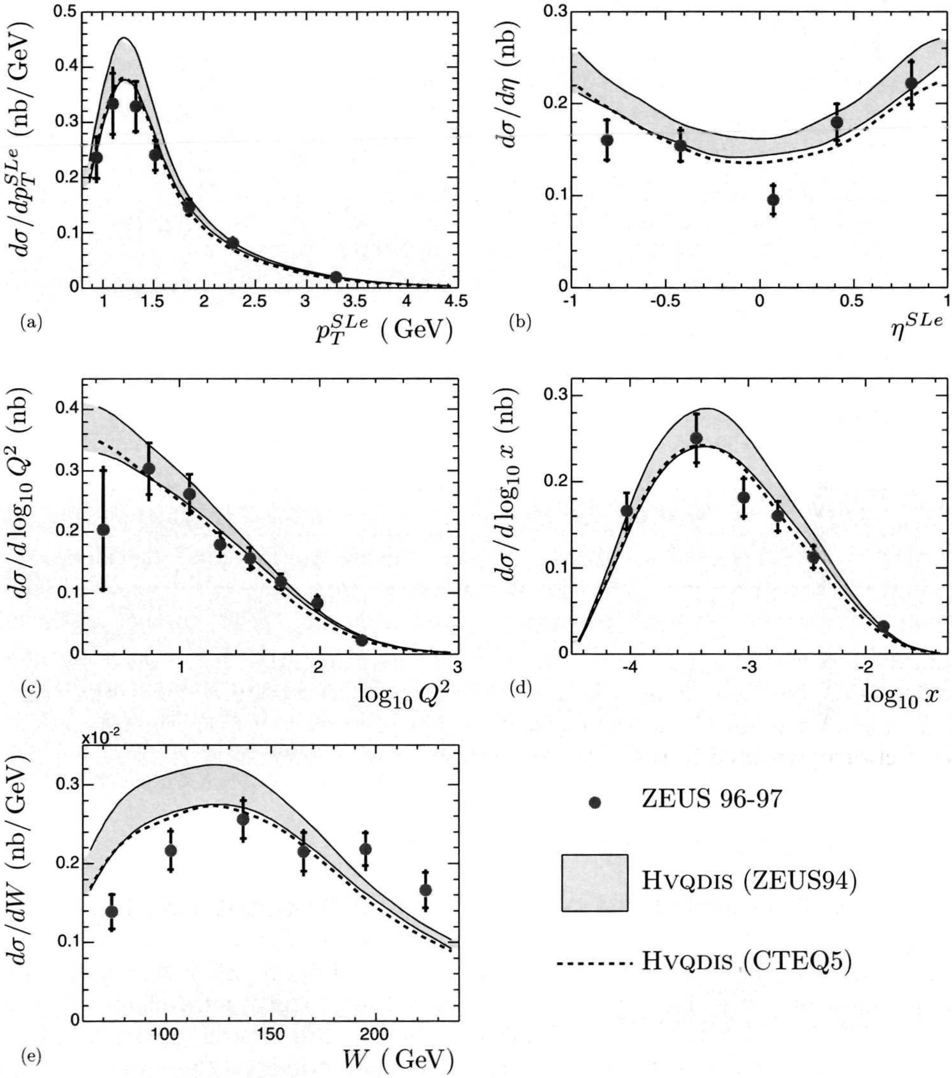

Figure 6.4: *The single differential production cross sections for semileptonic decaying charm as a function of (a) p_T^{SLe}, (b) η^{SLe}, (c) log(Q^2), (d) log(x) and (e) W. The shaded band gives the theory prediction for different charm masses ($m_c = 1.15/1.30/1.45$ GeV), based on the ZEUS94 PDF. In addition the prediction based on the CTEQ5 PDF for $m_c = 1.30$ GeV is shown (dashed line).*

Table 6.5: *A comparison between theoretical predictions of the visible semileptonic charm production cross section, with different input choices, and the measurement as presented in this thesis. The nominal mass is 1.3 GeV. The uncertainty quoted on the cross section is due to varying the mass to 1.15 and 1.45 GeV.*

PDF	fragmentation function	fragmentation parameter	σ_{HVQ} (pb)
ZEUS94	Peterson	$\epsilon = 0.035$	$415 \pm^{43}_{23}$
GRV98	Peterson	$\epsilon = 0.035$	$339 \pm^{37}_{34}$
CTEQ5F3	Peterson	$\epsilon = 0.035$	$384 \pm^{44}_{38}$
CTEQ6	Peterson	$\epsilon = 0.035$	$386 \pm^{38}_{35}$
CTEQ6	Peterson	$\epsilon = 0.025$	402
CTEQ6	Peterson	$\epsilon = 0.045$	372
CTEQ6	Kartvelishvili	$\alpha = 3.750$	384
Data			$380 \pm 21 \, ^{+22}_{-18}$

gramme, based on the ZEUS94 PDF and $\epsilon_{Peterson} = 0.035$. In general, there is agreement between the data and theory. Interesting is the fact that the forward η region (Fig. 6.4(b)) shows no hint of the proposed *beam-drag effect* which should explain a discrepancy in the same region when comparing theory prediction to results from the D^*-analysis [70]. However, it should be noted that, though there is a relation between η^{D^*} and η^{SLe}, it is not so simple that a direct comparison like this is justified. The deviations seen in the cross section as a function of W (Fig. 6.4(e)) are not understood. The difference seems to be due to some kind of shift, but the nature of such a shift is not understood. Despite this, the main conclusion is that NLO-pQCD DGLAP describes the production cross sections.

6.6. Double differential cross section and extraction of $F_2^{c\bar{c}}$

6.6.1. From cross section to structure function

Another convenient way to look at the data is found in the so-called reduced cross section, which is nothing more then the double differential cross section, but for the leading propagator term which has been divided out, *i.e.*:

$$\tilde{\sigma}^{c\bar{c}} = \left[\frac{2\pi\alpha^2}{xQ^4}(1+(1-y)^2)\right]^{-1} \frac{d^2\sigma^{ep\to ec\bar{c}X}}{dQ^2dx}, \tag{6.6}$$

which already has been restricted to the case of charm production for the purpose of this analysis. By dividing the propagator out of the measured cross section, the sensitivity for the structure functions of the DIS/quark parton framework comes out

Figure 6.5: *The binning in Q^2 and x for the measurement of the double differential cross section and the extraction of the reduced cross section and the structure function $F_2^{c\bar{c}}$. The numbers in the center of the bins correspond to the labelling of the measurements in the corresponding tables.*

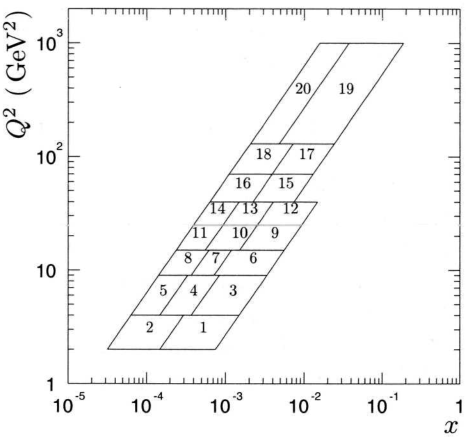

as

$$\tilde{\sigma}^{c\bar{c}} = F_2^{c\bar{c}}(x,Q^2) - \frac{y^2}{Y_+}F_L^{c\bar{c}} - \frac{Y_-}{Y_+}xF_3^{c\bar{c}}(x,Q^2), \tag{6.7}$$

where $Y_\pm = (1 \pm (1-y)^2)$ and all three inclusive structure functions are represented. By extracting the reduced cross section a model-independent measure of the charm structure of the proton is obtained. The charm structure function, for a given value of Q^2 and x is unfolded from the double differential cross section by assuming that

$$\frac{d^2\sigma^{e^+p\rightarrow e^+c\bar{c}X}}{dQ^2dx} \sim F_2^{c\bar{c}}, \tag{6.8}$$

i.e. that the contribution of $F_L^{c\bar{c}}$ and $xF_3^{c\bar{c}}$ to the cross section is negligible. In the region of phase space probed by this analysis this is certainly true for the $xF_3^{c\bar{c}}$ contribution. The $F_L^{c\bar{c}}$ contribution is not *per se* negligible. The validity of this assumption was studied by calculating the $F_L^{c\bar{c}}$ contribution to the total cross section directly from current PDFs and this was found to be of the order of a few percent. With the current statistical accuracy of the analysis it can therefore safely be neglected.

To extract $F_2^{c\bar{c}}$ from the double differential cross section the following unfolding method is used:

$$F_{2,\mathrm{data}}^{c\bar{c}}(Q^2,x) = \frac{\sigma^{data}}{\sigma^{theory}} \cdot F_{2,\mathrm{theory}}^{c\bar{c}}(Q^2,x), \tag{6.9}$$

which uses the NLO-pQCD predictions for both the $F_2^{c\bar{c}}$ and the cross section. The $F_{2,\mathrm{theory}}^{c\bar{c}}$ is extracted directly from the input PDFs and the cross section is calculated with the HVQDIS programme. The double differential cross section is measured in the (Q^2,x)-bins of Fig. 6.5. These bins have been selected such that the average number of signal electrons is approximately equal for all bins.

6.6.2. Electrons, efficiencies and systematics

The whole analysis as done for the total production cross section was repeated for the 20 individual bins of Fig. 6.5. The results on the electron signal composition, event selection efficiency and semileptonic electron tagging efficiency are summarised in Tab. 6.6. These numbers were used to calculate the visible cross section (σ_{vis}), the reduced cross section ($\tilde{\sigma}_{vis}$) and finally the charm structure function ($F_{2,\mathrm{data}}^{c\bar{c}}$).

The studies to systematic effects on the cross section measurement were also performed for these 20 kinematic regions. The results of these studies are given in detail in appendix A. The conclusion is that there are no surprises compared to the inclusive production cross section results (Sec. 6.3).

6.6.3. Results on the reduced cross section and $\mathrm{F}_2^{c\bar{c}}$

Table 6.6 gives in addition to the 'raw' numbers also the visible cross section and the error on the calculated cross section.

From the cross sections the reduced cross section and the structure function $\mathrm{F}_2^{c\bar{c}}$ are extracted. The results of this are given in Tab. 6.7. The theoretical prediction for the visible cross section (from HVQDIS) and the structure function are given in the last three columns. The kinematic bin definitions are given by columns 4 through 7, while the structure function was 'unfolded' at the kinematic point given by the columns two and three.

Another, more elegant, way to represent the $\mathrm{F}_2^{c\bar{c}}$ results is by plotting them in bins of fixed values of Q^2. This is done in Fig. 6.6, where the results are compared to the pQCD prediction of the ZEUS94 PDFs. The structure function shows a clear rise with increasing Q^2 and decreasing x which is also followed by the NLO-pQCD results from ZEUS.

When the results are plotted for fixed values of x as a function of Q^2 the scaling violations, due to the gluon contribution to the structure of the proton, become clearly visible (Fig. 6.7). For this figure the cross section were unfolded at different x-values compared to Tab. 6.7. The results are again compared to the ZEUS NLO-pQCD fits. The data seem to require a faster rise of the structure function as a function of Q^2, which in terms of parton density functions would mean a higher or harder gluonic content for the proton.

6.6.4. Comparison to D^* results

As the D^* analysis focuses on one single decay chain, but also, and perhaps more importantly, as the exact selection criteria for the two analyses select different regions of phase space, it is hard to compare the (differential) production cross sections. The charm structure function, which is assumed to be a universal property of the proton, on the other hand can be used to directly compare the charm results. This is done in Fig. 6.8, where the ratio $F_2^{c\bar{c}}/F_2$ is shown, effectively the contribution of charm to the total proton structure. This analysis and the published ZEUS D^* results for the same dataset [70] agree. The H1 D^* results complete the charm data from the 1996-1997 running period and agrees with the two ZEUS analyses. This figure also demonstrates that charm contributes a substantial part of the proton for increasing

Table 6.6: *An overview of the electron signal composition and selection efficiencies for the 20 bins of the double differential cross section measurement. The statistical errors on the numbers have been omitted for clarity of the table.*

	BIN		EXPERIMENTAL RESULTS											
												Uncertainty		
#	Q^2 GeV^2	x 10^{-4}	N_{ele}	N_{con}	N_{pro}	N_{dal}	N_{bea}	N_{SLe}	ϵ_{DIS}	ϵ_{SLe}	σ_{vis} (pb)	stat.	+syst.	-syst.
1	2.5	3.1	72.1	51.4	5.8	2.6	0.0	12.3	0.041	0.812	11.32	17.19	5.21	4.72
2	2.5	0.7	139.4	71.4	11.2	4.9	0.6	51.4	0.041	0.752	50.78	23.50	9.68	5.81
3	6.5	9.6	119.7	74.3	9.6	4.6	0.2	31.0	0.097	0.811	12.04	8.80	3.70	4.15
4	6.5	3.4	254.6	82.2	20.4	6.9	1.1	144.0	0.124	0.785	44.91	8.76	2.09	6.49
5	6.5	1.4	290.4	86.7	23.2	8.9	4.6	166.9	0.155	0.709	46.30	8.30	2.26	5.69
6	12.0	15.6	301.1	163.2	24.1	9.6	1.0	103.2	0.280	0.793	14.16	4.62	1.11	1.65
7	12.0	6.5	246.9	90.8	19.8	7.7	3.6	125.0	0.297	0.787	16.28	3.74	0.81	1.29
8	12.0	2.7	429.5	114.6	34.4	13.8	13.6	253.2	0.395	0.714	27.32	3.92	1.95	2.59
9	20.0	31.6	361.2	220.3	28.9	14.2	2.9	94.9	0.640	0.820	5.51	2.21	0.94	0.35
10	20.0	10.8	743.4	284.6	59.5	22.9	17.6	358.7	0.732	0.772	19.33	2.62	1.33	1.10
11	20.0	4.4	454.5	146.5	36.4	16.3	17.4	238.0	0.642	0.736	15.34	2.41	1.03	1.38
12	32.5	51.3	556.6	275.5	44.5	19.9	6.4	210.3	1.041	0.764	8.05	1.64	0.49	0.75
13	32.5	17.5	693.0	288.7	55.4	25.1	22.8	300.9	0.913	0.770	13.04	2.10	0.75	1.22
14	32.5	7.2	338.5	121.1	27.1	14.3	18.8	157.2	0.647	0.666	11.10	2.37	1.23	1.44
15	55.0	35.8	649.7	250.5	52.0	25.3	14.6	307.3	0.931	0.763	13.17	1.92	0.79	1.36
16	55.0	13.5	679.6	280.9	54.4	25.7	27.2	291.4	0.752	0.697	16.92	2.68	1.42	1.84
17	100.0	65.0	403.9	154.1	32.3	20.0	10.1	187.5	0.982	0.662	8.79	1.63	1.03	0.91
18	100.0	23.6	432.7	156.0	34.6	22.7	19.2	200.2	0.686	0.611	14.53	2.63	2.13	1.75
19	565.0	283.9	358.9	126.5	28.7	36.0	13.4	154.2	0.837	0.552	10.17	2.03	0.75	1.55
20	565.0	124.9	237.9	87.4	19.0	30.3	13.7	87.5	0.594	0.477	9.41	2.80	2.86	2.25

Table 6.7: *The semileptonic cross section in 20 bins of $y - Q^2$ and its derivatives.*

Bin							Data				Theory		
#	$Q^2{}_{Unf.}$ (GeV^2)	$x_{Unf.}$ (10^{-4})	$Q^2_{\min}$ (GeV^2)	$Q^2_{\max}$ (GeV^2)	$y_{\min}$	$y_{\max}$	σ_{vis} (pb)	$\frac{d^2\sigma^{vis}}{dQ^2dx}$ (pb/GeV^2)	$\tilde{\sigma}_{vis}$ (10^{-3})	$F_2^{c\bar{c}}$	σ_{vis} (pb)	$\tilde{\sigma}_{vis}$ (10^{-3})	$F_2^{c\bar{c}}$
1	2.5	3.070	2	4	0.03	0.15	11.32	$6.404 \cdot 10^3$	0.05161	0.01543	41.15	0.1875	0.05607
2	2.5	0.6502	2	4	0.15	0.70	50.78	$1.462 \cdot 10^5$	0.3428	0.06586	66.95	0.4520	0.08684
3	6.5	9.579	4	9	0.03	0.12	12.04	$1.341 \cdot 10^3$	0.2246	0.03652	32.37	0.6037	0.09816
4	6.5	3.432	4	9	0.12	0.30	44.91	$2.501 \cdot 10^4$	1.713	0.1430	43.22	1.649	0.1376
5	6.5	1.437	4	9	0.30	0.70	46.30	$6.767 \cdot 10^4$	2.524	0.2541	32.62	1.778	0.1790
6	12.0	15.60	9	15	0.03	0.14	14.16	$6.792 \cdot 10^2$	0.6377	0.09405	20.58	0.9269	0.1367
7	12.0	6.470	9	15	0.14	0.27	16.28	$5.948 \cdot 10^3$	2.608	0.1769	17.20	2.756	0.1870
8	12.0	2.723	9	15	0.27	0.70	27.32	$1.509 \cdot 10^4$	3.597	0.3497	19.33	2.546	0.2475
9	20.0	31.58	15	25	0.03	0.11	5.508	$1.028 \cdot 10^2$	0.5347	0.06113	13.02	1.264	0.1445
10	20.0	10.78	15	25	0.11	0.30	19.33	$1.519 \cdot 10^3$	3.081	0.2061	20.67	3.295	0.2204
11	20.0	4.420	15	25	0.30	0.70	15.34	$3.643 \cdot 10^3$	3.957	0.3379	13.73	3.541	0.3024
12	32.5	51.32	25	40	0.03	0.11	8.049	$6.162 \cdot 10^1$	1.375	0.1368	8.840	1.511	0.1502
13	32.5	17.52	25	40	0.11	0.30	13.04	$4.202 \cdot 10^2$	3.659	0.2056	15.32	4.300	0.2416
14	32.5	7.184	25	40	0.30	0.70	11.10	$1.082 \cdot 10^3$	5.044	0.3916	9.645	4.381	0.3401
15	55.0	35.76	40	70	0.06	0.20	13.17	$6.192 \cdot 10^1$	3.045	0.2464	12.09	2.795	0.2261
16	55.0	13.50	40	70	0.20	0.70	16.92	$2.598 \cdot 10^2$	6.256	0.3903	14.97	5.535	0.3453
17	100.0	65.02	70	130	0.06	0.20	8.787	$1.136 \cdot 10^1$	3.358	0.2439	7.435	2.841	0.2064
18	100.0	24.56	70	130	0.20	0.70	14.53	$6.137 \cdot 10^1$	8.886	0.4467	10.86	6.640	0.3338
19	565.0	283.9	130	1000	0.06	0.30	10.17	$1.072 \cdot 10^{-1}$	4.637	0.1403	7.255	3.309	0.1001
20	565.0	124.9	130	1000	0.30	0.70	9.412	$3.192 \cdot 10^{-1}$	7.818	0.2580	7.115	5.910	0.1950

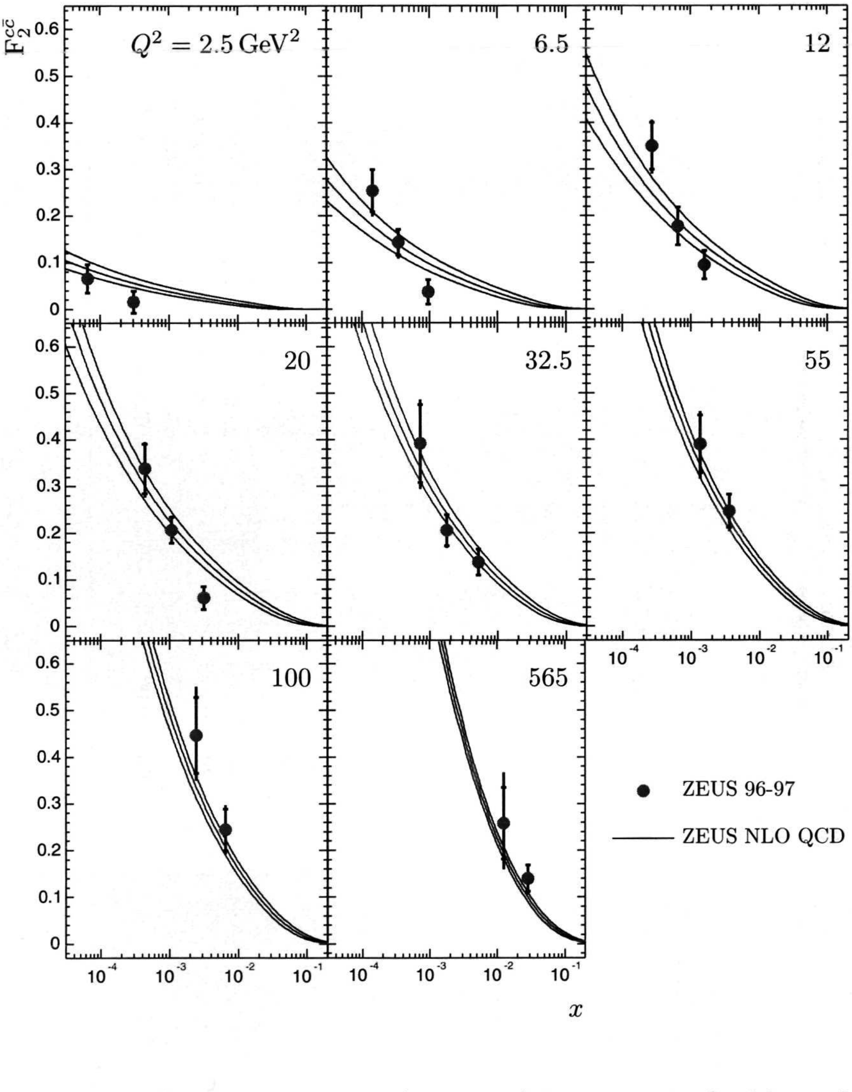

Figure 6.6: *The charm structure function of the proton in fixed bins of Q^2 as a function of x. The data are compared to the ZEUS NLO-pQCD fit results of the inclusive F_2 measurement.*

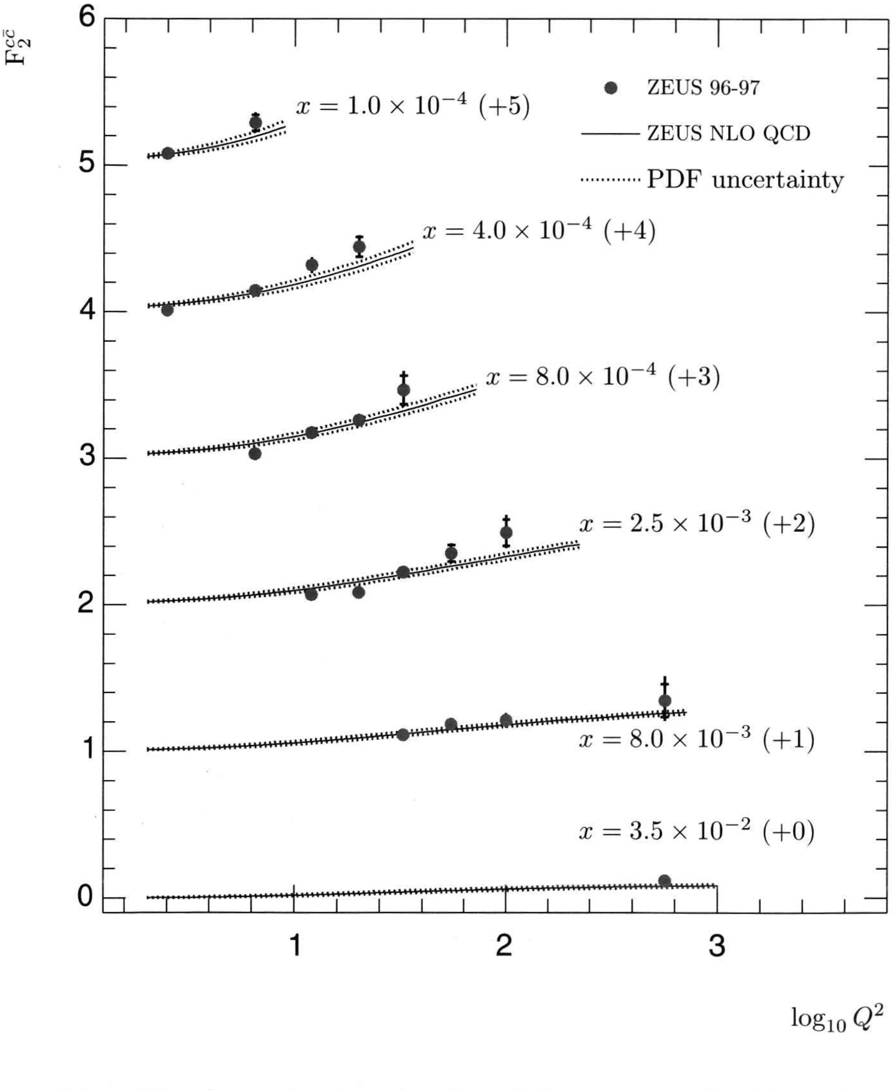

Figure 6.7: *The charm structure function of the proton in fixed bins of x as a function of Q^2. The data are again compared to the ZEUS NLO-pQCD fit results.*

Q^2, rising to approximately 35% of the total proton structure for $x \approx 10^{-5}$ at $Q^2 \gtrsim 100$ GeV^2.

6.7. Summary

In this chapter the transformation of the found number of electrons, to cross sections and derivatives thereof has been discussed. The selection efficiencies have been treated in detail. The event selection efficiency increases with Q^2, due to the adopted strategy of the third level trigger. The semileptonic electron tagging efficiency was found to be flat, both as a function of momentum and of polar angle, which together define the visible phase space of the decay electron. An overview was given of the studies to systematic effects that might bias the final results. These effects have been quantified and are treated as a source of uncertainty on the final results. The visible production cross section was presented and compared to predictions of the NLO-pQCD programme HVQDIS, for several choices of the input parameters. The single differential visible cross sections in Q^2, x and W of the event and p_T and η of the electron were shown. These results were compared to predictions of HVQDIS, with the ZEUS94 PDFs, $m_c = 1.3$ GeV and the standard Peterson fragmentation function. Overall agreement was found, but for the $d\sigma/dW$ distribution. This distribution seems to be shifted compared to the theoretical prediction. For the moment, this remains a puzzle unsolved. The double differential cross section in Q^2 and x was used to extract the charm structure function $F_2^{c\bar{c}}$. The data agree with the current PDFs.

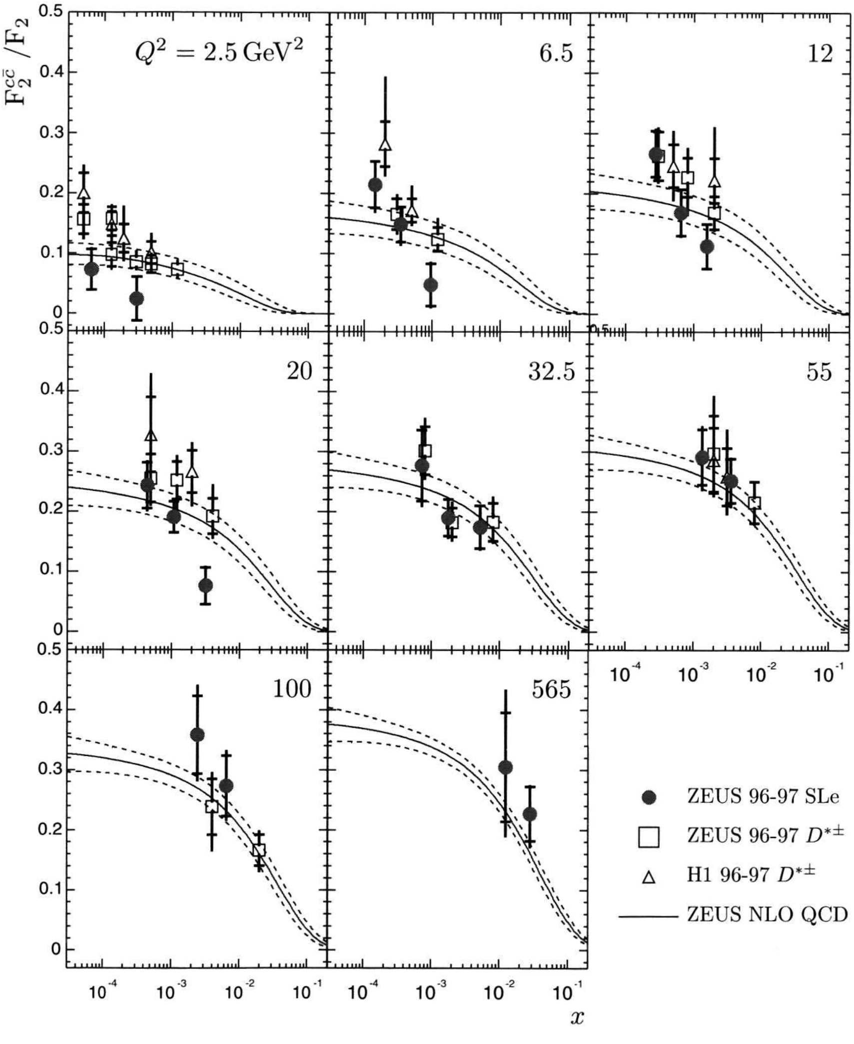

Figure 6.8: *A direct comparison between published D^* results (ZEUS - squares, H1 - triangles) and this analysis. The contribution of charm to the total proton structure is shown in fixed bins of Q^2 as a function of x. The top-most label indicates the Q^2 of the given bin. These data are plotted as published, without re-unfolding to the central Q^2 values of this analysis.*

CHAPTER 7

NLO Fits on the charm production cross section

In this chapter fits of the charm quark mass, m_c, the Peterson and the Kartvelishvili fragmentation functions are described. First there will be a short discussion about the goal of the fits. The available experimental data are described which is followed by an outline of the fit strategy. Results of one and two dimensional fits are presented and discussed.

7.1. Goal of the fits

The motivation for the fits presented in this chapter will be outlined in this section. A terse description will be given on what the current methods are to obtain knowledge on the charm quark mass. It will be argued why NLO-pQCD fits of the charm quark mass cannot be done without taking into account fragmentation. This will lay the basis for the work described in the remainder of this chapter.

7.1.1. Mass of the charm quark

The mass of the charm quark is one of the 19 free parameters of the Standard Model. As a consequence, there is the need to know its value with as much accuracy as possible. As free quarks have not been detected the only way to extract the charm quark mass is indirectly. The traditional method has been to extract it from the well known charm-meson masses. One approach uses the quark binding potential obtained from Heavy Quark Effective Theory (HQET) to extract the charm quark mass from D-mesons. Unfortunately this is hampered by the relative lightness of the charm quark. Using non-relativistic QCD the mass can be extracted from the spectrum of the J/Ψ and the higher bound $c\bar{c}$ states.

An alternative to using effective theories is found in lattice-gauge calculations where again the mass of charmed mesons is determined. This method suffers from

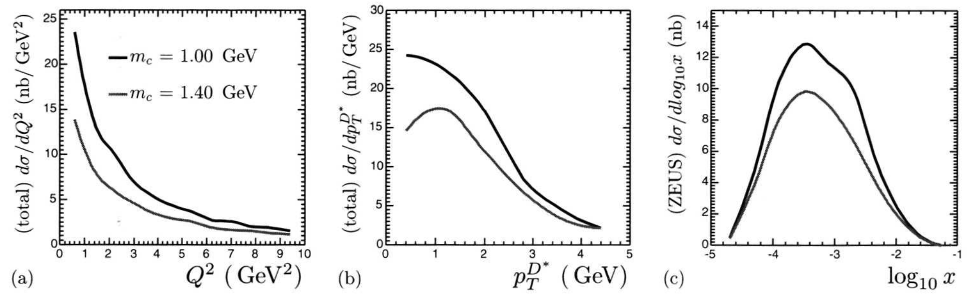

Figure 7.1: *Differential cross section calculations for open* $D^{*\pm}$ *production at HERA by* Hvqdis *for CTEQ6 and* $\epsilon_P = 0.035$*. (a) the total production cross section differential in* Q^2 *and (b) differential in* $p_T(D^*)$*. (c) The visible production cross section for the ZEUS data, differential in* x*. The upper (lower) curve shows the calculation for* m_c *= 1 (1.4) GeV.*

the fact that the charm quark mass is so high that it is sensitive to so-called *lattice artifacts*: effects of choices related to the size and spacing of the lattice [33].

These extraction methods have been the subject of detailed studies over the past years, revealing the mentioned difficulties when extracting the mass of the lightest heavy quark. Especially for the lattice-gauge calculations it is true that new insights in the difficulties have been obtained in recent years. This is reflected in the fact that the Particle Data Group has increased its estimate of the uncertainty on the mass between the 1998 [72] and 2002 [33] editions of the Review of Particle Physics by 33%, to $1.0 < m_c < 1.4\,\mathrm{GeV}$ (was $1.1 < m_c < 1.4\,\mathrm{GeV}$).

With the advent of more precise charm-production data from the HERA experiments a fourth method becomes available. As shown in chapter 1, the role of the charm quark mass in the charm production cross sections is most pronounced in the fact that the cross section rises with a falling charm quark mass and *vice versa* as shown in Fig. 7.1. The effect of the uncertainty on the charm quark mass is always treated as an uncertainty on the cross section calculation, but actually it provides a window of opportunity for determining m_c.

7.1.2. Fragmentation functions

Fragmentation functions are extremely important in building the bridge between the hard QCD interaction and the experimental reality. Furthermore, the Peterson function has an implicit correlation with the quark mass: $\epsilon_P \sim 1/m_Q$. When extracting the charm quark mass from the visible cross section this cannot be overlooked. Apart from this (direct) argument, there is the additional effect of the kinematic cuts applied on the charm-originating particles (D^*,e^-). Variations in the kinematics of the produced mesons directly affect the predicted visible cross sections. This mainly manifests itself in terms of normalisation but additionally it can also directly influence the shape of differential cross sections. Examples hereof are the $d\sigma/dp_T$ and $d\sigma/d\eta$ cross sections.

Figure 7.2: *The ARGUS and CLEO measurements of the D^0 and D^{*+} cross section as a function of z'. These data were obtained in e^+e^- annihilation at $\sqrt{s} \approx 10$ GeV. The Peterson functions have been fitted to the two D-mesons separately, but with the data sets combined.*

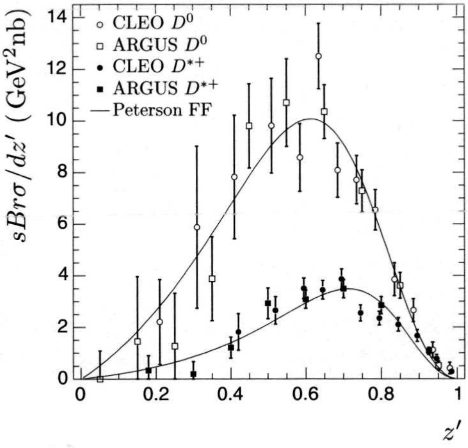

This leads to the conclusion that, when extracting the charm quark mass from differential production cross sections, this must be done in conjunction with tuning of the fragmentation functions. And in fact, doing so has two main advantages. First, it decreases the (fragmentation) model dependence of the extracted charm quark mass. Second, it gives rise to a novel way to extract information about the heavy quark fragmentation.

Traditionally fragmentation functions are tuned by fitting them to cross sections differential in a parameter z', where z' is an approximation of the fragmentation function z, the fraction of the transfered light cone momentum (Ch. 2). Typical examples are $z' = p/p_{max}$, used by ARGUS [73], and $z' = (E+p)/(E+p)_{max}$, used by CLEO [74] to extract ϵ_P for D^0 and $D^{*\pm}$ production. These measurements and the resulting Peterson function are shown in Fig. 7.2. Though the parameter z' is related to the fragmentation z it is not quite the same. This makes the interpretation of the obtained fragmentation parameter less clear.

7.2. The available datasets

$D^{*\pm}$-data

The straightforward nature of the $D^{*\pm}$-final state compared to the semileptonic state (see Ch. 2) makes it an excellent working ground for pioneering fits on both the mass and the fragmentation function. Both the ZEUS and H1 collaborations have published results on the inclusive production of $D^{*\pm}(2010)$ [70, 71]. The data used in these fits cover the 1996-1997 running period. The two collaborations have measured the differential production cross sections in slightly different regions of phase space. This is mainly due to the respective designs of the two experiments. The kinematic characteristics of the two data sets are given on the left hand side in Tab. 7.1.

Both experiments reported single differential production cross sections as a function of Q^2, x_{BJ} and W of the event and p_T and η of the D^*. Additionally, ZEUS has published a cross section differential in $x(D^*) = 2|\vec{p}^*(D^*)|/W$, with $\vec{p}^*$ the

Table 7.1: *Kinematic range of the measured D^* (left) and semileptonic (right) cross sections measured by ZEUS and H1.*

$D^{*\pm}$-Variable	ZEUS-$D^{*\pm}$	H1-$D^{*\pm}$	ZEUS-SLe	SLe-variable
Q^2_{MIN} (GeV^2)	1	1	2	
Q^2_{MAX} (GeV^2)	600	100	1000	
y_{MIN}	0.02	0.05	0.03	
y_{MAX}	0.70	0.70	0.70	
$P^{D^*}_{T,MIN}$ (GeV)	1.5	1.5	1.2	p^{SLe}_{MIN} (GeV)
$P^{D^*}_{T,MAX}$ (GeV)	15	inf	5.0	p^{SLe}_{MAX} (GeV)
$\lvert\eta^{D^*}_{MAX}\rvert$	1.5	1.5	0.65	θ^{SLe}_{MIN} (rad)
			2.50	θ^{SLe}_{MAX} (rad)

spatial vector of the D^* in the γp center of mass frame, and H1 a $d\sigma/dz$, where $z = (E - p_z)_{D^*}/2yE_e$. All these results include a statistical and a systematic uncertainty estimation from which a total error was derived by adding them in quadrature.

The semileptonic data

The semileptonic data presented in the previous chapter will be fitted separately and the result will be combined with the $D^{*\pm}$ data to yield a combined result for the simultaneous extraction of both m_c and ϵ_P. For completeness, the kinematic range covered by this data is given on the right hand side in Tab. 7.1.

7.3. Fit strategy

To investigate the parameter space for m_c and ϵ_P initially one parameter will be fixed while the other is determined. The results of these fits are the input of a second round of fits to estimate the minimum of a combined fit. Additionally, this allows a proof of concept and the investigation of the behaviour of the χ^2 shape in a more controlled setting.

In this simple setting, the use of the Peterson fragmentation function is compared to that of the Kartvelishvili form. The fit of the Kartvelishvili fragmentation function will be done with the best-fit value of the charm quark mass of the first round of fits. This ensures that it can be directly compared with the result of the second fit of the Peterson function.

The knowledge obtained from this exercise will be applied in the simultaneous extraction of both the charm quark mass and ϵ_P. Apart from determining the statistical uncertainty of these two dimensional fits, there will also be an assessment of the effect of systematic choices involved in these fits on the obtained results.

The calculation of a full set of cross sections for one configuration of parameters by HVQDIS is rather time consuming. Depending on the machine and parameter configuration it can take between 8 hours and 2 days. As a result it is not feasible to do a (MINUIT-like) steepest descent parameter fit. Therefore, instead of scanning the parameter space with decreasing step sizes as the χ^2-minimum is approached, it is binned equidistantly and the visible cross sections are calculated *a priori*. The χ^2-values are calculated in each bin. The χ^2-function can be obtained by fitting a function to these χ^2-values. Using this analytical function a steepest descent search can be applied to find the best-fit value of the parameter. The obtained best-fit parameter value can be determined with an accuracy better than the parameter bin size, due to the fact that the χ^2-function is well over-constrained on a relative large interval. An additional benefit of this approach is the greatly reduced sensitivity to statistical fluctuations in the calculated visible cross sections (see Ch. 2).

7.4. Fixed choices for all fits

The charm quark mass and the fragmentation function are not the only parameters in the calculation as done by the HVQDIS programme. The other, fixed, settings are given here.

Parton density function

In figure 7.3 the results of using CTEQ6 are compared to distributions obtained using the CTEQ5F3 PDF, which is a true fixed-three-flavour set. Both PDFs yield very similar results for the total cross section distributions. The CTEQ6 PDF have been extracted from data sets that include the latest (high precision) results on structure functions from HERA and the high-E_T jets data from the Tevatron. This is more likely to account for the small differences than the use of a not VFNS for the PDF extraction. In addition the CTEQ6 set has the added bonus that the FORTRAN implementation of the PDFs has a faster interface to the results, compared to the CTEQ5 set. In principle other PDFs (GRV98, ZEUS94) are also available, but those are all (a lot) older than CTEQ6, and none included the aforementioned new datasets. Therefore, CTEQ6 was chosen as basis for the fits.

Renormalisation and factorisation scale

Past analysis of HVQDIS results have given insight in the effect of the scales for renormalisation and factorisation, which for HVQDIS are set to be equal. The most detailed description of such an analysis can be found in the work from the author of the programme [39]. The conclusion of such studies is invariantly that the choice of the exact definition of the scale has only a small effect ($\approx 2\%$). As HVQDIS offers the option to choose from many different scale-definitions, which all are equally valid, the choice was made to use to the scale-definition as used in the calculation for the ZEUS $D^{*\pm}$ publication [70]: $\mu = \sqrt{Q^2 + m_c^2}$.

Hadronisation fraction $c \to D^{*\pm}$

The hadronisation fraction is effectively a normalisation parameter for the theory distributions. It is applied after the pQCD calculation as a global scale. In the ZEUS-D^* publication a value of 0.222 ± 0.020 is used. The current PDG only quotes the DELPHI result $f(c \to D^{*+}) = 0.255 \pm 0.017$ [33]. However, combined results of all

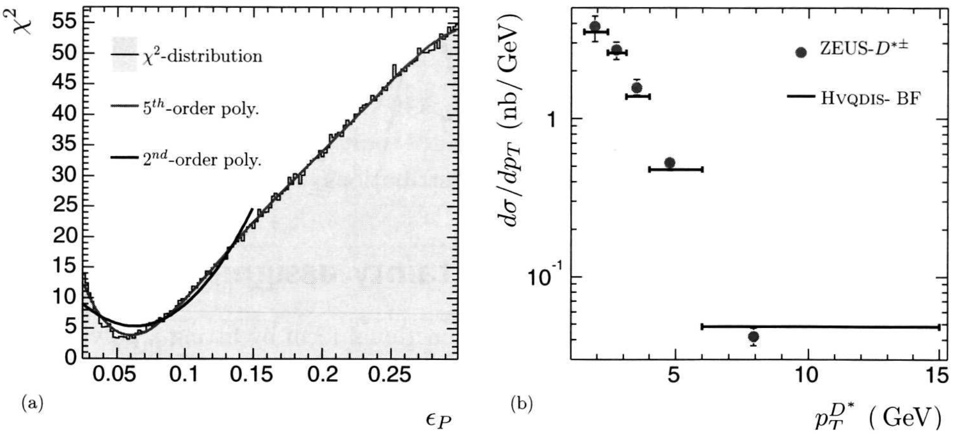

Figure 7.4: *(a) The χ^2-distribution of the ZEUS-p_T cross section for the fits of the Peterson fragmentation function with $m_c = 1.30$ GeV. The fifth order polynomial, used to obtain the best-fit value is also shown. A fit on a limited range of a parabola shows that this functional form cannot describe the underlying χ^2-distribution. (b) A comparison between the data (dots) and the best-fit* HVQDIS*-distribution.*

When the best fit values for the individual differential cross sections are listed the σ_{stat} will be quoted. The best fit values will be given with the two uncertainties separately, following $\mu_{\rm BF} \pm \sigma_{\rm BF} \pm \sigma_{\rm spread}$.

7.7.3. Results from the fits

In all, five sets of fits were performed: two on ϵ_P, two on m_c and one on the Kartvelishvili fragmentation model. The first fits for both ϵ_P and m_c were based on a reasonable prior assumption for the other variable. For the second fit the other parameter was fixed to the result of the first fit. This way correlations between optimal values of m_c and ϵ_P are probed.

Charm quark mass fit for $\epsilon_P = 0.035$

The fit range for m_c was fixed to $m_c \in [1.0\,\text{GeV}, 2.0\,\text{GeV}]$ with $\Delta m_c = 0.01$ GeV. In appendix C, Fig. C.1 the χ^2-distributions of the individual differential cross sections and the combined result are shown. The best-fit values from these χ^2-distributions are given in Tab. 7.2 and shown in Fig. 7.5. The statistical uncertainty on the best fit value is ≈ 3 times larger than the initial grid spacing. The result is in good agreement with the PDF value of $m_c = 1.0$ - 1.4 GeV.

Peterson fragmentation fit for $m_c = 1.30$ GeV

To fit the Peterson fragmentation function a grid was spanned for ϵ_P with $\epsilon_P \in [0.024, 0.300]$ and $\Delta\epsilon_P = 0.002$. The χ^2 distributions are shown in Fig C.4 and the

Table 7.2: *The charm quark mass fit results, with Peterson fragmentation ($\epsilon_P = 0.035$)*

Experiment	$d\sigma/dY$	best fit	$+1\sigma$	-1σ	χ^2/dof
ZEUS	$p_T(D^*)$	1.384	0.101	0.093	7.1/4
	$\eta(D^*)$	1.342	0.084	0.078	3.7/5
	$x(D^*)$	1.389	0.083	0.075	4.6/5
	$\log_{10}(Q^2)$	1.251	0.088	0.084	1.8/6
	$\log_{10}(x)$	1.314	0.084	0.080	1.7/4
	W	1.318	0.088	0.082	1.8/5
H1	$p_T(D^*)$	1.25	0.11	0.11	5.2/4
	$\eta(D^*)$	1.15	0.12	0.12	1.4/3
	$z(D^*)$	1.31	0.13	0.11	11.8/6
	$\log_{10}(Q^2)$	1.22	0.13	0.11	1.8/5
	$\log_{10}(x)$	1.14	0.12	0.11	0.4/3
	W	1.17	0.13	0.12	1.1/3
combined	(best fit)	1.297	0.028	0.027	50.3/53
	(spread)		0.087	0.087	

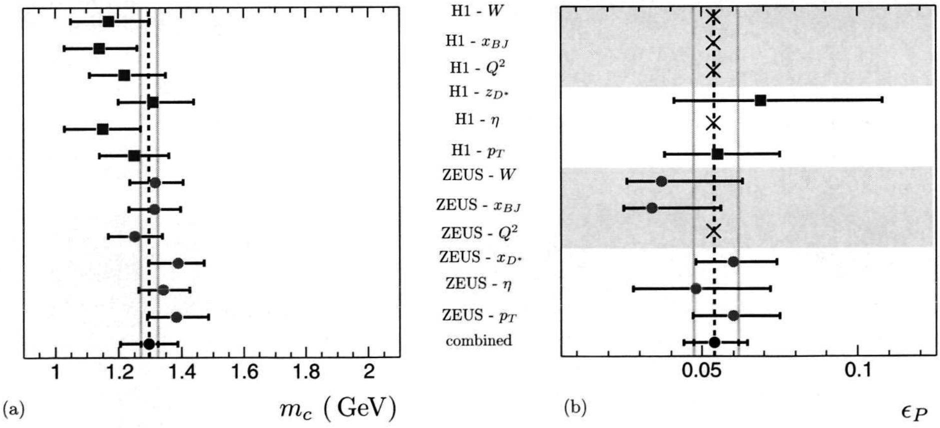

Figure 7.5: *The individual and combined results of (a) the charm quark mass fit, for ϵ_P = 0.035 and (b) the ϵ_P fit with m_c = 1.30 GeV compared. The distributions that were not used to obtain the combined ϵ_P result are marked by the coloured background.*

Table 7.3: *The results for ϵ_P with $m_c = 1.3\,GeV$. The distributions marked with an * have been used to obtain the combined result.*

Experiment		$d\sigma/dY$	best fit	$+1\sigma$	-1σ	χ^2/dof
ZEUS	*	$p_T(D^*)$	0.060	0.015	0.013	3.8/4
	*	$\eta(D^*)$	0.048	0.024	0.020	3.7/5
	*	$x(D^*)$	0.060	0.014	0.012	1.8/5
		$\log_{10}(Q^2)$	-	-	-	-
		$\log_{10}(x)$	0.034	0.022	0.009	1.7/4
		W	0.037	0.026	0.011	1.9/5
H1	*	$p_T(D^*)$	0.055	0.020	0.017	4.0/4
	*	$\eta(D^*)$	-	-	-	-
	*	$z(D^*)$	0.069	0.039	0.028	10.5/6
		$\log_{10}(Q^2)$	-	-	-	-
		$\log_{10}(x)$	-	-	-	-
		W	-	-	-	-
combined		(best fit)	0.054	0.0076	0.0067	29.2/28
		(spread)		0.0074	0.0074	

results are summarised in Tab. 7.3 and Fig. 7.5. To obtain the combined results only those distributions that have a direct measure of the D^*-fragmentation are used: $d\sigma/dp_T^{D*}$, $d\sigma/d\eta^{D*}$ and $d\sigma/dx^{D*}$ or $d\sigma/dz^{D*}$.

The first thing that stands out is that the H1 *global* (Q^2,x_{BJ},W) differential distributions have no minimum on the scanned interval and likewise for the ZEUS-Q^2.

The distributions that represent the D^*-final state (p_T,η,$x(D^*)$ and $z(D^*)$) give results that are very compatible, with the only exception being the H1-η distribution, which has no minimum on the probed interval for $m_c = 1.3\,\text{GeV}$. The χ^2-distribution of this cross section was nonetheless combined with the other D^*-specific distributions for the determination of the combined result.

Continuation of the unfolding

The charm quark mass and the Peterson fragmentation function are now fixed to the fit results in order to determine the other parameter in a new fit. The procedure for these fits is identical to the ones presented in the previous sections. Therefore only the results will be given here. The individual results for fit on m_c (ϵ_P) are given in table 7.4 (7.5). The results are also given in Fig. 7.6. The H1 cross sections typically give a lower mass as best-fit result than the ZEUS cross sections. This systematic difference between the result of the two experiments is however well within the respective quoted uncertainties on the luminosity, which is 2%.

The second fit of the charm quark mass, though within the combined error of the first fit result, has moved significantly. The ϵ_P result remains for all practical purposes the same. This last comes as no surprise as the input charm quark mass only changed by $\approx 1\%$. Both results have an improved χ^2/dof with respect to the initial fits in common. To conclude, the chain of (combined) results are given in

Table 7.4: *The charm quark mass fit results, with Peterson fragmentation ($\epsilon_P = 0.054$)*

Experiment	$d\sigma/dY$	best fit	$+1\sigma$	-1σ	χ^2/dof
ZEUS	$p_T(D^*)$	1.245	0.100	0.094	3.3/4
	$\eta(D^*)$	1.259	0.086	0.081	3.4/5
	$x(D^*)$	1.259	0.083	0.080	1.1/5
	$\log_{10}(Q^2)$	1.168	0.094	0.088	2.0/6
	$\log_{10}(x)$	1.234	0.086	0.082	1.1/4
	W	1.242	0.090	0.085	1.8/5
H1	$p_T(D^*)$	1.15	0.11	0.10	2.0/4
	$\eta(D^*)$	1.072	0.122	0.076†	1.2/3
	$z(D^*)$	1.23	0.13	0.12	10.3/6
	$\log_{10}(Q^2)$	1.13	0.14	0.13	1.8/5
	$\log_{10}(x)$	1.062	0.117	0.067†	0.4/3
	W	1.079	0.144	0.084†	1.2/3
combined	(best fit)	1.201	0.028	0.029	36.1/53
	(spread)		0.077	0.077	

† These uncertainties are truncated to not exceed the lower edge of the fit interval. Therefore they appear smaller than what they should be.

Table 7.5: *The result for ϵ_P with $m_c = 1.29$ GeV. The distributions marked with an * have been used to obtain the combined result.*

Experiment		$d\sigma/dY$	best fit	$+1\sigma$	-1σ	χ^2/dof
ZEUS	*	$p_T(D^*)$	0.057	0.013	0.011	3.5/4
	*	$\eta(D^*)$	0.047	0.022	0.017	3.5/5
	*	$x(D^*)$	0.056	0.013	0.010	1.2/5
		$\log_{10}(Q^2)$	-	-	-	-
		$\log_{10}(x)$	0.038	0.020	0.012	1.7/4
		W	0.041	0.023	0.015	1.8/5
H1	*	$p_T(D^*)$	0.054	0.019	0.015	3.8/4
	*	$\eta(D^*)$	-	-	-	-
	*	$z(D^*)$	0.062	0.044	0.023	10.4/6
		$\log_{10}(Q^2)$	-	-	-	-
		$\log_{10}(x)$	-	-	-	-
		W	-	-	-	-
combined		(best fit)	0.054	0.007	0.006	27.1/28
		(spread)		0.005	0.005	

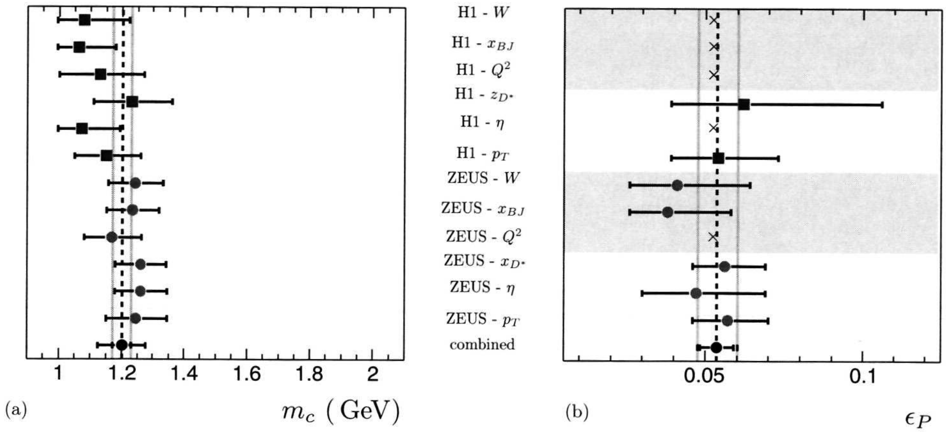

Figure 7.6: *The individual and combined results of (a) the charm quark mass fit, for ϵ_P = 0.054 and (b) the ϵ_P fit with m_c = 1.29 GeV compared. The distributions that were not used to obtain the combined ϵ_P result are marked by the coloured background.*

Table 7.6: *The results of the two rounds of fits.*

	initial	**first fit**	**second fit**
m_c (GeV)	1.3	$1.297 \pm^{0.028}_{0.027} \pm^{0.087}_{0.087}$	$1.201 \pm^{0.029}_{0.029} \pm^{0.077}_{0.077}$
ϵ_P	0.035	$0.054 \pm^{0.0076}_{0.0076} \pm^{0.0074}_{0.0074}$	$0.054 \pm^{0.0066}_{0.0060} \pm^{0.0053}_{0.0053}$

Tab. 7.6.

Fits of the Kartvelishvili fragmentation function

The Kartvelishvili fragmentation function has been successfully fitted on beauty production data at SLD [76]. The parameter α_K was determined to be 3.904 ± 0.072. In principle charm fragmentation is softer, so the expected value for charm should be (slightly) below this value. Based on these considerations the following interval of investigation was defined: $\alpha_K \in [1., 5.]$ with $\Delta\alpha_K = 0.05$. For these fits the charm quark mass was fixed to $m_c = 1.30$ GeV, based on the results from the ϵ_P/m_c fits. As for the fits of ϵ_P, the fits were restricted to those distributions that are directly sensitive to the heavy quark fragmentation. The χ^2 distributions of these fits and the accumulative result are shown in Fig. C.5. The results are summarised in Tab. 7.7. The combined result of $\alpha_K = 3.34$ is in good agreement with the initial assessment of the authors, whom assessed it to be $\alpha_K \approx 3$ [37].

7.7.4. Comparison of fragmentation functions

In Fig. 7.7 the Peterson and Kartvelishvili fragmentation functions are compared, with the parameters fixed to the fit results. The Kartvelishvili function with $\alpha_K =$

Table 7.7: *The results of the fit of α_K, for $m_c = 1.3$ GeV.*

Experiment		$d\sigma/dY$	**best fit**	$+1\sigma$	-1σ	χ^2**/dof**
ZEUS	$*$	$p_T(D^*)$	3.21	0.39	0.36	3.7/4
	$*$	$\eta(D^*)$	3.48	0.82	0.61	3.6/5
	$*$	$x(D^*)$	3.20	0.41	0.37	2.5/5
		$\log_{10}(Q^2)$	4.56	0.47	0.93	1.8/6
		$\log_{10}(x)$	3.90	0.91	0.70	1.7/4
		W	3.82	0.94	0.74	1.7/5
H1	$*$	$p_T(D^*)$	3.37	0.59	0.50	3.7/4
	$*$	$\eta(D^*)$	4.82	0.20†	0.91	1.9/3
	$*$	$z(D^*)$	3.05	0.92	0.71	9.8/6
		$\log_{10}(Q^2)$	4.82	0.20†	1.36	1.8/5
		$\log_{10}(x)$	4.82	0.20†	0.81	1.0/3
		W	4.82	0.20†	1.03	1.4/3
combined			3.34	0.22	0.21	28.3/28
		(spread)		0.62	0.62	

† These uncertainties are truncated to not exceed the upper edge of the fit interval. Therefore they appear smaller than what they should be.

Figure 7.7: *The Peterson (solid) and Kartvelishvili (dashed) fragmentation functions for the central values (thick line) and quoted the uncertainties (thin lines). All the distributions have been normalised individually.*

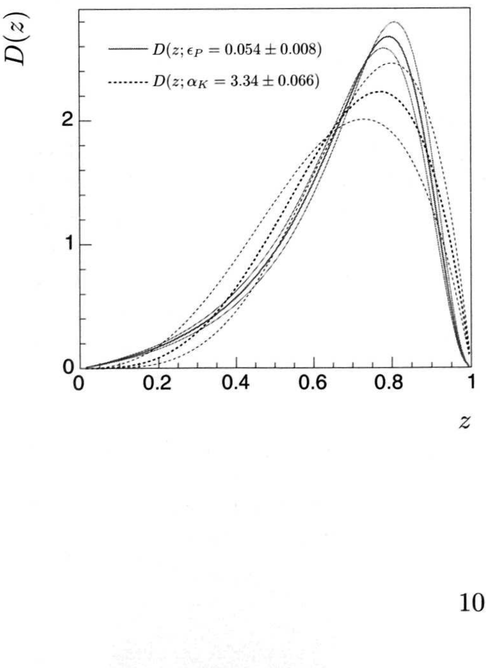

3.34 peaks at approximately the same value of z as the Peterson function with the best fit value for ϵ_P. The main difference lies in the fact that the Kartvelishvili function has a more pronounced tail on both sides of the peak. This is also reflected in that the peak yields a lower $D(z)$-value. The difference on the high end side is important as it directly effects the fraction of the cross section that is *a priori* visible.

7.8. Simultaneous extraction of two parameters

7.8.1. Parametrisation of the χ^2-distribution

In the two dimensional case the best-fit coordinate is found by locating the minimum of the χ^2-distribution, analogous to the one dimensional case. The two dimensional grid is defined within the ranges $x_{min} - x_{max}$ ($y_{min} - y_{max}$) for the first (second) varied parameter. Each point on this grid has an associated χ^2-value.

So, where the one dimensional case uses a (simple) fifth order polynomial, the two parameter case needs a more elaborate functional description. This is found in the completely correlated two dimensional polynomial of order two:

$$\begin{aligned}\chi^2(x,y) &= \alpha_1 x^2 y^2 + \alpha_2 x^2 y + \alpha_3 x^2 \\ &+\alpha_4 x y^2 + \alpha_5 y^2 \\ &+\alpha_6 x y + \alpha_7 x + \alpha_8 y + \alpha_9 \end{aligned} \tag{7.6}$$

Before the function is fitted to the χ^2 grid the parameters are initialised to some sensible values. The first assumption is that the correlations between the two quantities on the grid-axes are minimal, *i.e.*

$$\alpha_1 = 0, \quad \alpha_2 = 0, \quad \alpha_4 = 0, \quad \alpha_6 = 0$$

and the second assumption is that the grid dimensional was chosen such that the minimum lies approximately half-way of the available range and that the one sigma uncertainty touches the grid boundaries

$$\begin{aligned}\alpha_3 &= 4(x_{max}^2 - 2y_{max}y_{min} + y_{min}^2)^{-1} \\ \alpha_5 &= 4(y_{max}^2 - 2y_{max}y_{min} + y_{min}^2)^{-1} \\ \alpha_7 &= -\alpha_3(x_{max} + x_{min}) \\ \alpha_8 &= -\alpha_5(y_{max} + y_{min})\end{aligned}$$

And finally, the constant term is set to the average of the constants of the two independent parabola, which are assumed to yield $\chi^2 = 2$ at the minimum:

$$\alpha_9 = 2 - \tfrac{1}{2}(\alpha_3 x_{min}^2 + \alpha_7 x_{min} + \alpha_5 y_{min}^2 + \alpha_8 y_{min})$$

By initialising the parameters in this way a stable fit of the χ^2-distribution is ensured, where the correlation factors will not rampage to compensate one another on the grid domain.

7.8.2. Best fit value

Locating the global minimum within the grid domain is non-trivial. There is no analytical solution for a correlated polynomial of order two. To find the minimum, an adapted version of the bisection method is used in which a step in the x direction is followed by a step in the y direction. Both of these bisection procedures are treated independently, so the minimum in the x-coordinate can be found, for instance, while the y coordinate still needs to be determined. To verify that indeed the global minimum is found the following strategy is used. The bisection method can use any initial point as a starting point for its 'walk' towards the minimum, if indeed the function is monolithically falling towards the minimum. Therefore, by starting of in the four corners of the domain it can be verified that the found minimum is the global minimum.

7.8.3. Uncertainty assignment

The uncertainty for the two dimensional fit result is taken from the one dimensional case. The difference lies in that the uncertainty can not be given by a set of two 1σ deviation values, but rather as a closed curve on the two dimensional parameter plane. Points on the 1σ-contour must satisfy Eqn. 7.4.

In the ideal case, with only a linear correlation between the two parameters, this closed curve is given by an ellipse, with its focal point being the best fit value.

When the observables, m_c and ϵ_P, are linearly correlated the axes of the ellipse will not coincide with the axes spanned by the two parameters. Rather, the ellipse will be rotated in the m_c-ϵ_P plane. The relation between m_c-ϵ_P and the orthogonal basis of the problem is given by

$$\begin{pmatrix} \alpha \\ \beta \end{pmatrix} = \boldsymbol{R} \begin{pmatrix} m_c \\ \epsilon_P^2 \end{pmatrix} \tag{7.7}$$

where $\boldsymbol{R}$ is the unitary rotation matrix. The matrix $\boldsymbol{R}$ is purely defined by the rotation angle ϕ which is shown in Fig. 7.8. The one-sigma contour can now be used to directly extract the uncertainties on and the correlation between m_c and ϵ_P, following

$$\begin{pmatrix} \sigma_{m_c} & \sigma_{m_c/\epsilon_P^2} \\ \sigma_{m_c/\epsilon_P^2} & \sigma_{\epsilon_P^2} \end{pmatrix} = \boldsymbol{R} \begin{pmatrix} \sigma_\alpha & 0 \\ 0 & \sigma_\beta \end{pmatrix} \boldsymbol{R}^{-1} \tag{7.8}$$

with σ_α and σ_β as given in Fig. 7.8. This matrix will be given as the quantified numerical uncertainty, together with the extreme values of the two parameters on the contour. The quoted error on a single parameter will be based on the extremal values on the 1σ-contour.

7.8.4. Extraction of charm quark mass and Peterson fragmentation

Differences with the one dimensional fits

The simultaneous extraction of m_c and ϵ_P follows the same principles as outlined for the single parameter fits. The differences are summarised by the following.

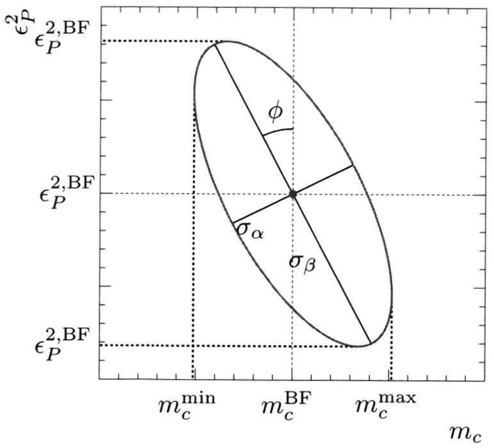

Figure 7.8: *An example of a 1σ-contour for two linearly correlated parameters. The rotation angle ϕ is denoted as well as the definitions of σ_α and σ_β.*

- To allow the use of a correlated 2-dimensional parabola shape for the χ^2-distribution not ϵ_P but rather ϵ_P^2 is fitted.

- The hadronisation fraction is taken to be $f(c \to D^{*+}) = 0.235$, following Gladilin. In the previous fits the value of $f(c \to D^{*+}) = 0.222$ was used, in accordance with the ZEUS publication on $D^{*\pm}$ production.

- The ZEUS x^{D^*} distribution is strongly correlated with its $P_T^{D^*}$ and η^{D^*} distributions. To exclude that such correlations bias the combined result, the first is not used in the two dimensional fits.

Results

The fits are based on a two dimensional grid in the m_c-ϵ_P^2-plane with 20 and 15 bins in the m_c and ϵ_P^2 direction, respectively. The fit ranges are taken as

$$1.00 \leq m_c \leq 1.95\,\mathrm{GeV}$$
$$0.0009 \leq \epsilon_P^2 \leq 0.0100$$

The results of these primary fits are given in Tab. 7.8. In figure 7.9 the χ^2-distribution, the best-fit point and the 1σ-contour are shown. In addition it shows the effect of varying the hadronisation fraction $f(c \to D^{*+})$ by one sigma. This is part of the systematic effects, treated in the next section.

On systematic effects

The charm quark mass and the value for ϵ_P are obtained by fixing several parameters. The correct form or value of these parameters is not known on forehand. The effect of these choices is investigated to get an idea of the systematic effect on the obtained results.

Table 7.8: *The best fit point of the combined two dimensional fit. The uncertainty has been quantified in terms of the extreme values on the* 1σ *contour and the covariance matrix. The best-fit value gave a* χ^2/dof *of 54/57.*

quantity	m_c (GeV)	ϵ_P^2	ϵ_P
best fit value	1.37	$6.66 \cdot 10^{-3}$	0.082
minimum on 1σ	1.33	$5.55 \cdot 10^{-3}$	0.075
maximum on 1σ	1.41	$7.68 \cdot 10^{-3}$	0.088

$$\begin{pmatrix} \sigma_{m_c} & \sigma_{m_c/\epsilon_P^2} \\ \sigma_{m_c/\epsilon_P^2} & \sigma_{\epsilon_P^2} \end{pmatrix} \qquad \begin{pmatrix} 0.033 & 5.24 \cdot 10^{-3} \\ 5.24 \cdot 10^{-3} & 1.11 \cdot 10^{-3} \end{pmatrix}$$

- Choice of input PDF
  In section 7.4 the CTEQ6 set was compared to the CTEQ5 set, which is, unlike the CTEQ6 PDFs, a Fixed Three Flavour parton density set. The effect was there shown to be of the order of a few percent, compatible with the intrinsic statistical accuracy of the HVQDIS calculations. Therefore, no uncertainty is attributed to this effect.

- Renormalisation and factorisation scale
  The choice of renormalisation and factorisation scales was also checked. Both scales were changed from the initial $\mu^2 = Q^2 + m_c^2$ to $\mu^2 = Q^2 + 4m_c^2$. The effect was also negligible.

- Hadronisation fraction $f(c \to D^{*+})$
  This constant directly affects the normalisation of the HVQDIS-calculated NLO-pQCD cross sections. The effect of varying the central world value with one standard deviation on the best fit value and the one-sigma contour has been studied. The effect induced by these variations on the best-fit values is comparable with the one-sigma contour obtained by taking the central value.

The results of these studies are, when applicable, shown in Fig. 7.9, on top of the χ^2-distribution of the main fit. The effect of varying the hadronisation fraction has a more pronounced effect on the resulting charm quark mass than on the fragmentation function. This is understood in the direct manner in which the charm quark mass enters the total cross section, shown in Ch. 1. From these studies it follows that the systematic error on the best-fit parameters is ±0.05 GeV for the charm quark mass and ±0.001 on ϵ_P, which is negligible compared to the statistical uncertainty on this parameter.

7.9. Fits to the semileptonic cross sections

The cross sections presented in chapter 6 have also been fitted to the predictions of the HVQDIS-programme. Based on the knowledge obtained from the fits on the $D^{*\pm}$ data. For the calculation of the semileptonic distributions, the same settings as for

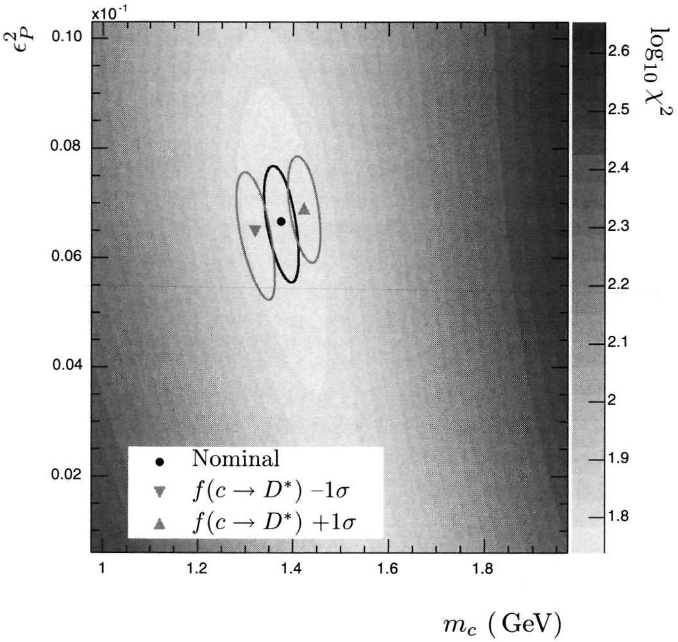

Figure 7.9: *The result of the two parameter extraction on $D^{*\pm}$ production data. The effect of varying the hadronisation scale (triangles) is also shown.*

the $D^{*\pm}$ cross sections were used. In addition the EvtGen-improved semileptonic decay, described in Ch. 2, was used. The branching fraction for the semileptonic decay was set to be $9.6 \pm 0.4\%$.

The result of these fits is summarised in Fig. 7.10. For the semileptonic cross sections no minimum was found. The figure clearly indicates that this can mainly be attributed to the fact that there is no real sensitivity to the ϵ_P parameter. This is likely the result of the convolution of the D-production with the semileptonic decay, diluting the already weak sensitivity to this parameter, as shown in the $D^{*\pm}$-case. Still this χ^2-distribution can be used to further tighten down the charm quark mass and the value for ϵ_P, when this information is combined with the results from the $D^{*\pm}$-fits.

7.10. Combined $D^{*\pm}$ and semileptonic fits

The two χ^2-distribution of both fits can be combined and re-analysed. When doing so, the result of Fig. 7.11 is obtained.

This figure corresponds to the result presented in Tab. 7.9. The maximal variation of the charm quark mass has remained 40 MeV despite the inclusion of the semileptonic results in the fit. The central value of the charm quark mass has come down with 30 MeV, or within 1σ of the statistical error. The uncertainty on ϵ_P has not improved either, as could be expected from the χ^2-distribution of the semileptonic cross section alone. From the evaluation of the systematic effects on the fits on the

Figure 7.10: *χ^2-distribution on the two dimensional grid for the semileptonic cross sections of the previous chapter.*

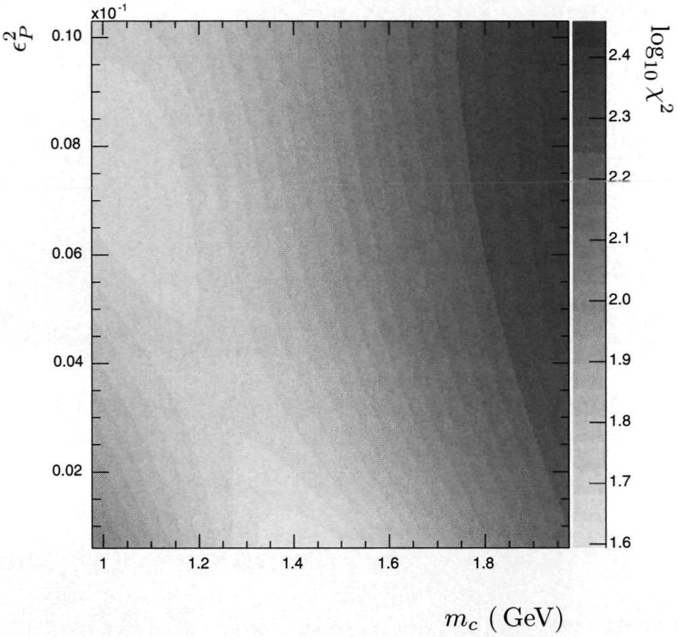

Figure 7.11: *χ^2-distribution of the combined $D^{*\pm}$ and semileptonic data.*

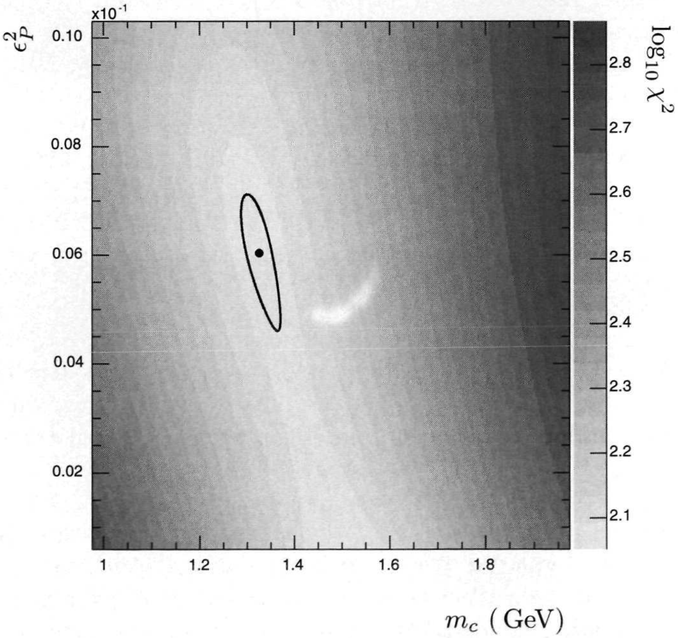

Table 7.9: *The best fit point of the combined two dimensional fit. The uncertainty has been quantified in terms of the extreme values on the* 1σ *contour and the covariance matrix. The best-fit value gave a* χ^2/dof *of 120/89.*

quantity	m_c (GeV)	ϵ_P^2	ϵ_P
best fit value	1.33	$6.03 \cdot 10^{-3}$	0.078
minimum on 1σ	1.29	$4.60 \cdot 10^{-3}$	0.068
maximum on 1σ	1.37	$7.12 \cdot 10^{-3}$	0.084

$$\begin{pmatrix} \sigma_{m_c} & \sigma_{m_c/\epsilon_P^2} \\ \sigma_{m_c/\epsilon_P^2} & \sigma_{\epsilon_P^2} \end{pmatrix} \qquad \begin{pmatrix} 0.035 & 6.16 \cdot 10^{-3} \\ 6.16 \cdot 10^{-3} & 1.40 \cdot 10^{-3} \end{pmatrix}$$

$D^{*\pm}$-data it can be concluded that the systematic uncertainty on the charm mass is of the same order as the statistical one and for ϵ_P it is negligible. This leads to the final estimate for both m_c and ϵ_P of:

$$m_c = 1.33 \pm 0.04 \pm 0.05$$
$$\epsilon_P = 0.078 \pm^{0.008}_{0.010} \pm 0.001$$

where the first uncertainty denotes the statistical and the second the systematic error. The 1σ bands for both parameters are shown for all used distributions in Figs. 7.12, 7.13 and 7.14. The bands for m_c (ϵ_P) are for the central value of ϵ_P (m_c).

7.11. Summary and conclusions

In this chapter it has been shown that the visible cross sections of charm production in DIS *ep* scattering can be used to extract the mass of the charm quark and optimise the functional form of the heavy quark fragmentation function. The method presented is completely novel and therefore contributes to the world knowledge of these two parameters.

The one dimensional fits showed that the little used Kartvelishvili fragmentation function is equally able to describe the $D^{*\pm}$-production cross sections as the traditionally favoured Peterson function.

The dual extraction of the charm quark mass and the optimal Peterson fragmentation function has shown that these two parameters are indeed correlated. This is best demonstrated in the case of the fits on the semileptonic production cross sections, where no minimum can be found, but instead a minimum-trough is seen.

The data prefer a Peterson function parameter of $\epsilon_P = 0.078 \pm 0.010$ which is larger than the one currently in use, by both collaborations. However, the uncertainty already indicates that the visible charm production cross sections are not particularly sensitive to the precise value of this phenomenological parameter.

The largest contribution to the uncertainty in the extraction of the charm quark mass is in the absolute normalisation of the production process, *i.e.* the values of the hadronisation fraction $f(c \to D^{*+})$ and the branching ratio $BR(c \to e^+)$.

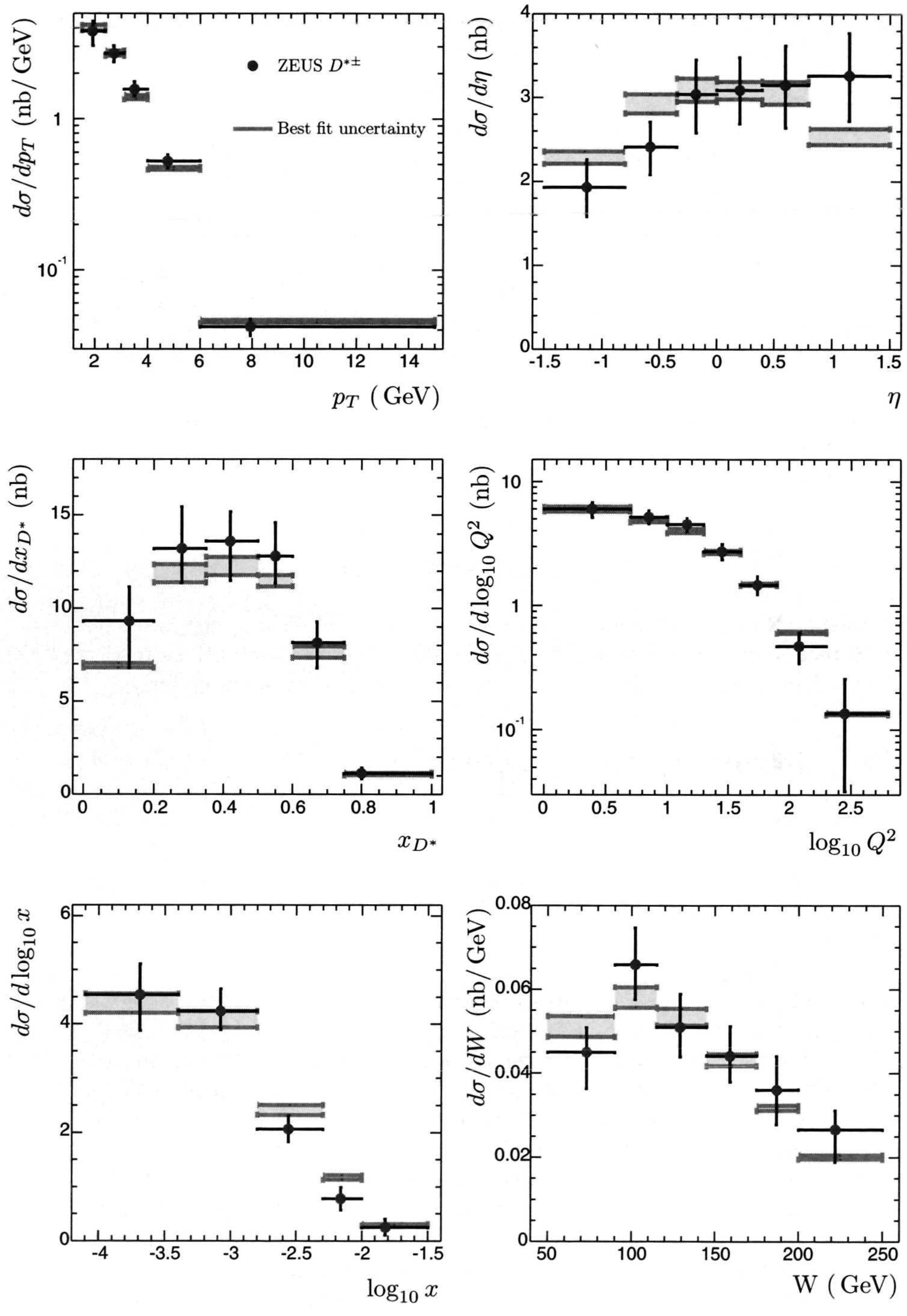

Figure 7.12: *The ZEUS $D^{*\pm}$-cross sections compared to the distributions on the 1σ-contour around the best-fit value.*

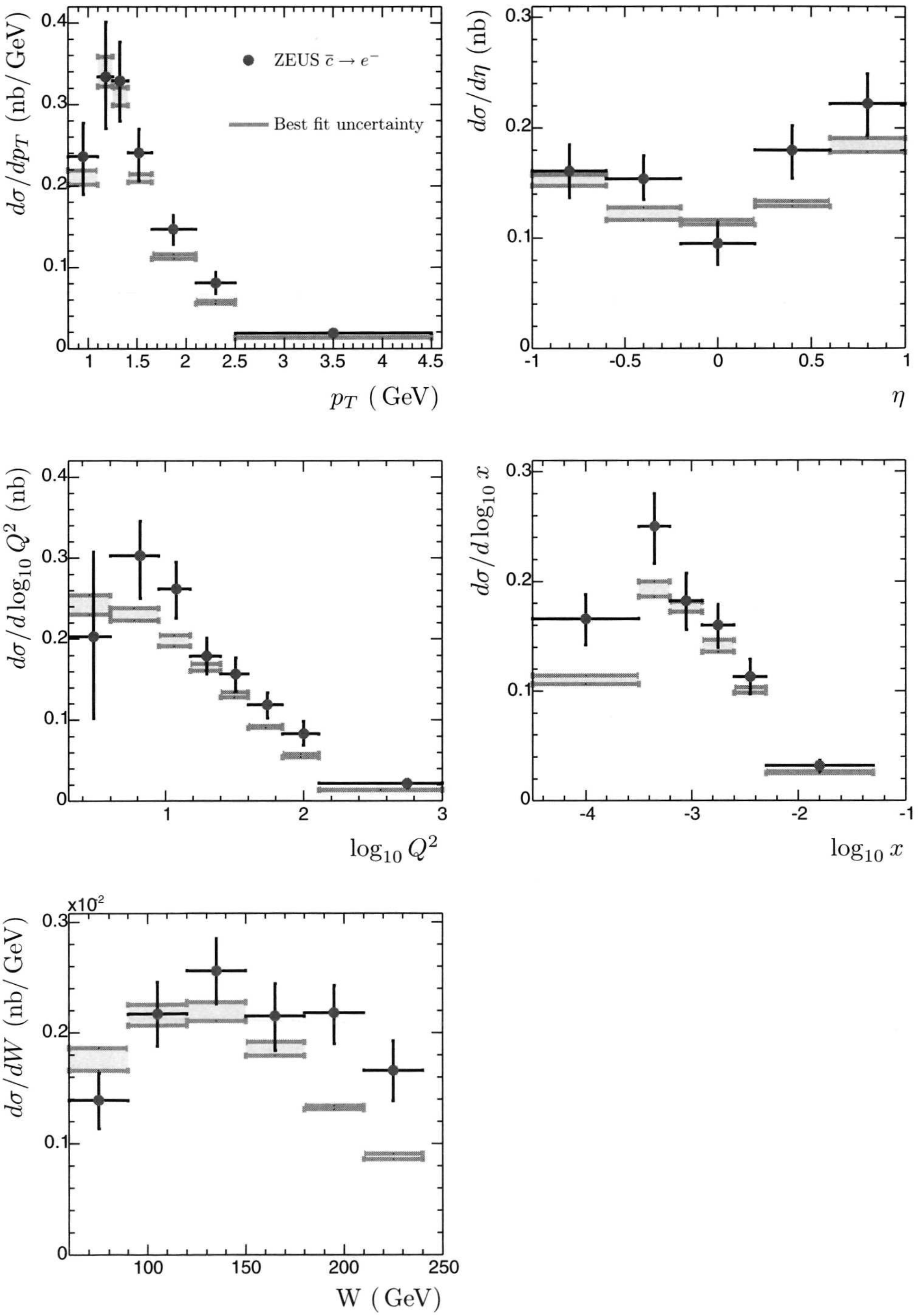

Figure 7.13: *The ZEUS semileptonic cross sections compared to the distributions on the 1σ-contour around the best-fit value.*

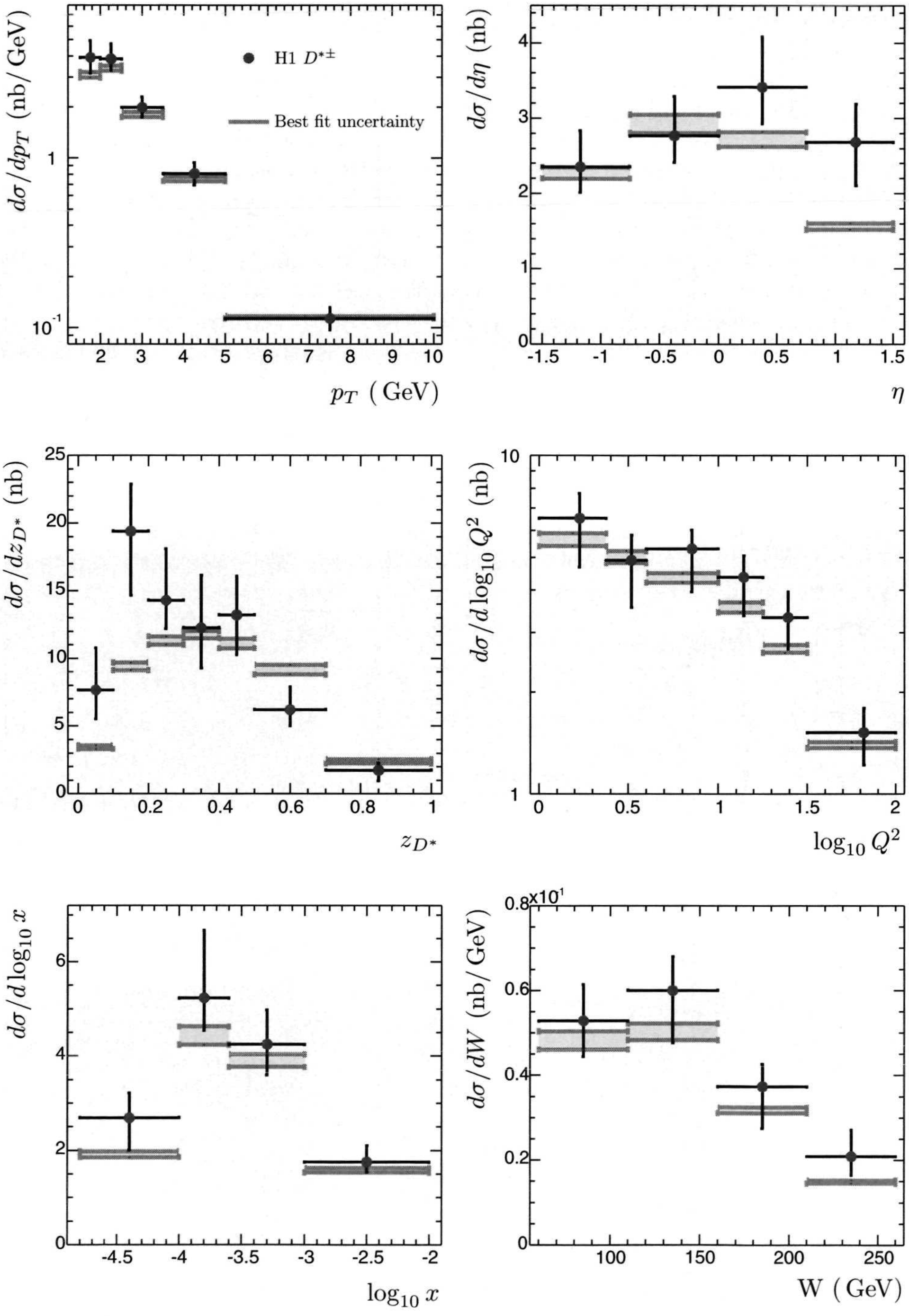

Figure 7.14: *The H1 $D^{*\pm}$-cross sections compared to the distributions on the 1σ-contour around the best-fit value.*

Further improvement on the knowledge of these two numbers will directly improve the systematical uncertainty on the extracted charm quark mass.

The obtained result of the charm quark mass of $m_c = 1.33 \pm 0.04 \pm 0.05$ GeV is in agreement with other measurements of the charm quark mass, while the uncertainty is competitive with results obtained with the methods presented at the beginning of this chapter. However, unlike those methods, the result of the method introduced in this thesis can be improved without having to overcome great technical difficulties.

The statistical uncertainty can be further reduced by including the new $D^{*\pm}$-production data from both H1 and ZEUS, based on the 1998-2000 running of the HERA accelerator. These results use roughly twice the luminosity compared to the results used thus far. The increase in statistics will lead to finer differential cross section measurements, vastly improving the resolution of the fits.

It would also be interesting to see what results are obtained when not the Peterson fragmentation function is used, but some other functional form. The Kartvelishvili form already proved in the one dimensional fits that it is able to describe the charm data.

At last an answer can be provided to the question central to this thesis. The fits lead to the conclusion that, within the uncertainties, both experimental and phenomenological (the fragmentation function), pQCD is indeed able to describe the data. Current discrepancies between the visible cross sections and the theoretical predictions are most likely the result from our limited knowledge of the fragmentation process.

APPENDIX A

Results tabulated

Table A.1: *The results of the measurement of the semileptonic cross section differential in* P_T^{SLe}.

BIN			EXPERIMENTAL RESULTS											
#	$P_{T,min}$ GeV	$P_{T,max}$ GeV	N_{ele}	N_{con}	N_{pro}	N_{dal}	N_{bea}	N_{SLe}	ϵ_{DIS}	ϵ_{SLe}	$\frac{d\sigma}{dP_T}$ (nb/GeV)	Uncertainty		
												stat.	+syst.	-syst.
1	0.80	1.10	1515.2	778.6	121.2	71.5	19.2	524.6	0.290	0.777	0.236	0.038	0.015	0.027
2	1.10	1.25	1193.1	589.6	95.4	52.2	21.7	434.2	0.329	0.802	0.334	0.055	0.038	0.032
3	1.25	1.40	1019.3	415.1	81.5	45.4	22.6	454.7	0.358	0.784	0.329	0.045	0.015	0.021
4	1.40	1.65	1226.0	456.1	98.1	51.5	32.8	587.6	0.393	0.757	0.241	0.027	0.010	0.021
5	1.65	2.10	1280.2	410.2	102.4	50.5	39.5	677.5	0.436	0.717	0.146	0.015	0.008	0.011
6	2.10	2.50	649.8	196.6	52.0	23.4	23.3	354.5	0.490	0.678	0.081	0.011	0.007	0.007
7	2.50	4.50	785.3	207.6	62.8	31.4	48.9	434.5	0.557	0.609	0.019	0.003	0.002	0.002

Table A.2: *The results of the measurement of the semileptonic cross section differential in* η^{SLe}.

BIN			EXPERIMENTAL RESULTS											
#	η_{min}	η_{max}	N_{ele}	N_{con}	N_{pro}	N_{dal}	N_{bea}	N_{SLe}	ϵ_{DIS}	ϵ_{SLe}	$\frac{d\sigma}{d\eta}$ (nb)	Uncertainty stat.	 +syst.	 -syst.
1	-1.0	-0.6	1397.8	640.4	111.8	68.3	26.9	550.4	0.366	0.714	0.160	0.022	0.009	0.011
2	-0.6	-0.2	1242.2	409.0	99.4	47.7	35.9	650.2	0.416	0.771	0.154	0.017	0.012	0.009
3	-0.2	0.2	951.4	390.8	76.1	41.6	38.9	404.0	0.435	0.742	0.095	0.016	0.010	0.011
4	0.2	0.6	1459.0	541.8	116.7	52.0	44.6	704.0	0.399	0.748	0.180	0.020	0.009	0.016
5	0.6	1.0	1819.6	757.4	145.6	78.2	49.3	789.1	0.356	0.759	0.222	0.024	0.012	0.016

Table A.5: *The results of the measurement of the semileptonic cross section differential in W.*

BIN			EXPERIMENTAL RESULTS											
#	W_{min} GeV	W_{max} GeV	N_{ele}	N_{con}	N_{pro}	N_{dal}	N_{bea}	N_{SLe}	ϵ_{DIS}	ϵ_{SLe}	$\frac{d\sigma}{dW}$ (pb)/GeV	Uncertainty stat.	+syst.	-syst.
1	60	90	1246.6	651.6	99.7	49.9	14.0	431.3	0.395	0.799	1.39	0.22	0.10	0.13
2	90	120	1515.6	648.3	121.2	65.9	32.8	647.3	0.395	0.767	2.17	0.24	0.15	0.15
3	120	150	1608.8	594.2	128.7	65.3	45.4	775.2	0.409	0.753	2.56	0.24	0.16	0.17
4	150	180	1370.3	559.5	109.6	59.2	46.6	595.3	0.396	0.710	2.15	0.25	0.15	0.18
5	180	210	1143.4	341.7	91.5	49.7	44.9	615.7	0.419	0.684	2.18	0.21	0.12	0.18
6	210	240	675.5	217.3	54.0	33.5	26.1	344.6	0.309	0.682	1.66	0.22	0.14	0.16

APPENDIX B

Graphical overview of systematic studies

The figures presented here follow the same key as Fig. 6.3. The key for the figures is presented again in Fig. B.1. If the statistical error is larger than 30% it is not shown in the figure. The same is true for (individual) systematic uncertainties that exceed this value.

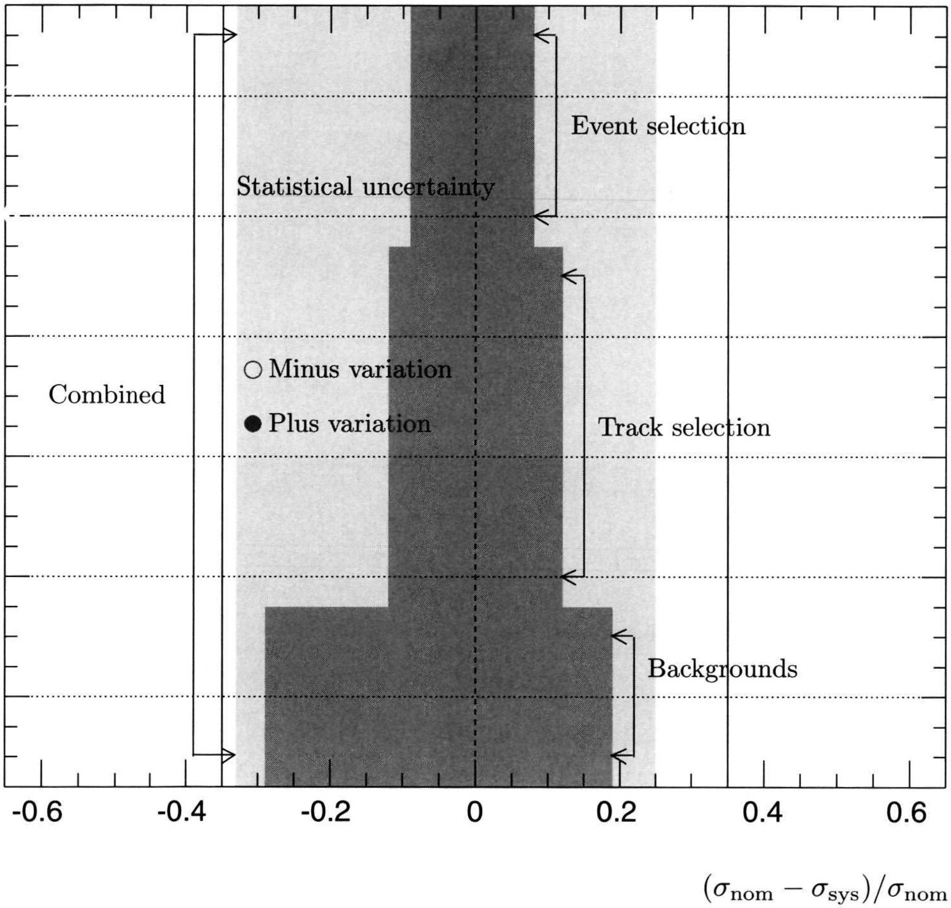

Figure B.1: *The key for the graphical representation of the results of the systematic studies. For a given bin, the dashed line shows the statistical error. The effects of the different variations are given by the points, where the open (solid) points depict the lowering (raising) of the selection criterium or background constribution. The light shade shows the total (combined) systematic uncertainty while the dark shade gives the combined contribution for a given category (event selection, track selection or backgrounds).*

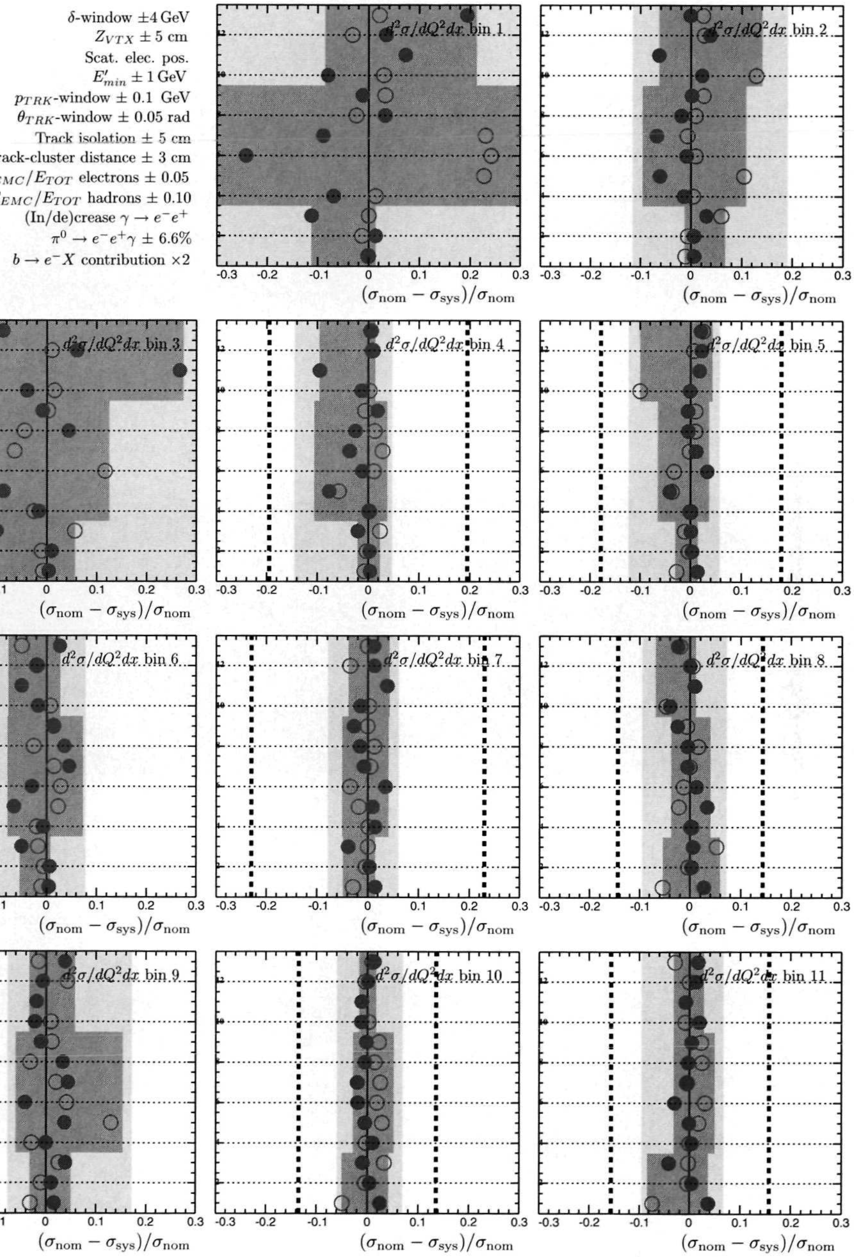
δ-window ±4 GeV
Z_{VTX} ± 5 cm
Scat. elec. pos.
E'_{min} ± 1 GeV
p_{TRK}-window ± 0.1 GeV
θ_{TRK}-window ± 0.05 rad
Track isolation ± 5 cm
Track-cluster distance ± 3 cm
E_{EMC}/E_{TOT} electrons ± 0.05
E_{EMC}/E_{TOT} hadrons ± 0.10
(In/de)crease $\gamma \rightarrow e^-e^+$
$\pi^0 \rightarrow e^-e^+\gamma$ ± 6.6%
$b \rightarrow e^-X$ contribution ×2
$d^2\sigma/dQ^2dx$ bin 1
$d^2\sigma/dQ^2dx$ bin 2
$d^2\sigma/dQ^2dx$ bin 3
$d^2\sigma/dQ^2dx$ bin 4
$d^2\sigma/dQ^2dx$ bin 5
$d^2\sigma/dQ^2dx$ bin 6
$d^2\sigma/dQ^2dx$ bin 7
$d^2\sigma/dQ^2dx$ bin 8
$d^2\sigma/dQ^2dx$ bin 9
$d^2\sigma/dQ^2dx$ bin 10
$d^2\sigma/dQ^2dx$ bin 11
-0.3
-0.2
-0.1
0
0.1
0.2
0.3
$(\sigma_{\rm nom} - \sigma_{\rm sys})/\sigma_{\rm nom}$

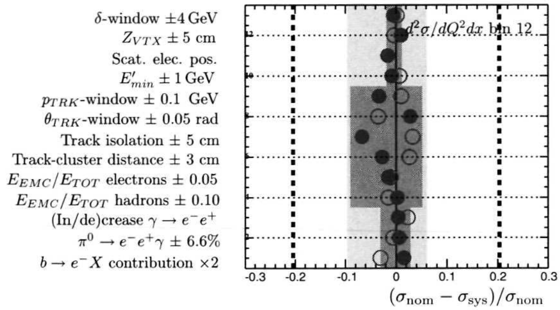
δ-window $\pm 4\,\mathrm{GeV}$
$Z_{VTX} \pm 5$ cm
Scat. elec. pos.
$E'_{min} \pm 1\,\mathrm{GeV}$
p_{TRK}-window $\pm$ 0.1 GeV
θ_{TRK}-window $\pm$ 0.05 rad
Track isolation $\pm$ 5 cm
Track-cluster distance $\pm$ 3 cm
E_{EMC}/E_{TOT} electrons $\pm$ 0.05
E_{EMC}/E_{TOT} hadrons $\pm$ 0.10
(In/de)crease $\gamma \rightarrow e^-e^+$
$\pi^0 \rightarrow e^-e^+\gamma \pm 6.6\%$
$b \rightarrow e^-X$ contribution $\times 2$
$d^2\sigma/dQ^2dx$ bin 12
-0.3 -0.2 -0.1 0 0.1 0.2 0.3
$(\sigma_{\mathrm{nom}} - \sigma_{\mathrm{sys}})/\sigma_{\mathrm{nom}}$

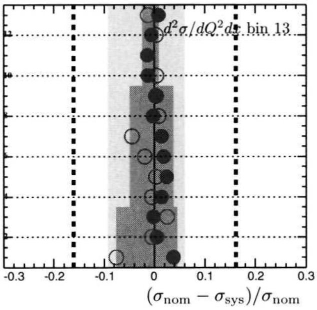
$d^2\sigma/dQ^2dx$ bin 13
-0.3 -0.2 -0.1 0 0.1 0.2 0.3
$(\sigma_{\mathrm{nom}} - \sigma_{\mathrm{sys}})/\sigma_{\mathrm{nom}}$

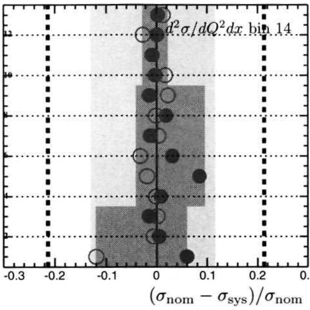
$d^2\sigma/dQ^2dx$ bin 14
-0.3 -0.2 -0.1 0 0.1 0.2 0.3
$(\sigma_{\mathrm{nom}} - \sigma_{\mathrm{sys}})/\sigma_{\mathrm{nom}}$

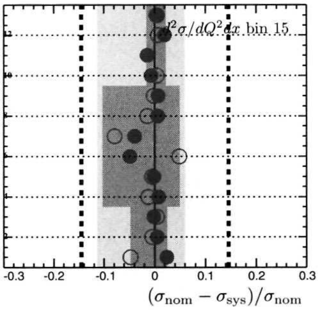
$d^2\sigma/dQ^2dx$ bin 15
-0.3 -0.2 -0.1 0 0.1 0.2 0.3
$(\sigma_{\mathrm{nom}} - \sigma_{\mathrm{sys}})/\sigma_{\mathrm{nom}}$

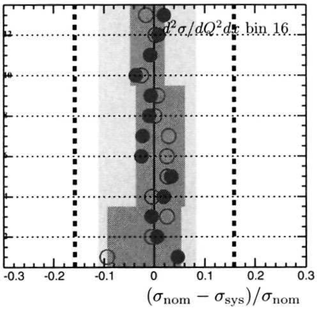
$d^2\sigma/dQ^2dx$ bin 16
-0.3 -0.2 -0.1 0 0.1 0.2 0.3
$(\sigma_{\mathrm{nom}} - \sigma_{\mathrm{sys}})/\sigma_{\mathrm{nom}}$

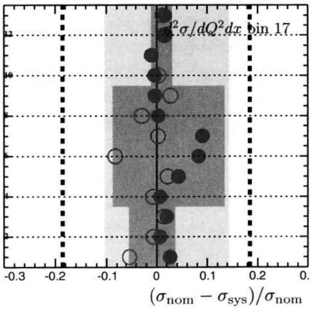
$d^2\sigma/dQ^2dx$ bin 17
-0.3 -0.2 -0.1 0 0.1 0.2 0.3
$(\sigma_{\mathrm{nom}} - \sigma_{\mathrm{sys}})/\sigma_{\mathrm{nom}}$

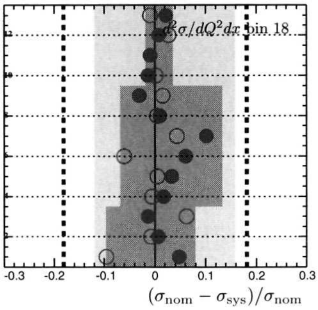
$d^2\sigma/dQ^2dx$ bin 18
-0.3 -0.2 -0.1 0 0.1 0.2 0.3
$(\sigma_{\mathrm{nom}} - \sigma_{\mathrm{sys}})/\sigma_{\mathrm{nom}}$

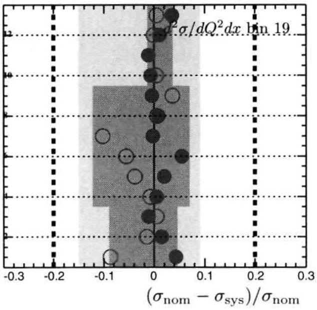
$d^2\sigma/dQ^2dx$ bin 19
-0.3 -0.2 -0.1 0 0.1 0.2 0.3
$(\sigma_{\mathrm{nom}} - \sigma_{\mathrm{sys}})/\sigma_{\mathrm{nom}}$

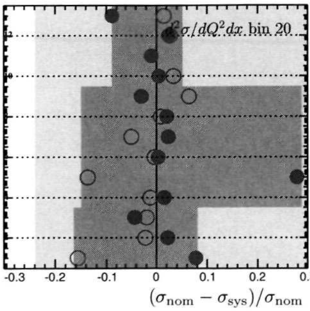
$d^2\sigma/dQ^2dx$ bin 20
-0.3 -0.2 -0.1 0 0.1 0.2 0.3
$(\sigma_{\mathrm{nom}} - \sigma_{\mathrm{sys}})/\sigma_{\mathrm{nom}}$

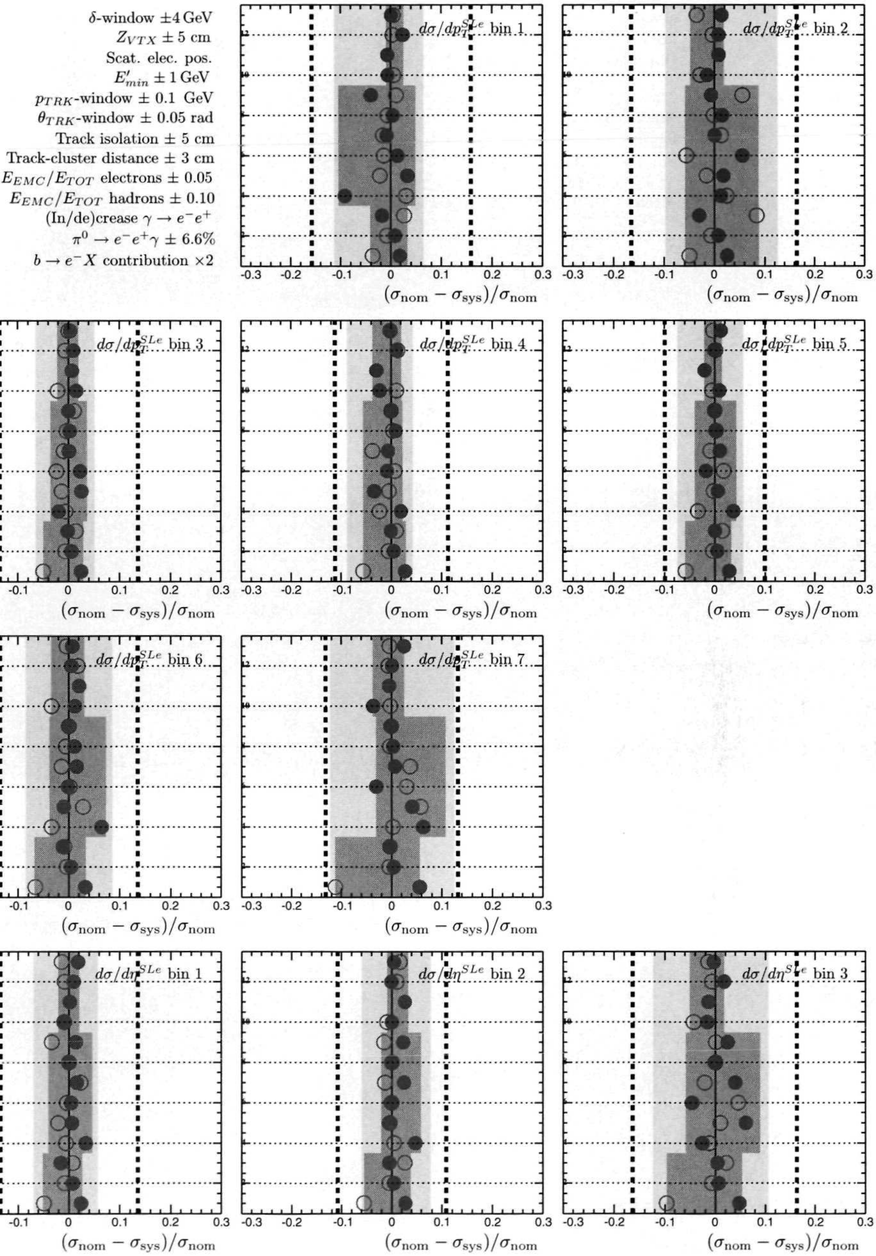
δ-window ±4 GeV
Z_{VTX} ± 5 cm
Scat. elec. pos.
E'_{min} ± 1 GeV
p_{TRK}-window ± 0.1 GeV
θ_{TRK}-window ± 0.05 rad
Track isolation ± 5 cm
Track-cluster distance ± 3 cm
E_{EMC}/E_{TOT} electrons ± 0.05
E_{EMC}/E_{TOT} hadrons ± 0.10
(In/de)crease $\gamma \to e^- e^+$
$\pi^0 \to e^- e^+ \gamma$ ± 6.6%
$b \to e^- X$ contribution ×2
$d\sigma/dp_T^{SLe}$ bin 1
$d\sigma/dp_T^{SLe}$ bin 2
$d\sigma/dp_T^{SLe}$ bin 3
$d\sigma/dp_T^{SLe}$ bin 4
$d\sigma/dp_T^{SLe}$ bin 5
$d\sigma/dp_T^{SLe}$ bin 6
$d\sigma/dp_T^{SLe}$ bin 7
$d\sigma/d\eta^{SLe}$ bin 1
$d\sigma/d\eta^{SLe}$ bin 2
$d\sigma/d\eta^{SLe}$ bin 3
-0.3 -0.2 -0.1 0 0.1 0.2 0.3
$(\sigma_{\rm nom} - \sigma_{\rm sys})/\sigma_{\rm nom}$

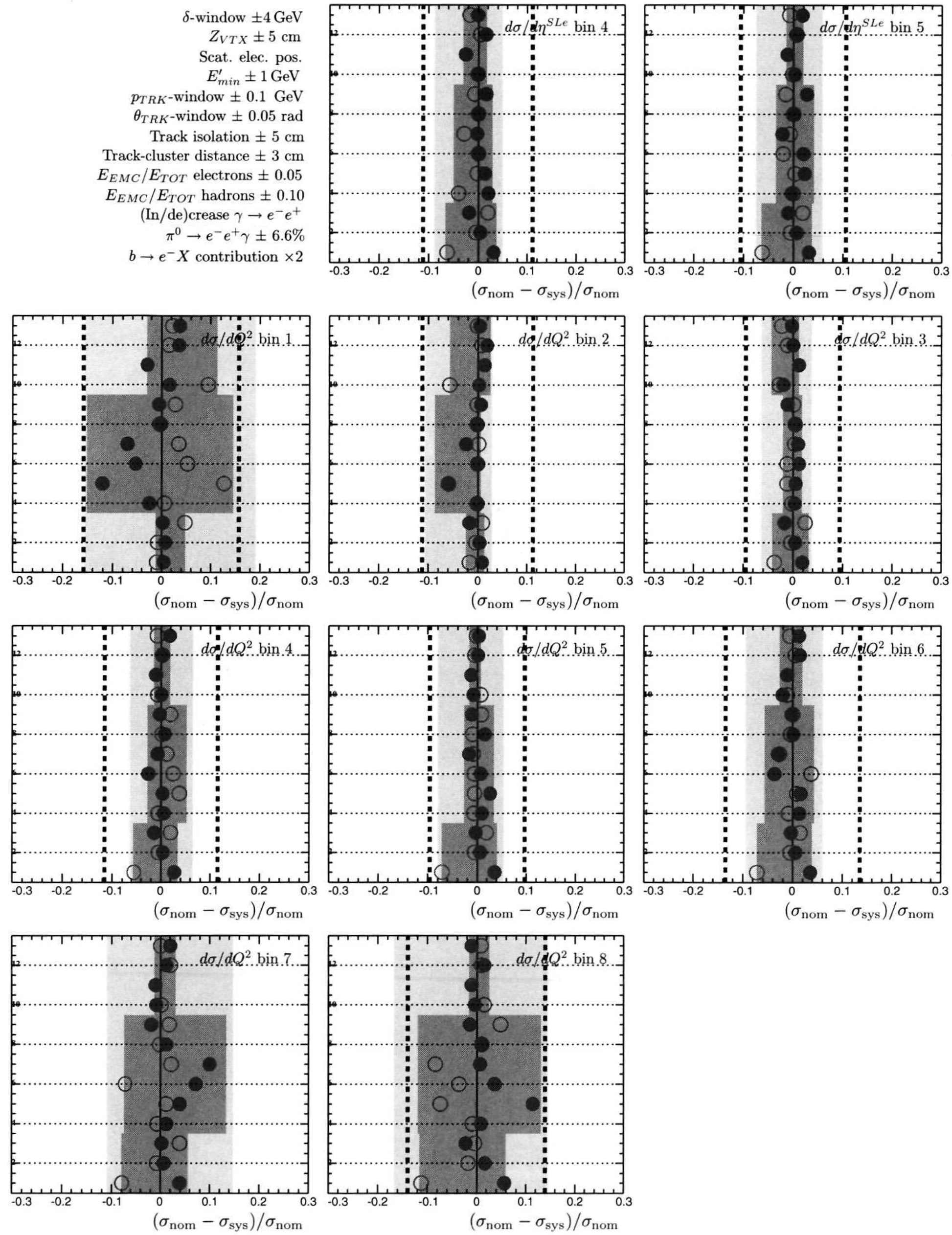
δ-window ±4 GeV
Z_{VTX} ± 5 cm
Scat. elec. pos.
E'_{min} ± 1 GeV
p_{TRK}-window ± 0.1 GeV
θ_{TRK}-window ± 0.05 rad
Track isolation ± 5 cm
Track-cluster distance ± 3 cm
E_{EMC}/E_{TOT} electrons ± 0.05
E_{EMC}/E_{TOT} hadrons ± 0.10
(In/de)crease $\gamma \to e^-e^+$
$\pi^0 \to e^-e^+\gamma$ ± 6.6%
$b \to e^-X$ contribution ×2
$d\sigma/d\eta^{SLe}$ bin 4
$d\sigma/d\eta^{SLe}$ bin 5
$d\sigma/dQ^2$ bin 1
$d\sigma/dQ^2$ bin 2
$d\sigma/dQ^2$ bin 3
$d\sigma/dQ^2$ bin 4
$d\sigma/dQ^2$ bin 5
$d\sigma/dQ^2$ bin 6
$d\sigma/dQ^2$ bin 7
$d\sigma/dQ^2$ bin 8
-0.3 -0.2 -0.1 0 0.1 0.2 0.3
$(\sigma_{\rm nom} - \sigma_{\rm sys})/\sigma_{\rm nom}$

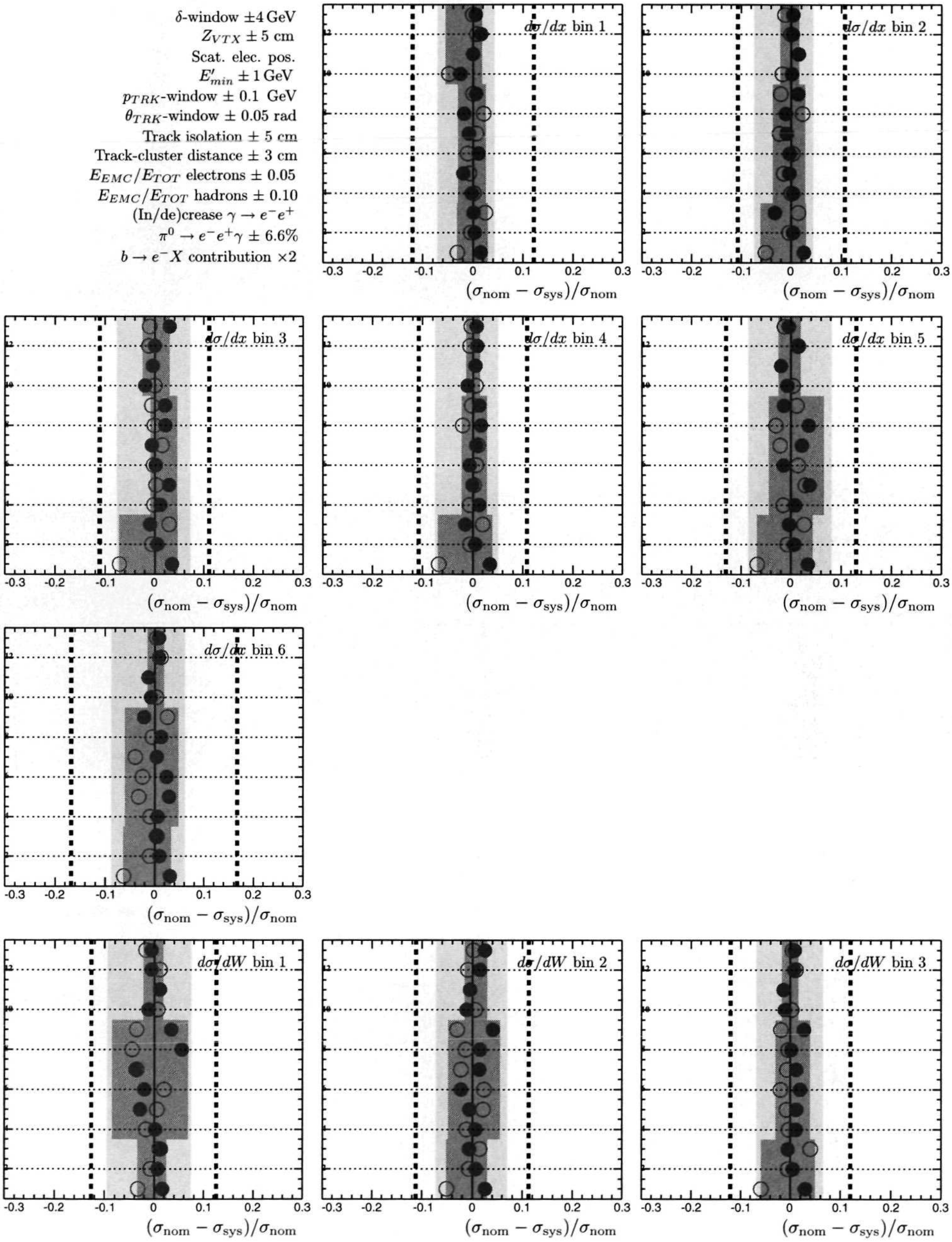
δ-window ±4 GeV
Z_{VTX} ± 5 cm
Scat. elec. pos.
E'_{min} ± 1 GeV
p_{TRK}-window ± 0.1 GeV
θ_{TRK}-window ± 0.05 rad
Track isolation ± 5 cm
Track-cluster distance ± 3 cm
E_{EMC}/E_{TOT} electrons ± 0.05
E_{EMC}/E_{TOT} hadrons ± 0.10
(In/de)crease $\gamma \to e^-e^+$
$\pi^0 \to e^-e^+\gamma$ ± 6.6%
$b \to e^-X$ contribution ×2
$d\sigma/dx$ bin 1
$d\sigma/dx$ bin 2
$d\sigma/dx$ bin 3
$d\sigma/dx$ bin 4
$d\sigma/dx$ bin 5
$d\sigma/dx$ bin 6
$d\sigma/dW$ bin 1
$d\sigma/dW$ bin 2
$d\sigma/dW$ bin 3
-0.3 -0.2 -0.1 0 0.1 0.2 0.3
$(\sigma_{\rm nom} - \sigma_{\rm sys})/\sigma_{\rm nom}$

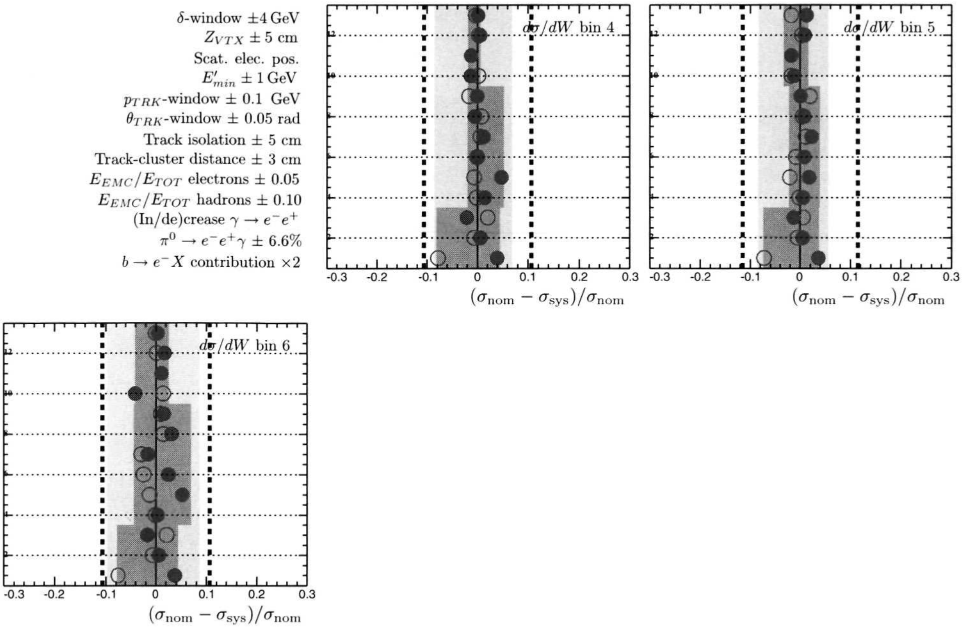
δ-window ± 4 GeV
$Z_{VTX} \pm 5$ cm
Scat. elec. pos.
$E'_{min} \pm 1$ GeV
p_{TRK}-window $\pm$ 0.1 GeV
θ_{TRK}-window $\pm$ 0.05 rad
Track isolation $\pm$ 5 cm
Track-cluster distance $\pm$ 3 cm
E_{EMC}/E_{TOT} electrons $\pm$ 0.05
E_{EMC}/E_{TOT} hadrons $\pm$ 0.10
(In/de)crease $\gamma \rightarrow e^-e^+$
$\pi^0 \rightarrow e^-e^+\gamma \pm 6.6\%$
$b \rightarrow e^-X$ contribution $\times 2$
$d\sigma/dW$ bin 4
$d\sigma/dW$ bin 5
$d\sigma/dW$ bin 6
-0.3
-0.2
-0.1
0
0.1
0.2
0.3
$(\sigma_{\rm nom} - \sigma_{\rm sys})/\sigma_{\rm nom}$

APPENDIX C

χ^2 distributions to the NLO-pQCD fits

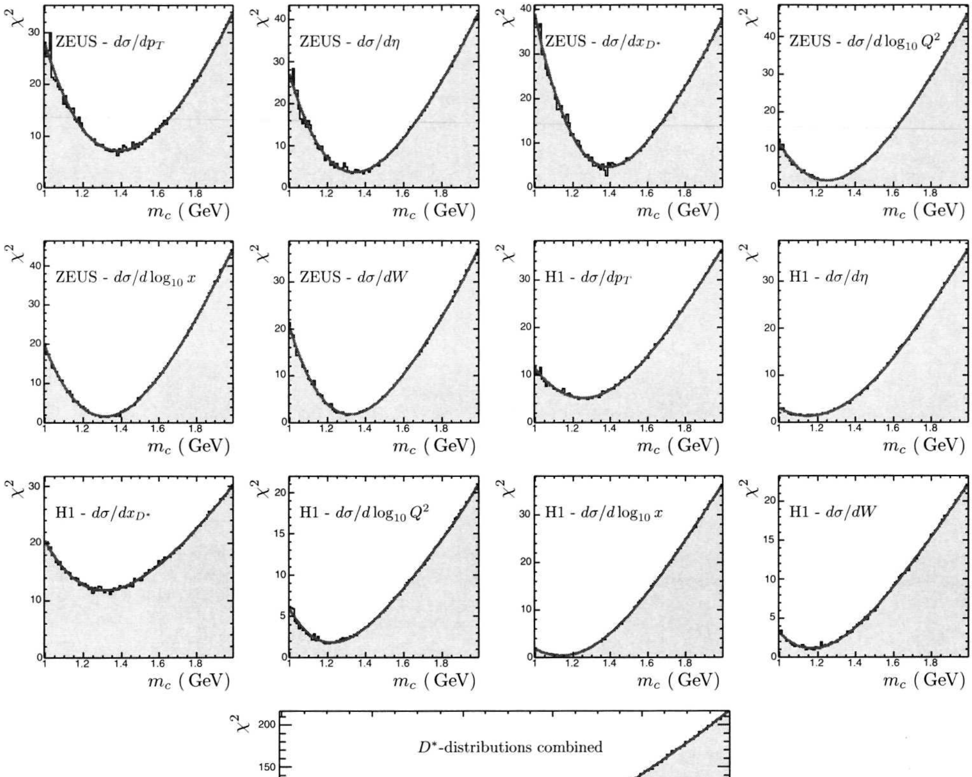

Figure C.1: *The χ^2-distributions of the fits on m_c with $\epsilon_P = 0.035$ for individual cross sections and the combined result (bottom). The line shows the fifth order polynomial that was fitted to the distribution.*

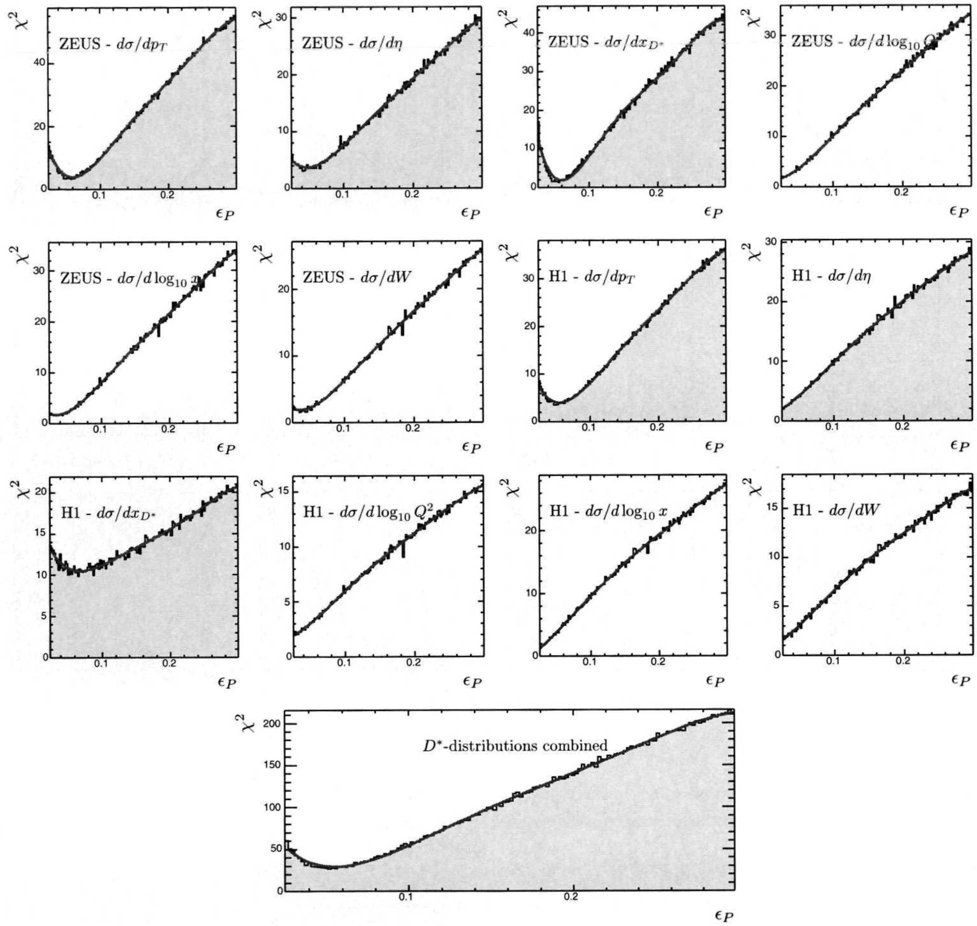

Figure C.2: *The χ^2 distributions of the first fits on ϵ_P with m_c fixed to 1.30 GeV. The D^*-distributions have filled histograms. Only these distributions were used to obtain the combined result (bottom row). The line shows the fifth order polynomial that was fitted to the distribution.*

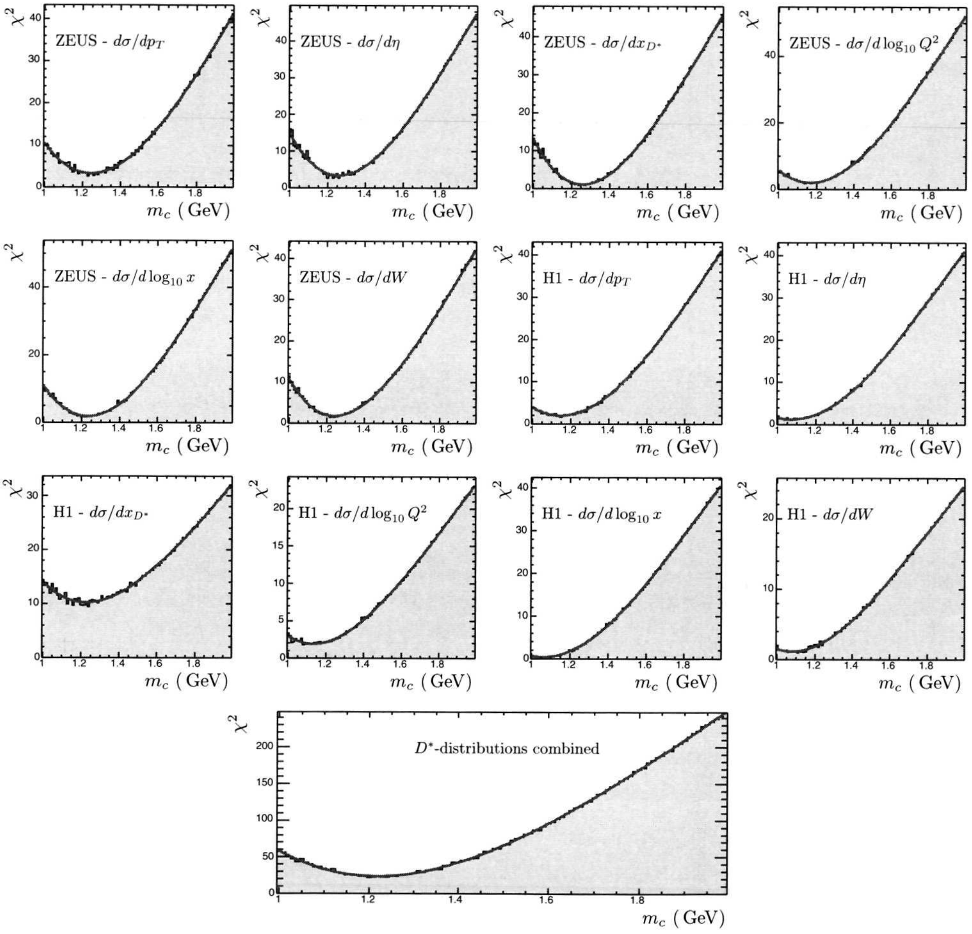

Figure C.3: *The χ^2-distributions of the fits on m_c with $\epsilon_P = 0.054$ for individual cross sections and the combined result (bottom). The line shows the fifth order polynomial that was fitted to the distribution.*

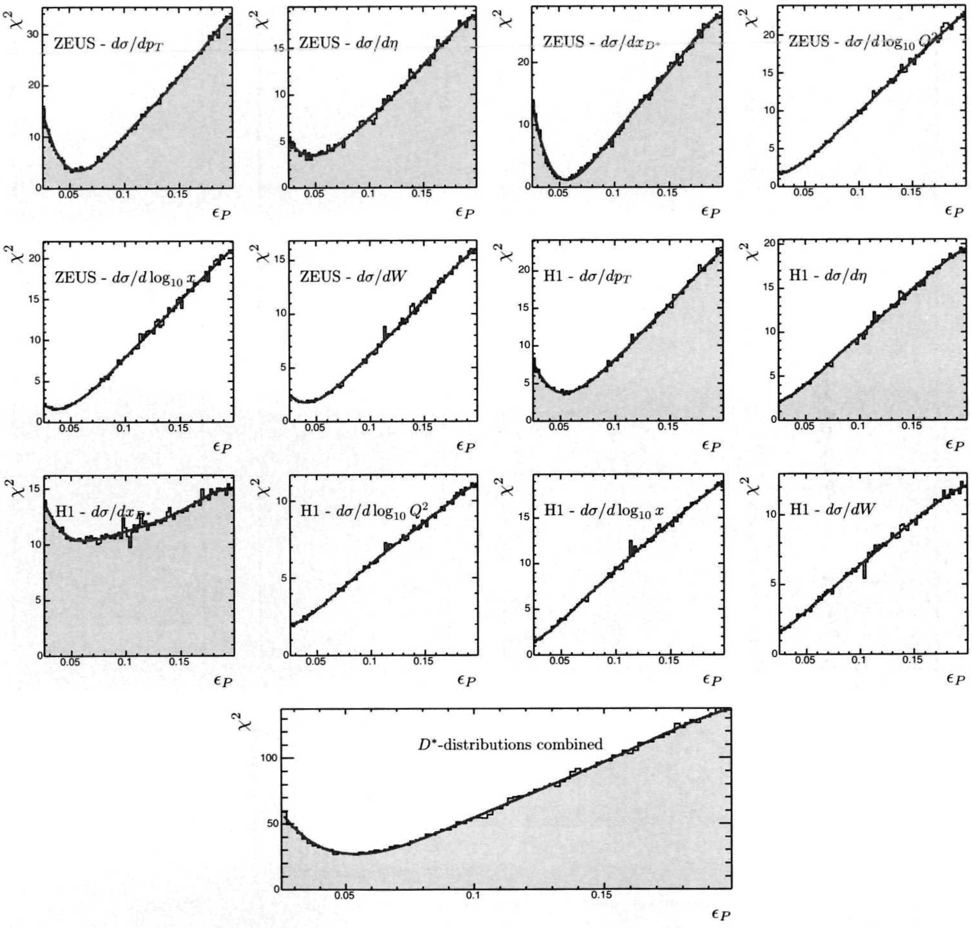

Figure C.4: *The χ^2 distributions of the first fits on ϵ_P with m_c fixed to 1.29 GeV. The D^*-distributions have filled histograms. Only these distributions were used to obtain the combined result (bottom row). The line shows the fifth order polynomial that was fitted to the distribution.*

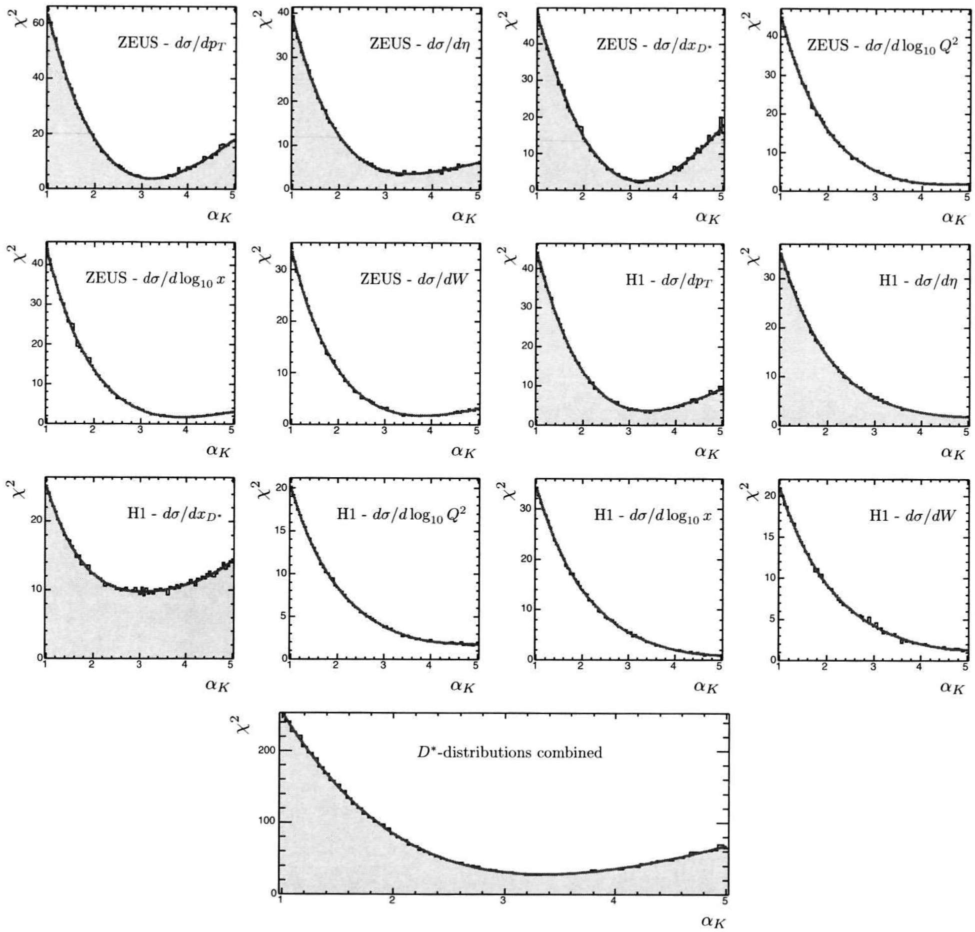

Figure C.5: *The χ^2 distributions of the fits of α_K for m_c = 1.30 GeV. The D^*-distributions have filled histograms. Only these distributions were used to obtain the combined result (bottom row). The line shows the fifth order polynomial that was fitted to the distribution.*

References

[1] E.D. Bloom et al., *High-energy inelastic ep scattering at* 6° *and* 10°. Phys. Rev. Lett. **23**, 930 (1969);
M. Breidenbach et al., *Observed behaviour of highly inelastic electron-proton scattering.* Phys. Rev. Lett. **23**, 935 (1969).

[2] Yu.L. Dokshitzer, *Calculation of the structure functions for deep inelastic scattering and* e^+e^- *annihilation by perturbation theory in Quantum Chromodynamics [in Russian].* Sov. Phys. JETP **46**, 641 (1977).

[3] V.N. Gribov and L.N. Lipatov, *Deep inelastic ep scattering in perturbation theory.* Sov. J. Nucl. Phys. **15**, 438 (1972).

[4] G. Altarelli and G. Parisi, *Asymptotic freedom in parton language.* Nucl. Phys. **B 126**, 298 (1977).

[5] ZEUS Coll., J. Breitweg et al., *Observation of scaling violations in scaled momentum distributions at HERA.* Phys. Lett. **B 414**, 428 (1997);
H1 Coll., I. Abt et al., *Scaling violations of the proton structure functions* F_2 *at small* x. Phys. Lett. **B 321**, 161 (1994).

[6] E. Laenen et al., *Complete* $\mathcal{O}(\alpha_s)$ *corrections to heavy flavor structure functions in electroproduction.* Nucl. Phys. **B 392**, 162 (1993).

[7] M. Buza, Y. Matiounine, J. Smith, R. Migneron, and W. L. van Neerven, *Heavy quark coefficient functions at asymptotic values* $Q^2 \gg m^2$. NP **B472**, 611 (1996).

[8] M. Buza et al., *Comparison between the various descriptions for charm electroproduction and the HERA data.* Phys. Lett. **B 411**, 211 (1997).

[9] R.G. Roberts and R.S. Thorne, *Ordered analysis of heavy flavor production in deep inelastic scattering.* Phys. Rev. **D 57**, 6871 (1998);

R.G. Roberts and R.S. Thorne, *A practical procedure for evolving heavy flavour structure functions.* Phys. Lett. **B 421**, 303 (1998).

[10] ZEUS Coll., J. Breitweg et al., *ZEUS results on the measurement and phenomenology of* F_2 *at low* x *and low* Q^2. Eur. Phys. J. **C 7**, 609 (1999).

[11] M. Glück, E. Reya and A. Vogt, *Dynamical parton distributions revisited.* Eur. Phys. J. **C 5**, 461 (1998).

[12] CTEQ Coll., H.L. Lai et al., *Global QCD analysis of parton structure of the nucleon: CTEQ5 parton distributions.* Eur. Phys. J. **C 12**, 375 (2000).

[13] J. Pumplin et al., *New generation of parton distributions with uncertainties from global QCD analysis.* Preprint hep-ph/0201195, 2002.

[14] E.A. Kuraev, L.N. Lipatov and V.S. Fadin, *Multi-reggeon processes in the Yang–Mills theory.* Sov. Phys. JETP **44**, 443 (1976).

[15] Ya.Ya. Balitskiĭ and L.N. Lipatov, *The Pomeranchuk singularity in Quantum Chromodynamics.* Sov. J. Nucl. Phys. **28**, 822 (1978).

[16] M. Ciafaloni, *Coherence effects in initial jets at small* Q^2/s. Nucl. Phys. **B 296**, 49 (1988).

[17] S. Catani, F. Fiorani and G. Marchesini, *QCD coherence in initial state radiation.* Phys. Lett. **B 234**, 339 (1990);
S. Catani, F. Fiorani and G. Marchesini, *Small-*x *behaviour of initial state radiation in perturbative QCD.* Nucl. Phys. **B 336**, 18 (1990);
G. Marchesini, *QCD coherence in the structure function and associated distributions at small* x. Nucl. Phys. **B445**, 49 (1995).

[18] J. A. M. Vermaseren, S. Moch and A. Vogt, *First results for three-loop deep-inelastic structure functions in QCD.* Preprint hep-ph/0211296, 2002.

[19] ZEUS Coll., S. Chekanov et al., *ZEUS next-to-leading-order QCD analysis of data on deep inelastic scattering.* Phys. Rev. **D 67**, 012007 (2003).

[20] H1 Coll., C. Adloff et al., *Deep inelastic inclusive ep scattering at low* x *and a determination of* α_s. Eur. Phys. J. **C 21**, 33 (2001).

[21] V.S. Fadin and L.N. Lipatov, *BFKL pomeron in the next-to-leading approximation.* Phys. Lett. **B 429**, 127 (1998);
G. Camici, M. Ciafaloni, *Energy scale(s) and next-to-leading BFKL equation.* Phys. Lett. **B 430**, 349 (1998).

[22] Y. Azimov et al., *The string effect and QCD coherence.* Phys. Lett. **B 165**, 147 (1985);
G. Gustafson and U. Petterson, *Dipole formation of QCD cascades.* Nucl. Phys. **B306**, 746 (1988);
B. Andersson et al., *Coherence effects in deep inelastic scattering.* Z. Phys. **C 43**, 625 (1989).

[23] B. Andersson et al., *Parton fragmentation and string dynamics.* Phys. Rep. **97**, 31 (1983).

[24] A. Kwiatkowski, H. Spiesberger and H.-J. Möhring, HERACLES*: An event generator for ep interactions at HERA energies including radiative processes (version 1.0).* Comp. Phys. Comm. **69**, 155 (1992). Also in *Proc. Workshop Physics at HERA*, 1991, DESY, Hamburg.

[25] K. Charchula, G.A. Schuler and H. Spiesberger, *Combined QED and QCD radiative effects in deep inelastic lepton-proton scattering: The Monte Carlo generator DJANGO6.* Comp. Phys. Comm. **81**, 381 (1994).

[26] ZEUS Coll., S. Chekanov et al., *Measurement of the neutral current cross-section and F_2 structure function for deep inelastic e^+p scattering at HERA.* Eur. Phys. J. **C 21**, 443 (2001).

[27] G. Ingelman, A. Edin and J. Rathsman, LEPTO 6.5*: A Monte Carlo generator for deep inelastic lepton–nucleon scattering.* Comp. Phys. Comm. **101**, 108 (1997).

[28] L. Lönnblad, ARIADNE *version 4 – a program for simulation of QCD cascades implementing the colour dipole model.* Comp. Phys. Comm. **71**, 15 (1992).

[29] T. Sjöstrand, *High-energy physics event generation with* PYTHIA 5.7 *and* JETSET 7.4. Comp. Phys. Comm. **82**, 74 (1994).

[30] H.L. Lai et al., *Improved parton distributions from global analysis of recent deep inelastic scattering and inclusive jet data.* Phys. Rev. **D 55**, 1280 (1997).

[31] H. Jung, *Hard diffractive scattering in high energy ep collisions and the Monte Carlo generator* RAPGAP. Comp. Phys. Comm. **86**, 147 (1995).

[32] W. Verkerke, *Measurement of Charm Production in Deep Inelastic Scattering.* Thesis, Univeristy of Amsterdam, 1998.

[33] K. Hagiwara et al., *Review of Particle Physics.* Phys. Rev. **D 66**, 010001+ (2002).

[34] G. Corcella et al., HERWIG 6*: An event generator for hadron emission reactions with interfering gluons (including supersymmetric processes).* Journal of High Energy Phys. **01**, 010 (2001).

[35] C. Peterson et al., *Scaling violations in inclusive e^+e^- annihilation spectra.* Phys. Rev. **D 27**, 105 (1983).

[36] Particle Data Group, D.E. Groom et al., *Review of particle physics.* Eur. Phys. J. **C 15**, 1 (2000).

[37] V. G. Kartvelishvili, A. K. Likhoded and V. A. Petrov, *On the fragmentation function of heavy quarks into hadrons.* Phys. Lett. **B 78**, 615 (1978).

[38] R. Brun et al., GEANT3, Technical Report CERN-DD/EE/84-1, CERN, 1987.

[39] B. W. Harris and J. Smith, *Charm quark and* $D^{*\pm}$ *cross sections in deep inelastic scattering at DESY HERA*. Phys. Rev. **D**, 2806 (1998).

[40] B. W. Harris and J. Smith, *Heavy-quark correlations in deep inelastic scattering.* Nucl. Phys. **B**, 109 (1995);
B. W. Harris and J. Smith, *Invariant mass distributions for heavy quark - anti-quark pairs in deep inelastic electroproduction.* Phys. Lett. **B 353**, 535 (1995). Erratum-ibid **B 359** (1995) 423.

[41] P.G. Lepage, VEGAS*: an adaptive multidimensional integration program* (unpublished). CLNS-80/447, 1980.

[42] K. Hebbel, *Measurement of Charm production in Deep Inelastic ep scattering at HERA*. Ph.D. Thesis, University of Hamburg, 2000.

[43] E. Laenen and B. Harris, *Heavy quark fragmentation ambiguities, B Physics at the Tevatron Run II and Beyond*, K. Anikeev et al. (ed.), p. 525. FERMILAB (2001).

[44] D. Scora, and N. Isgur, *Semileptonic meson decays in the quark model: An update.* Phys. Rev. **D52**, 2783 (1995).

[45] A. Ryd et al., *EvtGen - A Monte Carlo Generator for B-Physics* (unpublished). 2001.

[46] H1 Coll., I. Abt et al., *The H1 detector at HERA*. Nucl. Inst. Meth. **A 386**, 310 (1997).

[47] V. Korbel, *Liquid argon calorimetry at HERA, the H1 calorimeter.* Nucl. Inst. Meth. **A 263**, 70 (1988);
V. Korbel, *The H1 LAr calorimeter at HERA, design, performance and status.* Nucl. Inst. Meth. **A 327**, 209 (1993);
H1 Coll., Calorimeter group, B. Andrieu et al., *The H1 liquid argon calorimeter system.* Nucl. Inst. Meth. **A 336**, 460 (1993);
P. Schacht, *Calibration of the H1 liquid argon calorimeter.* Nucl. Inst. Meth. **A 327**, 212 (1993).

[48] H1 Coll., SPACAL group, T. Nicholls et al., *Performance of an electromagnetic lead/scintillating-fiber calorimeter for the H1 detector.* Nucl. Inst. Meth. **A 374**, 149 (1996);
H1 Coll., SPACAL group, R.-D. Appuhn et al., *The H1 lead/scintillating-fiber calorimeter.* Nucl. Inst. Meth. **A 386**, 397 (1997).

[49] K. Ackerstaff et al., *The HERMES spectrometer.* Nucl. Inst. Meth. **A 417**, 230 (1998).

[50] HERA-B Coll., *HERA-B: An experiment to study CP violation in the B system using an internal target at the HERA proton ring.* Design report DESY-PRC 95/01, 1995.

[51] ZEUS Coll., U. Holm (ed.), *The ZEUS Detector.* Status Report (unpublished), DESY (1993), available on
`http://www-zeus.desy.de/bluebook/bluebook.html`.

[52] G.F. Hartner, *VCTRAK(3.07/04): Offline Output Information* (unpublished). ZEUS-97-064, internal ZEUS-note, 1997;
G. F. Hartner, *VCTRAK Briefing: Program and Math* (unpublished). Zeus-98-058, internal ZEUS-note, 1998.

[53] R. Hall-Wilton et al., *The CTD Tracking Resolution* (unpublished). ZEUS-99-024, internal ZEUS-note, 1999.

[54] H. Bethe and W. Heitler, *On the stopping of fast particles and on the creation of positive electrons.* Proc. Roy. Soc. Lond. **A 146**, 83 (1934).

[55] A. Bamberger et al., *The small angle rear tracking detector of ZEUS.* Nucl. Inst. Meth. **A 401**, 63 (1997).

[56] M. Derrick et al., *Design and construction of the ZEUS barrel calorimeter.* Nucl. Inst. Meth. **A 309**, 77 (1991).

[57] J. Straver, *Design, Construction and Beam Tests of the High Resolution Uranium Scintillator Calorimeter for ZEUS.* Ph.D. Thesis, University of Amsterdam, 1991.

[58] K. J. Gaemers and M. van der Horst, *The process* $e^-p \to \gamma\ e^-p$ *as a fast luminosity monitor for the HERA collider.* Nucl. Phys. **B 316**, 269 (1989).

[59] J. Andruszków et al., *Luminosity measurement in the ZEUS experiment.* Acta Phys. Pol. **B 32**, 2025 (2001).

[60] H. Abramowicz, A. Caldwell and R. Sinkus, *Neural network based electron identification in the ZEUS calorimeter.* Nucl. Inst. Meth. **A 365**, 508 (1995);
R. Sinkus and T. Voss, *Particle identification with neural networks using a rotational invariant moment representation.* Nucl. Inst. Meth. **A 391**, 360 (1997).

[61] N. Tuning, *Proton Structure Functions at HERA.* Ph.D. Thesis, Amsterdam University, 2001.

[62] N. Tuning, *ZUFOs: Hadronic Final State Reconstruction with Calorimeter, Tracking and Backsplash Correction* (unpublished). ZEUS-Note-01-021, 2001.

[63] J. Grosse-Knetter, *Corrections for the Hadronic Final State* (unpublished). ZEUS-98-031, internal ZEUS-note, 1998.

[64] S. Bentvelsen, J. Engelen and P. Kooijman, *Reconstruction of* (x, Q^2) *and extraction of structure functions in neutral current scattering at HERA*, *Proc. Workshop on Physics at HERA*, W. Buchmüller and G. Ingelman (eds.), Vol. 1, p. 23. Hamburg, Germany, DESY (1992).

[65] W.H. Smith et al., *The ZEUS calorimeter first level trigger.* Nucl. Inst. Meth. **A 355**, 278 (1995).

[66] T. Wolff et al., *A drift chamber track finder for the first level trigger of the H1 experiment.* Nucl. Inst. Meth. **A 323**, 537 (1992).

[67] M. Wodarczyk, *Measurement of the F_2 Structure Function of the Proton at HERA from 1996 and 1997 ZEUS Data.* Ph.D. Thesis, University of Wisconsin, 1999.

[68] R. W. Hendricks, *Space charge effects in proportional counters.* Rev. Sci. Inst. **40**, 1216 (1969).

[69] Y.-S. Tsai, *Pair production and bremsstrahlung of charged leptons.* Rev. Mod. Phys. **46**, 815 (1974);
Y.-S. Tsai, *Erratum.* Rev. Mod. Phys. **49**, 421 (1977).

[70] ZEUS Coll., J. Breitweg et al., *Measurement of $D^{*\pm}$ production and the charm contribution to F_2 in deep inelastic scattering at HERA.* Eur. Phys. J. **C 12**, 35 (2000).

[71] H1 Coll., C. Adloff et al., *Measurement of D^* meson cross-sections at HERA and determination of the gluon density in the proton using NLO QCD.* Nucl. Phys. **B 545**, 21 (1999).

[72] Particle Data Group, C. Caso et al., *Review of particle physics.* Eur. Phys. J. **C3**, 1 (1998).

[73] H. Albrecht et al., *Inclusive production of D^0, D^+ and D^{*+} (2010) mesons in B decays and nonresonant e+ e- annihilation at 10.6 GeV.* Z. Phys. **C52**, 353 (1991).

[74] Bortoletto, D. and others, *Charm production in nonresonant e+ e- annihilations at $\sqrt{s}$ = 10.55 GeV.* Phys. Rev. **D37**, 1719 (1988).

[75] L. Gladilin, *Charm hadron production fractions.* Preprint hep-ex/9912064, 1999.

[76] K. Abe et al., *Measurement of the b-quark fragmentation function in Z^0 decays.* Phys. Rev. **D65**, 092006 (2002).

Summary

The proton, one of the three cornerstones of every day matter, is built up from quarks and gluons. The innards of the proton are not static, but rather boiling with activity, changing appearance from moment to moment. This ongoing metamorphosis is described by the quantum theory of the *colour symmetry*: Quantum Chromo Dynamics or QCD. The theory of QCD describes how the picture of the proton changes when zooming in on finer details. The number of visible quarks increases when the probed distance decreases. This *evolution* of the quark structure of the proton as a function of the probed distance scale can be calculated. The way to do this is not *per se* unique, and there are actually several approaches, each of which with a different angle on how to solve this problem. The DGLAP evolution scheme is one of these approaches and to date it has proven to be the one best able to describe the deep inelastic scattering data.

QCD also gives rise to the production of heavy quarks in electron-proton interactions. These heavy quarks have a mass that exceeds that of the proton itself. Nevertheless they can be pair produced in interactions with the proton. This is a direct result of the Heisenberg Uncertainty principle, one of the founding principles of quantum mechanics, combined with the dynamics of QCD.

In the *perturbative* region, $Q^2 \gtrsim 1\,\mathrm{GeV}^2$, it is possible to use QCD to calculate the cross section of heavy quark (c,b,t) production. For the case of ep-scattering this has been done up to the next-to-leading order in the DGLAP evolution scheme. The QCD calculation gives predictions for the production of charm and anticharm quarks. But in the experimental reality, free quarks can not be seen. Rather, the quarks go through a series of interactions that involve energies $\lesssim 1\,\mathrm{GeV}^2$. These processes are usually referred to as *hadronisation*. There are currently no calculations, based on the quantum theory of chromodynamics, available for these kind of *soft* processes. To model these, one has to use QCD-inspired phenomenological models, that have been refined over many years. The results of the partonic (hard) cross section convoluted with the (soft) phenomenological description can be confronted with experimental data.

Within the realm of hadronisation, heavy quarks are in a land of their own. Due to their large mass, they are sensitive to simplifications made for the modelling of the processes that involve the light quarks (u,d,s). For the semileptonic decay of charmed mesons, this affects both the formation of the charmed mesons and the subsequent weak decay of the bound charm quark. The formation of the charmed mesons is simulated using the Peterson fragmentation model. For the modelling of the semileptonic decay there are predictions available that are the result of *exact* calculations using the quantum mechanical wavefunctions. The energy spectrum of the decay electrons that follows from these calculations is harder, *i.e.* more energetic, than that of the naive model that is used for the semileptonic decay of quarks in standard Monte Carlo hadronisation packages.

The measurement of the charm production through the detection of the semileptonic decay of charmed mesons is performed with data taken with the ZEUS experiment. The ZEUS experiment measures interactions on the HERA ring, which collides positrons on protons of 27.5 and 820 GeV, respectively. During the 1996-1997 running period, a data sample with an equivalent luminosity of 33 pb^{-1} was collected that is used in the analysis of semileptonic charm production.

The selection of events for this analysis follows the criteria for the inclusive F_2 measurement of the ZEUS collaboration, on the same data set. The electron from the semileptonic decay is then tagged by combining calorimeter and tracking information. This selects an electron enriched sample, but the larger part of this sample actually consists of hadrons (π^-, K^- and $\overline{p}$). It is possible to subtract these hadrons from the dE/dx -spectrum of this sample, using a specifically selected hadron sample. What remains is an electron sample that contains a small remnant of the $\overline{p}$-background that can easily be subtracted from the total number of electrons that is obtained. The inclusive electron signal contains, in addition to the semileptonic charm electron, also electrons from other (background) sources. The contribution of these backgrounds, from photon conversions, Dalitz decay of neutral pions and the semileptonic decay of beauty quarks, can be determined by using various techniques. Subsequently, these non-charm electrons can be removed from the electron signal, such that only the charm-decay electrons remain.

Based on this analysis the production cross section could be measured for the kinematic region $2 < Q^2 < 1000\,\text{GeV}^2$ and $0.03 < y < 0.70$. On this same domain the cross section differential in Q^2, x and W as well as P_T^{SLe} and η^{SLe} could be determined. The contribution of charmed quarks to the proton structure, $\text{F}_2^{c\overline{c}}$, could be extracted for 20 bins in the (Q^2, x)-plane, extending previous results by almost an order of magnitude. The comparison between these results and the aforementioned QCD calculations show that the standard model holds for the production of charm quark in DIS.

The agreement between the measurements on charm production and the theory prediction can be used to extract one of the fundamental parameters of the standard model from data: the mass of the charm quark. As the measurements are made in limited regions of the produced quarks phase space, there is an intrinsic dependency on the modelling of the hadronisation. To acknowledge this, the charm mass is extracted concurrently with the free parameter of the Peterson fragmentation model. The charm mass is found to be $m_c = 1.33 \pm 0.04 \pm 0.05\,\text{GeV}$ and $\epsilon_P = 0.082 \pm 0.010 \pm$

0.001. These results are competitive with other results and in fact once again show the validity of the DGLAP-QCD picture of the proton.

Samenvatting

Aan het begin van de 20$^{\mathrm{ste}}$ eeuw was men de mening toegedaan dat al het stoffelijke in deze wereld slechts was opgebouwd uit protonen, neutronen en elektronen. Deze bouwstenen die ondeelbaar of fundamenteel geacht werden, liggen aan de basis van bijvoorbeeld het Periodiek Systeem der Elementen van Mendelejev. Dit beeld bleek echter te eenvoudig en halverwege dezelfde eeuw vond men bij experimenten in de Verenigde Staten het onweerlegbare bewijs dat het proton geen *fundamenteel* deeltje is, maar een interne structuur bezit. Ook het neutron bleek minder fundamenteel dan altijd aangenomen. Beide deeltjes zijn complexe objecten met een interne structuur. Het proton en het neutron zijn niet de enige 'samengestelde' deeltjes, ook wel hadronen genoemd. Tot op heden zijn er meer dan 300 hadronen gevonden en naar het zich laat aanzien is het einde nog niet in zicht. Het proton en het neutron zijn uniek door het feit dat zij stabiel zijn[1] en daardoor de atoomkernen kunnen vormen. Rond de atoomkernen bewegen elektronen als planeten rond de zon. Gezamenlijk vormen zij de stabiele wereld om ons heen.

Met de ontdekking van de structuur in het proton verdwenen het proton en het neutron van het toneel van de fundamentele bouwstenen van de natuur, de kleinste blokjes waarmee materie in elkaar gezet kan worden. Hiervoor zijn de ongrijpbare deeltjes die men *quarks* noemt in de plaats gekomen, naast het (nog altijd) fundamentele elektron en zijn broeders het muon en het tau. Een proton en een neutron bestaan uit quarks. Er zijn tot op heden zes van deze quarks 'gezien': *up, down, strange, charm, beauty* en *top*. Dit 'zien' gebeurt niet met het blote oog, zoals men naar een schilderij van Monet zou kunnen kijken, maar door het minutieus bestuderen van complexe patronen van uitelkaar vallende deeltjes. De reden dat we op een dergelijke (indirecte) manier naar quarks moeten kijken is eenvoudigweg dat quarks niet alléén voorkomen in de natuur, maar altijd in paren van 2 of 3 (of mogelijk zelfs 5).

De eerste quarkmodellen van het proton gingen ervan uit dat er slechts drie quarks

---

[1] Het neutron *an sich* heeft een levensduur van 15 minuten, maar door samenspel met het proton is het neutron in atoomkernen stabiel.

in een proton zouden zitten. Echter, in een proton zitten niet alleen deze drie quarks maar ook *gluonen*: de 'lijm'-deeltjes die de quarks in een proton binden. In zekere zin is een proton te vergelijken met een geleipudding met sukade: de gelei houdt de sukade bij elkaar. Maar in het geval van een proton is de pudding niet statisch, zoals men mag hopen van een gewone geleipudding, maar bewegen gelei en sukade in een complexe dans, binnen de vorm van de pudding. In deze dans worden continu nieuwe quark-antiquark paren en gluonen gemaakt die kort daarop weer verdwijnen (*annihileren*)om plaats te maken voor nieuwe stellen op de dansvloer van de proton balzaal. De specifieke eigenschappen van het proton worden gegeven doordat er altijd *netto* drie quarks in het proton zitten: 2 up-quarks en 1 down-quark (voor het neutron is het 2 down-quarks en 1 up- quark).

Quantum Chromo Dynamica is de theorie die beschrijft hoe quarks en gluonen met elkaar 'communiceren'. Deze theorie vertelt ons hoe het beeld verandert als we naar kleinere afstanden binnen het proton kijken. Maar QCD is niet in staat ons te vertellen *hoe* de precieze structuur van het proton eruit ziet, alleen hoe de structuur verandert. Dit betekent dat de structuur van het proton gemeten moet worden. De metingen kunnen dan gebruikt worden om voorspellingen te doen over wat er te zien zal zijn als we nog dieper in het proton gaan kijken. Nauwkeurige metingen laten zien dat QCD inderdaad de juiste voorspellingen geeft voor de structuur dieper in het proton. Ze heeft deze proef glansrijk doorstaan.

Naast de voorspellingen voor de evolutie van de structuur van het proton geeft QCD ook voorspellingen over hoe de zware charmquarks gemaakt worden bij botsingen tussen een proton en een elektron. Het interessante aan deze charmquarks is dat ze zwaar zijn, zwaarder zelfs dan het proton. Toch kunnen in het proton paren van charm en anticharm gemaakt worden door een eigenschap van de quantummechanica gecombineerd met 's werelds beroemdste natuurkundige formule, $E = mc^2$. De (quantummechanische) onzekerheidsrelatie van Heisenberg stelt dat energie niet bepaald is op korte tijdsintervallen. Einstein legde reeds in 1905 de relatie bloot die energie gelijk stelt aan massa: $E = mc^2$. Het gevolg van deze twee relaties is dat, hoewel een charmquark zwaarder is dan een proton, het toch in een proton kan voorkomen, vermits voor zeer korte tijd en tezamen met een anticharmquark, als paar. Een elektron kan een dergelijk kort levend quark raken en uit het proton schieten, zodat het quark gedetecteerd kan worden. Wat er vervolgens overblijft van het proton valt uiteen in nieuwe hadronen.

In dit proefschrift worden de bevindingen van mijn onderzoek van de productie van het charmquark beschreven. Dit onderzoek valt in twee delen uiteen. Het eerste deel is de meting van de productie van deze charmquarks in harde botsingen tussen elektronen en protonen. Het tweede deel bevat de analyse van de resultaten van dit onderzoek, gecombineerd met eerder gepubliceerde onderzoeksresultaten over dit proces, in de context van de QCD.

De meting van charm-productie wordt gedaan door de identificatie van het elektron dat geproduceerd kan worden als het anticharmquark vervalt. De meting is uitgevoerd aan de hand van botsingen in de HERA versneller in Hamburg, Duitsland die zijn waargenomen met de ZEUS detector. De HERA versneller jaagt bundels van positronen (anti-elektronen) en protonen door ruim 6 kilometer lange buizen, 25 meter onder de grond. De deeltjes gaan met een snelheid die de lichtsnelheid benadert rond en worden op verschillende plaatsen op elkaar gericht om botsingen tussen de elektronen en protonen te veroorzaken. Op één van deze plaatsen staat de ZEUS detector. De ZEUS detector is een complex apparaat van 20×12×12 meter. Bij de besturing van deze detector is een internationale collaboratie betrokken van ongeveer 400 fysici uit 15 landen.

Uit een groot aantal in de PC opgeslagen botsingen worden diegene geselecteerd die voldoen aan de criteria voor wat we diep inelastische verstrooiingen noemen. Dit zijn het type botsingen waarbij het proton zo hard geraakt wordt, dat het uit elkaar geslagen wordt. Het elektron krijgt hierdoor ook een zwiep en belandt vervolgens in de calorimeter. Het vinden van een (hoog) energetisch elektron in de calorimeter is hèt kenmerk van deze botsingen.

Na selectie blijft een verzameling van ongeveer 2 miljoen botsingen over. Het is vervolgens zaak om in deze verzameling de elektronen uit het semileptonische verval van anticharmquarks te vinden. Hierbij wordt gebruik gemaakt van de eigenschappen van elektronen gemeten door de calorimeter. Omdat het produceren van elektronen een relatief zeldzaam verschijnsel is, vergeleken bij de productie van lichte hadronen, is er een grote achtergrond.

Uit de gemeten elektronen is nog meer informatie te halen. Door te kijken naar de afhankelijkheid van de productie van bijvoorbeeld de totale massa van de verzameling van de bij de botsing geproduceerde hadronen of de verstrooiingshoek van het semileptonische elektron wordt de dynamica van de onderliggende interactie verder blootgelegd. Dit levert extra vergelijkingsmateriaal op om de theorie mee te confronteren. Door de afhankelijkheid van de productie van de energie van het foton en de snelheid van het geraakte quark in het proton te bestuderen zijn we direct gevoelig voor de bijdrage die charmquarks leveren aan de structuur van het proton. Het blijkt dat bij voldoende hoge energie van het foton charmquarks rond 30% van de structuur van het proton voor hun rekening nemen. Dit is een aanzienlijke bijdrage, zoals duidelijk moge zijn!

De tweede analyse die gepresenteerd wordt in dit proefschrift behelst het bepalen van de massa van het charmquark gecombineerd met een verfijning van van het hadronisatiemodel. De massa van het charmquark is een van de fundamentele, *a priori* onbekende, parameters van het Standaard Model van de deeltjesfysica. Het Standaard Model is de combinatie van QCD en de electrozwakke wisselwerking, welke bijvoorbeeld voor het verval van het neutron verantwoordelijk is. Het is voor het eerst dat charm-productie data uit diep inelastische verstrooiing gebruikt worden om de charmquark massa te bepalen. Om de technieken te ontwikkelen gebruiken we de door de ZEUS en H1 collaboraties gepubliceerde data van $D^{*\pm}$ productie, een hadron met een charm quark. Om deze bepalingen te doen zijn vele honderden berekeningen met het HVQDIS-programma nodig. Elk van deze berekeningen heeft tussen de 8 en 24 uur nodig op een moderne (personal) computer. De drie datasets worden vervolgens gecombineerd om tot een eindresultaat te komen dat concurreert met de traditionele methoden om de charm massa te bepalen. Tevens stelt deze analyse vast dat er, gegeven de huidige experimentele nauwkeurigheid, geen reden is om aan te nemen dat de QCD beschrijving van zware quark productie in diep inelastische verstrooiing van positronen aan protonen onvolledig is.

Dankbetuigingen

Na bijna vijf jaar werken nadert het proefschrift met deze woorden zijn voltooiing. Tijdens deze periode hebben vele mensen op velerlei wijzen mij geholpen en gesteund. Hoewel het zeker ondoenlijk zal zijn eenieder die dit aangaat persoonlijk te danken, zou ik toch graag een poging willen wagen om de mensen die belangrijke bijdragen hebben geleverd te roemen.

Als eerste wil ik mijn copromotor en twee sequentiële promotores bedanken. Els, als directe begeleider was je het meest direct betrokken bij mijn werkzaamheden. Hierbij heb je me altijd veel vrijheid gegund en ik geloof dat dit een belangrijke bijdrage heeft gehad aan het proefschrift en in de 'verzelfstandiging' van mijn werk. Daarnaast kon ik ook altijd goed mijn 'ei' bij je kwijt, over allerlei zaken die direct of indirect met het werk te maken hadden.

Paul, jouw enthousiasme voor het oplossen van de problemen inherent aan het onderzoek is buitengewoon aanstekelijk. Meer dan eens heeft dit me de moed gegeven nogmaals de tanden te zetten in een ogenschijnlijk onoplosbaar probleem - om het dan vervolgens inderdaad op te lossen.

Jos, ondanks dat je naam niet vermeld wordt als promotor heb je toch een niet te verwaarlozen bijdrage aan dit proefschrift geleverd. In de eerste plaats door mij aan te nemen als een van je promovendi, maar ook door altijd je interesse te tonen in de voortgang van het onderzoek.

De overige staf van de ZEUS groep, Henk, Leo en Els, kan én wil ik zeker niet overslaan. Zij hebben altijd met raad en daad bijgedragen aan dit werk en ook hen wil ik daarvoor hartelijk danken.

De voorgangers mag ik uiteraard ook niet vergeten: Wouter, Joost, Aart, Niels en Jaap. Hun bijdrage was (met name) het opzetten van de analyse software, koffieleuten en bij gezellige bier drinken in kroegen over de hele wereld.

Niet alleen zij, maar ook Sjors heeft op deze twee gebieden een belangrijke bijdrage gegeven. Niet alleen zaten we gelijktijdig in Hamburg, ook hebben we samen een nieuwe toepassing voor tandenborstels[1] gevonden en de stranden van Brazilië bezocht. Verder wil ik graag Gabriel en Avraam en in het bijzonder Erik succes wensen bij het werk aan de voltooiing van hun proefschriften.

Buiten de collega's uit de ZEUS groep wil ik ook graag Eric Laenen bedanken. Hij spoorde mij aan om HVQDIS te gebruiken om de charm fragmentatie en massa te bestuderen. Dit werk was zeer interessant en heeft mij veel geleerd over de onderliggende theorie van de metingen.

Ook een speciaal woord van dank voor Kees Huyser, die heeft geholpen mijn ontwerp voor een kaft te vormen tot iets dat daadwerkelijk gedrukt kan worden.

Buiten het instituut zijn er uiteraard mensen geweest die er altijd voor gezorgd hebben dat er een zekere 'balans' was in mijn hoofd. Eén zo een belangrijke sanity-factor is altijd de Madend-gang geweest - Chris, Martijn, Rogier - wekelijks bier, schaken en de mogelijkheid om naar hartelust over de duvel, z'n ouwe moer en de wereld in het algemeen te kunnen klagen. De wekelijkse traditie moeten we in stand houden tot we allemaal 'grumpy old men' zijn - vooropgesteld dat we project-H overleven na onze pensioeneringen ... of toch maar ietsjes eerder uitvoeren ? Verder (uiteraard!) Pieter, voor de bijna dagelijkse dosis film/game kritieken en veel te infrequente 'get-togethers'.

Tenslotte, lest-best, ben ik aanbeland bij de 'inner-circle' van mijn familie. Mijn ouders, broer en grootouders. Hoewel mijn werk voor jullie vaak meer leek op abracadabra dan op wetenschap, hebben jullie mij altijd gesteund en gestimuleerd mijn droom na te jagen - voor jullie ligt het resultaat.

De laatste woorden in dit proefschrift zijn, net als de eerste, voor mijn vrouw (in spé) Claudia: zonder de thuishaven van rust en kalmte die je voor me gecreëerd hebt, zou het onmogelijk zijn geweest dit te bereiken. Hopelijk kan ik deze gunst terug geven als jij aan jouw promotie-onderzoek begint.

---

[1] Voor de duidelijkheid: het schoonmaken van detector onderdelen.

The production of heavy quarks in deep inelastic scattering of electrons and protons is assumed to be a pure Quantum Chromo Dynamical (QCD) process. Exclusive measurement of heavy meson production has been the paramount method to obtain experimental data. In this thesis an alternative method is used. Open charm production is measured through the semileptonic decay of the charm quarks, using the 1996-1997 data of the ZEUS experiment. The electrons are identified in the hadron dominated final state by combining calorimeter and tracking information. The measurements can be compared with the next-to-leading order calculation of the QCD process. When the semileptonic and D* measurements are combined, the comparison with theory allows the determination of the mass of the charm quark, dual with the optimisation of the Peterson fragmentation model.